Institut für Geowissenschaften, Universität Potsdam

GEOLOGY OF ULTRA-HIGH-PRESSURE ROCKS

FROM THE DABIE SHAN, EASTERN CHINA

Dissertation

zur Erlangung des akademischen Grades
Doktor der Naturwissenschaften
(Dr. rer. nat.)
in der Wissenschaftsdisziplin Geowissenschaften

eingereicht an der
Mathematisch-Naturwissenschaftlichen Fakultät
der Universität Potsdam

von

Robert Schmid
geboren am 05.02. 1970 in Mühlheim am Main

Potsdam, im Dezember 2000

Für meinen Vater,

der nicht die Chance hatte, das Entstehen dieser Arbeit zu begleiten.

TABLE OF CONTENTS

ABSTRACT

A multidisciplinary study has been carried out to contribute to the understanding of the geologic evolution of the largest known occurrence of ultra-high-pressure (UHP) rocks on Earth, the Dabie Shan of eastern China.

Geophysical data, collected along a ca. 20 km E-W trending seismic line in the eastern Dabie Shan, indicate that the crust comprises three layers. The upper crust has a homogeneously low reflectivity and exhibits roughly subhorizontal reflectors down to ca. 15 km. It is therefore interpreted to portray a crustal UHP slab thrust over non-UHP crust. An abrubt change in intensity and geometry of observed reflectors marks the boundary of a mid- to lower crustal zone which is present down to ca. 33 km. This crustal zone likely represents cratonal Yangtze crust that was unaffected by the Triassic UHP event and which has acted as the footwall during exhumation of the crustal wedge. Strong and continuous reflectors occurring at ca. 33-40 km depth most likely trace the Moho at the base of the crust. Any trace of a crustal root, that may have formed in response to collision tectonics, is therefore not preserved. A shallow tomographic velocity model based on inversion of the first arrivals is constructed additionally. This model clearly images the distinct lithologies on both sides of the Tan Lu fault. Sediments to the east exhibit velocities of about $3.4 - 5.0$ km* s^{-1}, whereas the gneisses have $5.2 - 6.0$ km* s^{-1}. Geometry of velocity isolines may trace the structures present in the rocks. Thus, the sediments dip shallowly towards the fault, whereas isoclinal folds are imaged to occur in the gneisses.

Field data from the UHP unit of the Dabie Shan enables definition of basement-cover sequences that represent sections of the former passive margin of the Yangtze craton. One of the cover sequences, the Changpu unit, still displays a stratigraphic contact with basement gneisses, while the other, the Ganghe unit, includes no relative basement exposure. The latter unit is in tectonic contact with the basement of the former unit via a greenschist-facies blastomylonite. The Changpu unit is chiefly constituted by calc-arenitic metasediments intercalated with meta-basalts, whereas the Ganghe unit contains arenitic-volcanoclastic metasediments that are likewise associated with meta-basalts. The basement comprises a variety of felsic gneisses, ranging from preserved eclogitic- to greenschist-facies parageneses, and locally contains mafic-ultramafic meta-plutons in addition to minor metabasaltic rocks. Metasites of all lithologies are eclogite-facies or are retrogressed equivalents, which, with the exception of those from the Ganghe unit, bear coesite and thus testify to an UHP metamorphic overprint. Mineral chemistry of the analysed samples reveal large compositional

variations among the main minerals, i.e. garnet and omphacite, indicating either distinct protoliths or different degrees of interaction with their host-rocks. Contents of ferric iron in low Fe_{tot} omphacites are determined by wet chemical titration and found to be rather high, i.e. 30-40 %. However, an even more conservative estimate of 50% is applied in the corresponding calculations, in order to be comparable with previous studies. Textural constraints and compositional zonation patterns are compatible with equilibrium conditions during peak metamorphism followed by a retrogressive overprint. P-T data are calculated with special focus on the application of the garnet-omphacite-phengite barometer, combined with Fe-Mg exchange thermometers. Maximum pressures range from 42-48 kbar (for the Changpu unit) to ~37 kbar (for the Ganghe unit and basement rocks). Temperatures during the eclogite facies metamorphism reached ca. 750 °C. Although the sample suite reveals variable peak-pressures, temperatures are in reasonable agreement. Pressure differences are interpreted to be due to strongly Ca-dominated garnet (up to 50 mole % grossular in the Changpu unit) and modification of peak-compositions during retrogressive metamorphism.

The integrated geological data presented in this thesis allow it to be concluded that,

i) basement and cover rocks are present in the Dabie Shan and both experienced UHP conditions

ii) the Dabie Shan is the metamorphic equivalent of the former passive margin of the Yangtze craton

iii) felsic gneisses undergoing UHP metamorphism are affected by volume changes due to phase transitions (qtz ⇔ coe), which directly influence the tectono-metamorphic processes

iv) initial differences in temperature may account for the general lack of lower crustal rocks in UHP-facies

KURZFASSUNG

Um das Verständnis der geologischen Entwicklung des größten bekannten Vorkommens von ultra-hochdruck (UHP) Gesteinen auf der Erde, des Dabie Shan im östlichen China, zu erhöhen, wurde eine multidisziplinäre Studie durchgeführt.

Geophysikalische Daten wurden entlang einer ca. 20 km langen seismischen Linie im östlichen Dabie Shan gesammelt. Diese reflektionsseismischen Daten zeigen, dass die Kruste aus drei Lagen besteht. Die Oberkruste besitzt eine durchgehend niedrige Reflektivität und meist subhorizontale Reflektoren bis in eine Tiefe von ca. 15 km. Aufgrund dieser Charakteristika wird diese Zone als UHP-bezogener krustaler Keil interpretiert, der auf nicht UHP Kruste überschoben wurde. Ein abrupter Wechsel in der Geometrie aber auch Intensität der Reflektoren markiert die Grenze zu einer mittel- bis unterkrustalen Zone, die sich bis ca. 33 km Tiefe erstreckt. Diese Zone repräsentiert wahrscheinlich kratonale Yangtze Kruste, die von der triassischen UHP-Orogenese nicht erfasst wurde, aber während der Exhumierung das Liegende relativ zum UHP Keil war. Starke und kontinuierliche Reflektoren im Tiefenintervall von 33-40 km bilden höchstwahrscheinlich die Moho an der Basis der Kruste ab. Relikte einer Krustenwurzel, die sich wahrscheinlich während der Kollisionstektonik gebildet hatte, sind nicht sichtbar. Ein flaches tomographisches Geschwindigkeitsmodell, das auf der Inversion der Ersteinsätze gründet, konnte zusätzlich erstellt werden. Dieses Modell bildet deutlich die unterschiedlichen Lithologien auf beiden Seiten der Tan Lu Störung ab. Sedimente östlich der Störung zeigen Geschwindigkeiten von $3.4 - 5.0$ km* s^{-1}, wohingegen die Gneise im Westen $5.2 - 6.0$ km*s^{-1} aufweisen. Die Geometrie der Geschwindigkeits-Isolinien kann als Ausdruck der Strukturen der Gesteine angenommen werden. Somit zeigen die Sedimente ein nordwestliches Einfallen zur Störung hin, wohingegen isoklinale Falten in den Gneisen abgebildet werden.

Geländedaten aus der UHP Einheit des Dabie Shan ermöglichen die Definition von Grundgebirgs- und Deckeinheiten, die Teile des ehemaligen passiven Kontinentalrandes des Yangtze Kratons repräsentieren. Eine der Deckeinheiten, die Changpu Einheit, besitzt nach wie vor einen stratigraphischen Kontakt zu den Grundgebirgs-Gneisen. Der anderen Einheit hingegen, der Ganghe Einheit, fehlt ein entsprechendes Grundgebirge. Diese Einheit steht vielmehr über einen Blasto-Mylonit in tektonischem Kontakt zum Grundgebirge der vorherigen. Die Changpu Einheit baut sich aus kalk-arenitischen Metasedimenten auf, die mit Metabasalten assoziiert sind. Die Ganghe Einheit wird von arenitisch-vulkanoklastischen Metasedimenten, die ebenfalls mit metabasaltischen Gesteinen vergesellschaftet sind,

dominiert. Das Grundgebirge baut sich aus diversen felsischen Gneisen auf, die von reliktisch eklogitfaziell bis grünschieferfaziell ausgeprägt sind, und in denen, zusätzlich zu Metabasalten, sporadisch mafisch-ultramafische Meta-Plutone auftreten. Mit Ausnahme der Ganghe Einheit, führen die Metabasite Coesit und belegen somit das UHP Ereignis. Die Mineralchemie der analysierten Proben dokumentiert deutliche Variationen in der Zusammensetzung der Hauptminerale, Granat und Omphazit, was entweder unterschiedliche Protolithe oder unterschiedliche Grade von Stoffaustausch mit den Wirtsgesteinen reflektiert. Gehalte von dreiwertigem Eisen in Omphaziten mit geringen Gesamteisengehalten, wurden mittels Titration bestimmt, wobei sich Werte von 30-40 % ergaben. Dennoch wurde ein noch konservativerer Wert von 50% dreiwertigem Eisen in den entsprechenden Berechnungen angenommen, hauptsächlich, um mit anderen Arbeiten vergleichbar zu sein. Texturen und chemische Zonierungen in den Mineralen sind kompatibel mit Gleichgewichtsbedingungen während dem Höhepunkt der Metamorphose, der retrograd überprägt wird. P-T Daten wurden mit deutlicher Betonung auf das Granat-Omphazit-Phengit Barometer, das mit Fe-Mg Austausch-Thermometern kombiniert wurde, berechnet. Höchstdrucke reichen von 42-48 kbar (für die Changpu Einheit) bis ca. 37 kbar (für das Grundgebirge und die Ganghe Einheit). Während der eklogitfaziellen Metamorphose wurden Temperaturen von ca. 750 °C erreicht. Obwohl die maximalen Drucke deutlich schwanken, sind die Temperaturbestimmungen in guter Übereinstimmung. Die Druckschwankungen können zum einen durch deutlich Ca-dominierte Granate (bis zu 50 mol% Grossular in der Changpu Einheit) und/oder zum anderen durch Modifikationen der Mineralzusammensetzungen während der retrograden Metamorphose erklärt werden.

Die präsentierten integrativen geologischen Daten ermöglichen die folgenden Schlussfolgerungen

i) Grundgebirgs- und Deckeinheiten treten im Dabie Shan auf und wurden beide UHP metamorph überprägt

ii) Der Dabie Shan ist das metamorphe Äquivalent des früheren passiven Kontinentalrandes des Yangtze Kratons

iii) felsische Gneise, die eine UHP Metamorphose durchlaufen, sind von Volumenveränderungen betroffen, die durch großräumige Phasenumwandlungen (Quarz ⇔ Coesit) hervorgerufen werden, was direkt die tektono-metamorphen Prozesse beeinflusst

iv) Initiale Unterschiede in der Temperatur sind möglicherweise dafür verantwortlich, dass generell Unterkrustengesteine in UHP Fazies fehlen

I. ACKNOWLEDGEMENTS

Furthermore, I benefited from multi-lateral co-operation with many scientists and colleagues, especially Trond Ryberg and Ali Schulze provided fruitful discussions during preparation of a joint manuscript.

Dieter Rhede, Ooana Appelt and Helga Kemnitz (at GFZ Potsdam), Roald Tagle and Philippe Claeys (Humboldt University Berlin) and Eric Reuser (ETH Zürich) kindly advised, supported and helped me during analytical procedures.

II. Preface, Introduction and Objectives

The discovery of coesite as inclusions within metamorphic minerals (garnet and omphacite) of crustal rocks (Chopin 1984; Smith 1984) opened a new chapter in the global research of metamorphic petrology (Fig.1). Because coesite is stable at pressure-temperature (P-T) conditions exceeding ~28 kbar at ~700°C (Mirwald and Massonne 1980; Bohlen and Boettcher 1982), its occurrence is equivalent to formation at depths of ≥ ~90 km (Fig. 2). Previously, such physical conditions during the peak metamorphism of crustal rocks were considered unreasonable or were not considered at all (cf. Schreyer 1995; Harley and Carswell 1995). Furthermore, coesite and especially diamond were thought to form only during shock-events (e.g. extraterrestrial impacts) or within the earth's mantle whereas crustal metamorphism was "classically" restricted to pressures of about 10 kbar (e.g. Ernst 1973, 1976). Thus, Chopin (1984) and Smith (1984) documented the first positive confirmation that crustal rocks may undergo metamorphism at mantle depths and return to the surface without penetrative re-equilibration. Consequently, geodynamic models had/have to be re-evaluated and/or extended in order to incorporate such processes. However, pseudomorphs allegedly after coesite from eclogites of the Münchberg Massif were reported earlier by Chesnokov and Popov (cf. Schreyer 1985). Some years later Sobolev and Shatsky (1990) documented microdiamonds as inclusions in garnet and zircon from gneisses of the Kokchetav Massif (Kazakhstan), thus these rocks must have experienced pressures of ≥ ~40 kbar (≥ ~120 km depth, Berman 1979, Chatterjee 1991).

During the last 15 years the number of localities with crustal rocks containing coesite, diamond or other mineral-assemblages diagnostic for ultrahigh pressure (UHP) metamorphism has steadily increased (cf. Fig. 1). Thus intense research was/is being launched in order to evaluate the geodynamic significance of such rocks. These investigations help to decipher the processes acting in former, present and future deep-seated orogenic roots like the Alps or the Himalaya and enables understanding of subduction and exhumation processes of lithospheric fragments.

The world`s largest exposure of UHP rocks is the Hong`an-Dabie-Su Lu area in central-east China (Fig. 3). Coesite was first documented by Okay et al. (1989) and Wang et al. (1989), whereas Xu et al. (1992) reported micro-diamond from eclogite, requiring formation at even higher pressures (cf. Fig. 2). A wealth of publications has already addressed the tectonics and petrology of the UHP-facies rocks from Dabie Shan (e.g. Okay 1993;
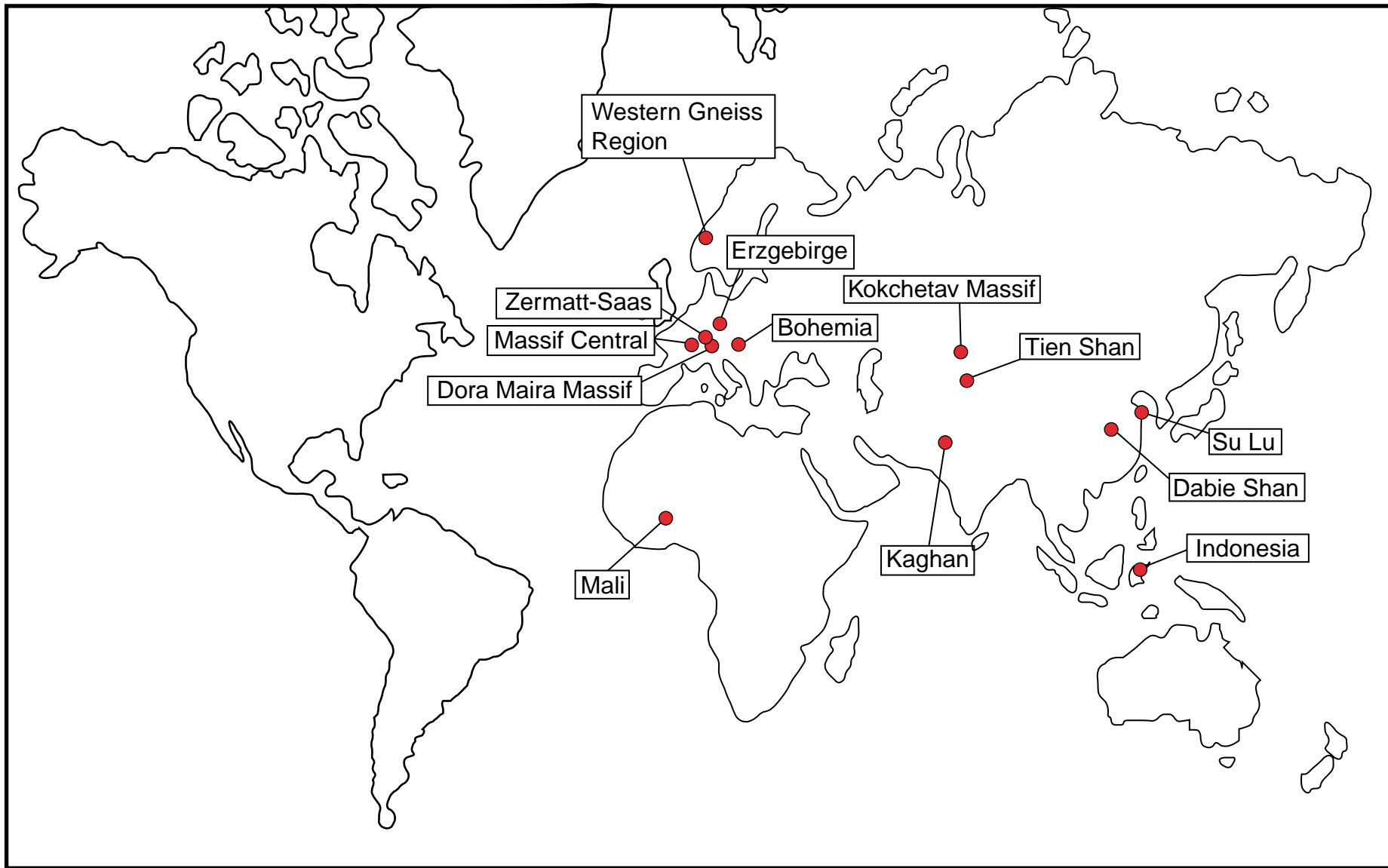
Figure 1: Global map showing the localities of confirmed occurrences of coesite and/or diamond in crustal rocks. Modified after Carswell (2000), Kaghan locality in Pakistan is after O`Brien et al. (in press) and Massif Central after Lardeaux (1998) and Lardaux et al. (1999).
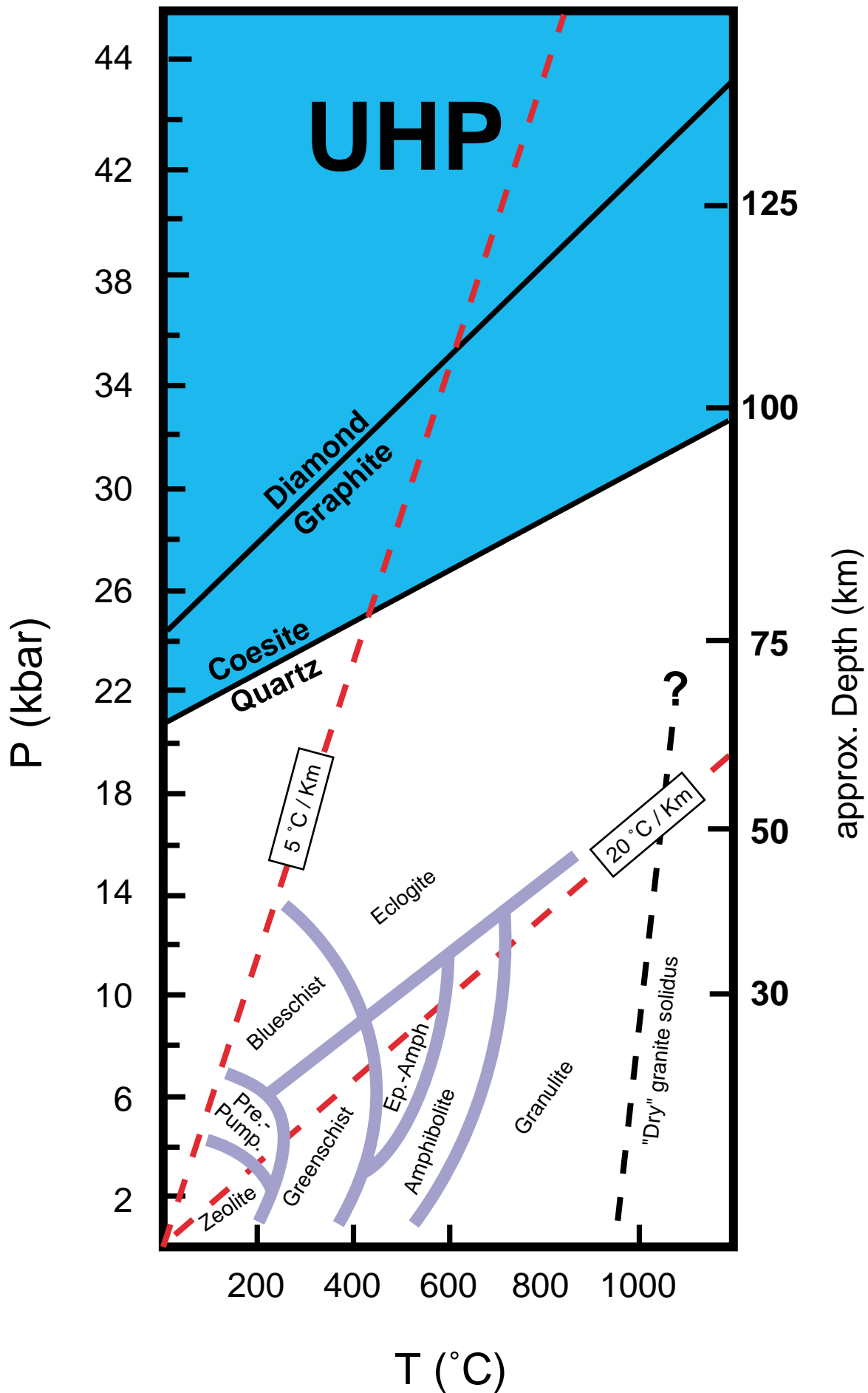
Figure 2: P-T grid showing the fields of the common metamorphic facies and the field of ultra-high-pressure metamorphism as defined by the quartz-coesite transition (cf. Schreyer 1995; Carswell and Zhang 1999). Also shown are two geothermal gradients and the "dry" Granite solidus for comparison.

Hacker et al. 1996; 1998; 2000; Kern et al. 1998; Liou et al. 1996; Rowley et al. 1997; Schmid et al. 1999; Ratschbacher et al. 2000), establishing the principal metamorphic paths of the rocks, the age of their metamorphism and proposing models for the lithospheric collision and exhumation. However, at least an equal wealth of information in the UHP rocks from eastern China remain to be deciphered.

The present work is a synthesis of field observations, geophysical data, petrography, mineral chemistry and thermobarometry contributing to the understanding of the geology of the Dabie Shan. Therefore it is at least fair to mention that some, but not all, of the data, subsequent interpretations and conclusions presented here were already published in abstracts and/or articles (e.g. Oberhänsli et al. 1998; Franz et al. in press; Schmid R. et al. 1999; 2000a; 2000b, in press) and are the results of multi-lateral co-operative work and mental exchange with many people.

The single chapters of this thesis concern different problems encountered in the Dabie Shan. Most emphasis is put on the mineral chemistry and calculation of peak P-T conditions of eclogite-facies rocks. Although some aspects are only briefly touched upon or even less elegantly, imported from the literature, a discussion summarises all results and puts them together to elucidate the geologic history of the Dabie Shan by drafting a petro-tectonic scenario. Employment and interpretation of geophysical data (Chapter 2) became possible through fruitful co-operation with the GeoForschungsZentrum Potsdam (cf. Schulze et al. 1998; Schmid et al. in press). New insights into the field-relationships in the UHP unit (Chapter 3) are founded on Chinese mapping work (Tang et al. unpubl.), which were extremely useful in combination with the observations of all project members. Mineral chemistry and thermobarometry (Chapter 4) is performed with special focus on the application of the garnet-clinopyroxene-phengite barometer in order to detect and document differences in the peak-conditions of different rock-sequences and -types. In this connection it is worth mentioning that impure marbles (calc-silicates) hosting metabasites were the central emphasis and that thermobarometers, originally designed for mafic rocks, are successfully applied to carbonatic and more felsic rocks.

The sample suite was collected by various members of the project group during several field-trips to the Dabie area in the years 1997-1999. Analytical data for these samples were obtained in the petrographic and geochemical laboratories at the Institut für Geowissenschaften Universität Potsdam, the electron microprobe, XFA and SEM laboratories at the GeoForschungsZentrum Potsdam and the electron microprobe facility at the Humboldt Universität Berlin as well as from the Raman probe at the ETH Zürich.

1. REGIONAL GEOLOGY OF THE DABIE SHAN

The Dabie Shan is part of the Qinling-Dabie-SuLu metamorphic belt in east-central China (Fig. 3, inset). Its formation resulted from the collision of the Sino-Korean (North China Block, NCB) with the Yangtze (South China Block, SCB) craton (Mattauer et al. 1985). The more than 2000 km, WNW-ESE stretching orogen is segmented by several, in part active, faults related to the India-Asia collision (Peltzer et al. 1985); most prominent is the dextral-transtensive Tan Lu fault, forming the eastern boundary of the Dabie and the western boundary of the Su Lu, respectively. This major fault is often interpreted to have a sinistral offset of more than 500 km (cf. Fig. 3; e.g. Okay et al. 1993; Yin and Nie 1993). However, no evidence exists for a pre-Cretaceous Tan Lu fault activity (cf. Schmid et al. 1999; Ratschbacher et al. 2000 for discussion).

According to paleomagnetic data, the NCB and SCB were separated during the Paleozoic by an ocean, which was several thousand kilometres wide, and approached each other in the late Paleozoic (Gilder and Courtillot 1997). The present suture-geometry is controlled by the `scissor-like´ terminal collision and by the former shape of the two cratons. Recent structural and chronological studies (Hacker et al. 2000; Ratschbacher et al. 2000) propose that the Yangtze craton indented the Sino-Korean craton and paleomagnetic data show that this progressed from E to W. Initial collision was closely followed by Triassic-Jurassic clockwise rotation of the SCB relative to the NCB, and the subsequent closure of the remaining ocean in the W (Zhao and Coe 1987; Enkin et al. 1992). However, late Paleozoic ages of metamorphic rocks in the eastern Qinling-Tongbai segments may indicate the collision of microcontinents with the NCB (cf. Kröner et al. 1993). A magmatic arc related to the subduction of large amounts of oceanic crust beneath the NCB is still missing in the Hong`an-Dabie-Su Lu area. On the other hand such relics from the western sections in the Qinling-Tongbai area have been described (Kröner et al. 1993).

The late Paleozoic convergence involved attempted northward subduction of the thinned passive margin or a promontory of the SCB beneath the NCB. P-T conditions of the accompanying metamorphism reached the stability fields of coesite and diamond (e.g. Okay 1989; Wang et al. 1989; Xu et al. 1992), thus corresponding to subduction of continental crust to depths of 120-150 km (cf. Fig. 2). The age of this ultrahigh-pressure (UHP) metamorphic event is estimated to be c. 240 Ma based on SHRIMP U/Pb zircon and Sm/Nd mineral ages (e.g. Hacker et al. 1998). The protoliths of the UHP rocks are reported to be much older, i.e.
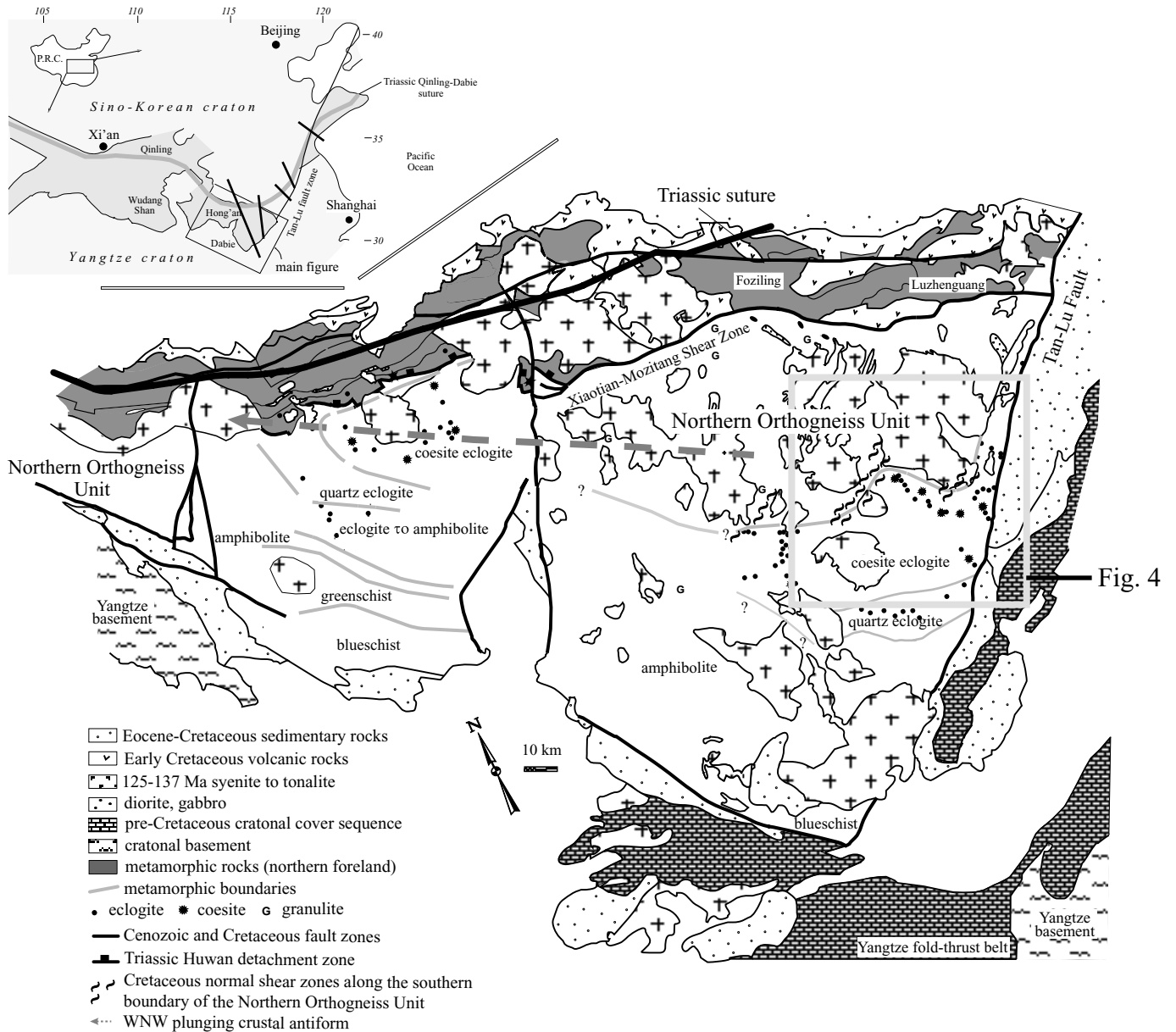
Fig. 3: Dabie and Hong'an Mountains at the eastern end of the Qinling-Dabie orogenic belt.
Locations of major faults and units are discussed in the text. Inset shows the Triassic collisional orogen
in central China and approximate locations of various refraction profiles (solid black lines) as discussed in
the text. Modified from Ratschbacher et al. (2000) and Gao et al. (1998).

Precambrian (> 700-800 Ma; e.g. Rowley et al. 1997; Maruyama et al. 1998; Romer unpubl.), thus any record of the Lower and Middle Paleozoic is still missing in this region.

Exhumation of the subducted crustal slab from upper mantle depths might have been triggered as buoyancy contrast (felsic crust vs. mantle) became dominant versus subduction forces ("slab-pull" and "continental drift-push"). According to analogue models this may take place if erosion accompanies an ongoing compressive regime (Chemenda et al. 1995, 2000). Such an exhumation model further predicts cooling of the exhuming rocks (e.g. Ernst and Peacock 1996). Development of a normal-sense shear zone on top and a thrust-fault zone at its footwall lets a coherent slab rise to crustal levels along the former subduction channel. During exhumation the rocks underwent, in part hydrous, retrogression and were deformed and folded penetratively (e.g. Hacker et al. 1998; 2000; Webb et al. 1999; Schmid et al. 1999). The exhumation through the middle and upper crust took place during the Cretaceous and the Cenozoic in response to far field collisions and Pacific subduction in the east. The major unroofing was accomplished by oblique detachment faulting and associated magmatism along the Xiaotian-Mozitang shear zone (Ratschbacher et al. 2000; Fig. 3).

The Hong´an and Dabie Shan are the largest area of UHP rocks on earth forming a WNW-plunging crustal antiform. The key to this structure was found in the Hong´an, where the NW-dipping limb is preserved. Along the S to SW-dipping limb several tectono-metamorphic units with decreasing grade normal to the fold-axes are exposed (cf. Hacker et al. 2000; Fig. 3).

The tectono-stratigraphy of the Dabie Shan is built up from south to north by the Yangtze foreland fold-thrust belt, the blueschist-facies Susong-complex, the HP- and UHP-eclogite bearing gneiss units, the Northern Orthogneiss unit (NOU), and various medium- to low grade units along the northern margin of Dabie (Fig. 3). Voluminous Cretaceous magmatism, overprinting the northern oroclinal limb in the Dabie, is concentrated in the NOU, but occurred throughout the orogen and its foreland (e.g. Okay 1993; Liou et al. 1996; Jahn et al. 1999). Recently, however eclogites were reported from the NOU, but their age(s) and formation conditions and thus significance for the Triassic UHP metamorphism are not constrained in detail (cf. Tsai and Liou 2000). The margins of the orogen are covered by Cretaceous to Cenozoic volcanic and sedimentary rocks.

The UHP unit of Dabie is composed of quartzo-feldspathic (ortho-) gneisses and metasediments such as garnet-mica-schists, marbles or quartzites (e.g. Liou et al. 1996). All lithologies are cross-cut and/or interlayered with metabasites occurring as layers or lenses, indicating that they have magmatic precursors. Due to this characteristic rock association the

orogen is in general interpreted to comprise a former section of Yangtze basement plus cover rocks, which likely originated within a Precambrian rift-setting (Reischmann et al. 1990; Ames et al. 1993; Rowley et al. 1997; and below). The volumetrically minor metabasites provide evidence for the UHP event (e.g. Wang and Liou 1991; Okay 1993; Carswell et al. 1997). The gneisses themselves, although hosting eclogitic UHP mafic/ultramafic rocks, are commonly reported to mainly show amphibolite- to greenschist-facies assemblages (e.g. Liou et al. 1996) However, recent reports of coesite in the gneisses (Tabata et al. 1998), petrologic constraints compatible with UHP conditions (Carswell et al. 2000; and below) as well as field relations in the UHP unit (below) clearly provide evidence for regional UHP conditions within a coherent crustal segment.

2. THE INTERIOR OF THE EASTERN DABIE SHAN – INTERPRETATION OF DEEP REFLECTION AND SHALLOW TOMOGRAPHIC DATA

Due to the orogen-wide occurrence of UHP rocks (cf. Fig. 3) the Dabie-Su Lu area is a recent target for a deep drillhole within the framework of the International Continental Drilling Program (ICDP). Hence, an initial feasibility test and forerunner project to a large-scale seismic study was carried out by a joint Chinese-German group within the eastern Dabie Shan. The near vertical explosion seismic data were collected within a standard common depth point (CDP) geometry (cf. Schulze et al. 1998). Here, the results and interpretations of deep reflection seismic data and a shallow 2D tomographic velocity model along a 20 km E-W traverse are reported (for details of the data processing the reader is referred to Schmid et al. in press).

A number of questions related to the genesis of UHP rocks can be addressed only by seismic experiments through the observation of deep and shallow structures. Those questions include: (i) What are the seismic reflection patterns of UHP crust and which implications for the present architecture of the Dabie Shan can be obtained? (ii) How heterogeneous is UHP crust? Are there distinct lithological slivers and what is their apparent thickness? (iii) What underlies the UHP rocks? (iv) Can the understanding of the 3D structural geometries of UHP rocks be enhanced by shallow 2D tomographic velocity models?

Previous seismic investigations of the Dabie Shan established the principal crustal velocity distribution by employing first-order refraction seismology with low spatial resolution. These seismic profiles were interpreted to show a four-layer crust below the Dabie region with velocity values of 6.14, 6.40, 6.63 and 6.95 km*s^{-1} for the upper, middle, upper-lower and lowermost crust, respectively (Dong et al. 1997; Yang and Chen 1998; Wang et al. 2000). Other seismic studies, published in Chinese, are summarised in Gao et al. (1998; cf. Inset of Fig. 3). Kern et al. (1998a, b) investigated the petrophysical properties of various rocks from Dabie and correlated them with the observed velocity data. They concluded that the crust is dominantly felsic and that eclogite is a minor constituent even in the deeper crust and a delamination model for the lowermost crust was suggested.
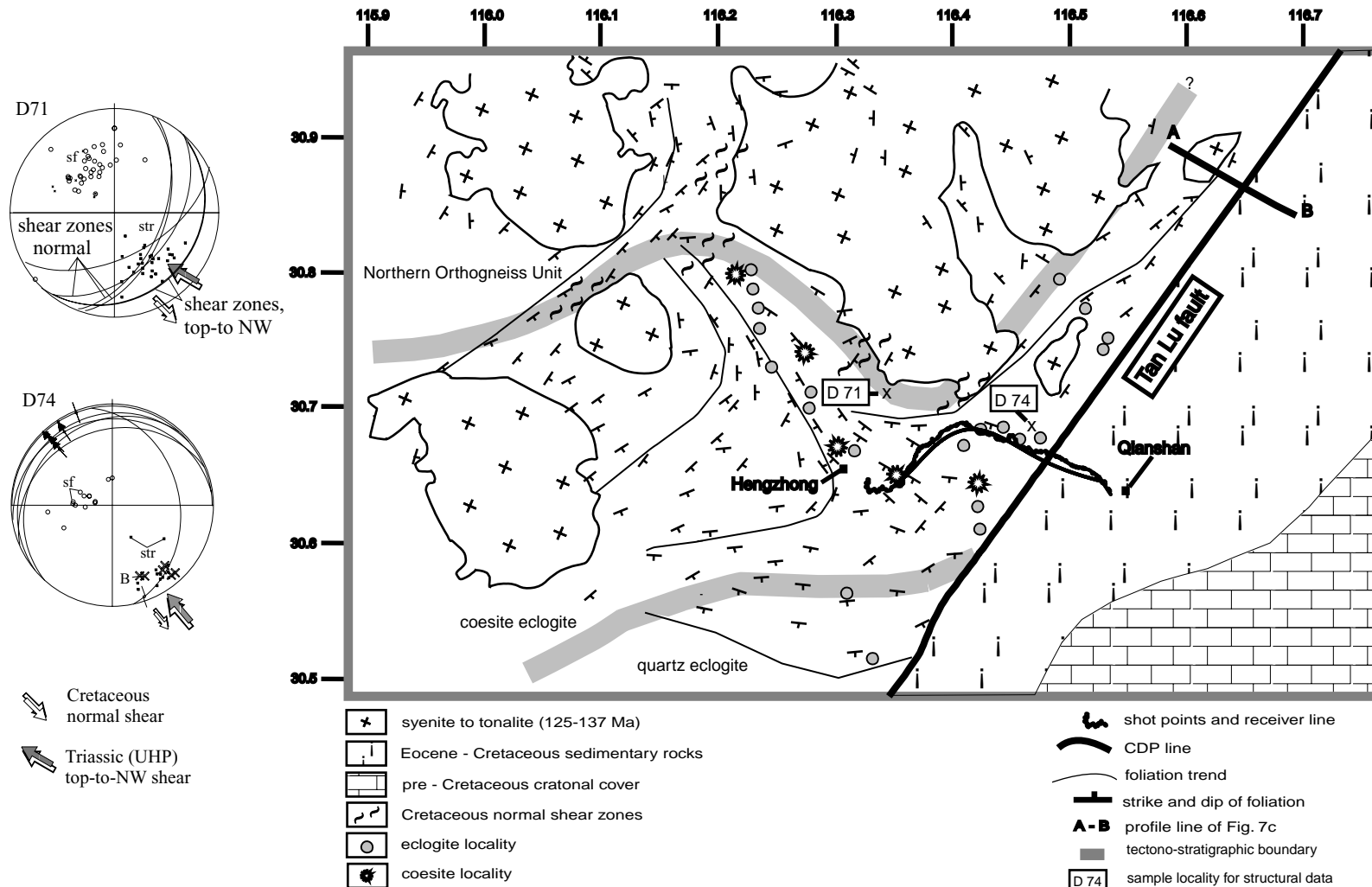
Figure 4: Map showing the geological setting of the eastern Dabie Shan and the location of the CDP line (modified from Ratschbacher et al. 2000 and Schmid et al. in press). Insets left show stereograms with structural data from stations within the UHP unit and close to a Cretaceous granitoid. Triassic top-to-NW flow, related to exhumation of the UHP rocks is overprinted by late Cretaceous, top-to-SE, normal shear. B, fold axes; sf, foliation, str, stretching (flow) lineation (modified from Hacker et al. 2000).

2.1 LOCAL GEOLOGY AND DATA ACQUISITION

The area of seismic investigation is divided by the Tan Lu fault (Fig. 4). West of the fault the seismic line runs through UHP gneisses, but comes close to a Cretaceous granite. All fabrics in the UHP gneisses show a SE-dip in the eastern part of the line, whereas they have a more southerly dip towards the west (Fig. 4). This variable dip results from doming by Cretaceous intrusions. Several local faults, oriented subparallel to the Tan Lu, truncate this unit (e.g. Zhang et al. 1995). Unmetamorphosed sedimentary rocks of Cretaceous to Eocene age crop out east of the Tan Lu and dip shallowly (~15°) towards the fault; however, most of the area is covered by Quaternary alluvium. These Cretaceous-Cenozoic rocks constitute the cover of the Yangtze foreland fold-thrust belt east and south of Dabie.

The 20 km long profile runs from east of the village Hengzhong to the west of Qianshan; due to the pronounced topography it follows a road and is thus rather crooked (cf. Fig. 4). Three different recording systems, resulting in 300 seismic channels, were used: a 120 channel Chinese DFS V (geophone spacing 50 m), a 96 channel German telemetric SUMMIT, and 14 six-channel PDAS (the latter two with a receiver spacing of 100 m). Along the profile 115 borehole shots were fired with an average spacing of 200 m and an average charge size of 50 kg. Whereas the Chinese geophones moved to provide a conventional Common Depth Point (CDP) measurement, the German equipment was installed to compensate the forward motion of the DSF V in such a manner that the spread covered the total length of the profile all the time. The goal of this recording scheme was to derive a shallow velocity model in addition to the CDP image.

Fig. 5 shows the unmigrated, stacked section along the profile, which was migrated under the assumption of a simple crustal velocity model of $Vp = 6.5$ km*s^{-1} (cf. Fig. 6). Other reasonable velocity models were tested, straddling the previously determined velocity values of 6.2 to 6.9 km*s^{-1}(cf. Dong et al. 1996; Wang et al. 2000), but it was found that there is no large effect on the migrated section.

In addition to the CDP stacking, resolving of the uppermost crustal structure was approached by interpreting the arrival time of the primary P-waves by tomographic techniques (Fig. 7a). The resolution of the inversion varies: the lower boundary and both edges are poorly resolved, the central parts of the line were well imaged. As the shallow velocity structure is
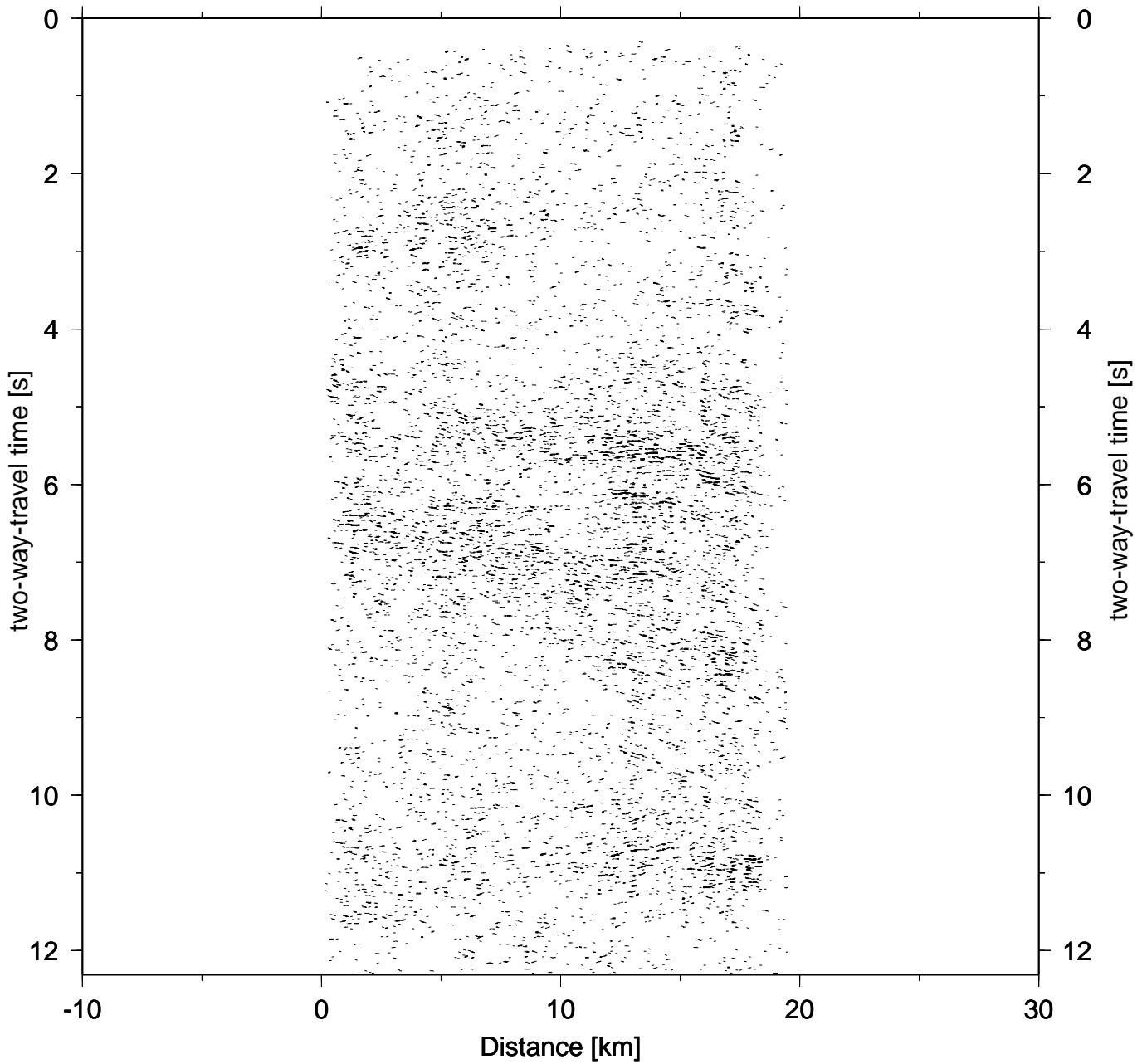
Figure 5: Image of the processed reflection data. Note that distance scale is pinned at 0 and 20 km at the south-western and eastern end of the line, repectively. a) Unmigrated line drawing of the stacked image, which has been automatically processed to obtain coherent reflective elements. Most of the reflectors are located in the middle and lower crust. The Moho is located at ca. 10-12 seconds two-way-travel (TWT) time.

characterised by a high surface velocity in combination with a very small average velocity gradient the tomographic model extends only to < 700 m depth (Fig. 7a).

2.2 REFLECTION SEISMICS AND TOMOGRAPHY INVERSION OBSERVATIONS

The crust beneath the line is characterised by strong reflections down to ca. 12 s two-way travel time (TWT) (~ 40 km; cf. Fig. 5), with a downward increasing reflectivity. The crustal reflectivity can be subdivided into three zones (cf. Fig. 6): (i) a very weakly reflective upper crust down to c. 5 s (~ 0-15 km); (ii) a diffuse but strongly reflective mid to lower crust at 5-10 s (~ 15-33 km), and (iii) a prominent reflective lowermost crust at 10-12 s TWT (~ 33-40 km).

The applied migration techniques and the velocity-model of 6.5 km*s^{-1} for the crust result in an uncertainty of reflector dips in the order of 10-15°. In this respect, the upper crustal reflectors (zone (i)) appear broadly subhorizontal, but tend to have an apparent easterly dip; reflectors occur mainly in the western part of the line. In zone (ii) reflections concentrate within the upper eastern and middle parts. Reflectors are subhorizontal in the upper part and more consistent easterly dipping in the middle western part. The lowermost zone (iii) exhibits more or less continuous reflections throughout the section with a subhorizontal appearance.

Tomographic inversion of the first arrivals revealed two zones with contrasting velocity structure that coincide with the regions east and west of the Tan Lu fault zone (Figs. 3, 4). Due to inversion techniques the tomographic profile has been inflected directly along the line, resulting in a crooked image (Fig. 7a). The eastern zone is characterised by an increase in velocity from 3.4 km*s^{-1} at the surface to 5.0 km*s^{-1} in a depth of c. 500 m. The western zone is clearly distinct in shape and values of velocity isolines. It is separated from the eastern zone by a strong and sharp increase in near-surface velocities, from < 4 km*s^{-1} to > 5.5 km*s^{-1} within < 2 km. In the western section surface velocities of 5.2 km*s^{-1} increase downward to 6.0 km*s^{-1} at 700 m. In the upper part two subhorizontal layers, more prominent in the W, are observed. They are underlain by several variably shaped zones, which differ in velocity by 0.1-0.2 km*s^{-1}.
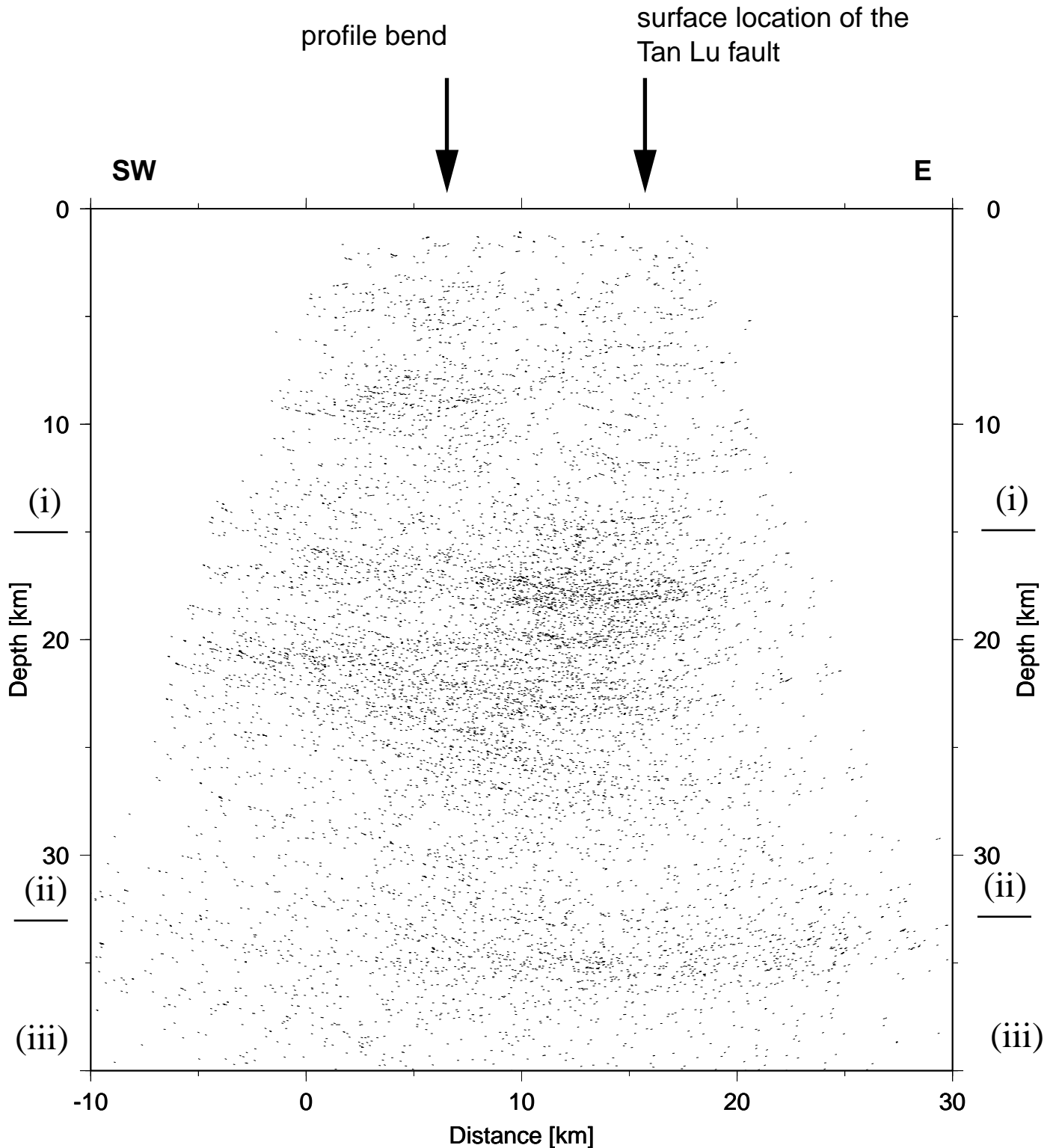
Figure 6: Image of the processed reflection data. Note that distance scale is pinned at 0 and 20 km at the south-western and eastern end of the line, repectively. Migrated line drawing of the stacked image. Migration follows a simple velocity model (V= 6.5 km/s) and results in depth-scale of the section. Note that some reflectors are imaged from regions outside the CDP line. The interpreted crustal reflection zones (i) to (iii) are indicated, see text for discussion of their significance.
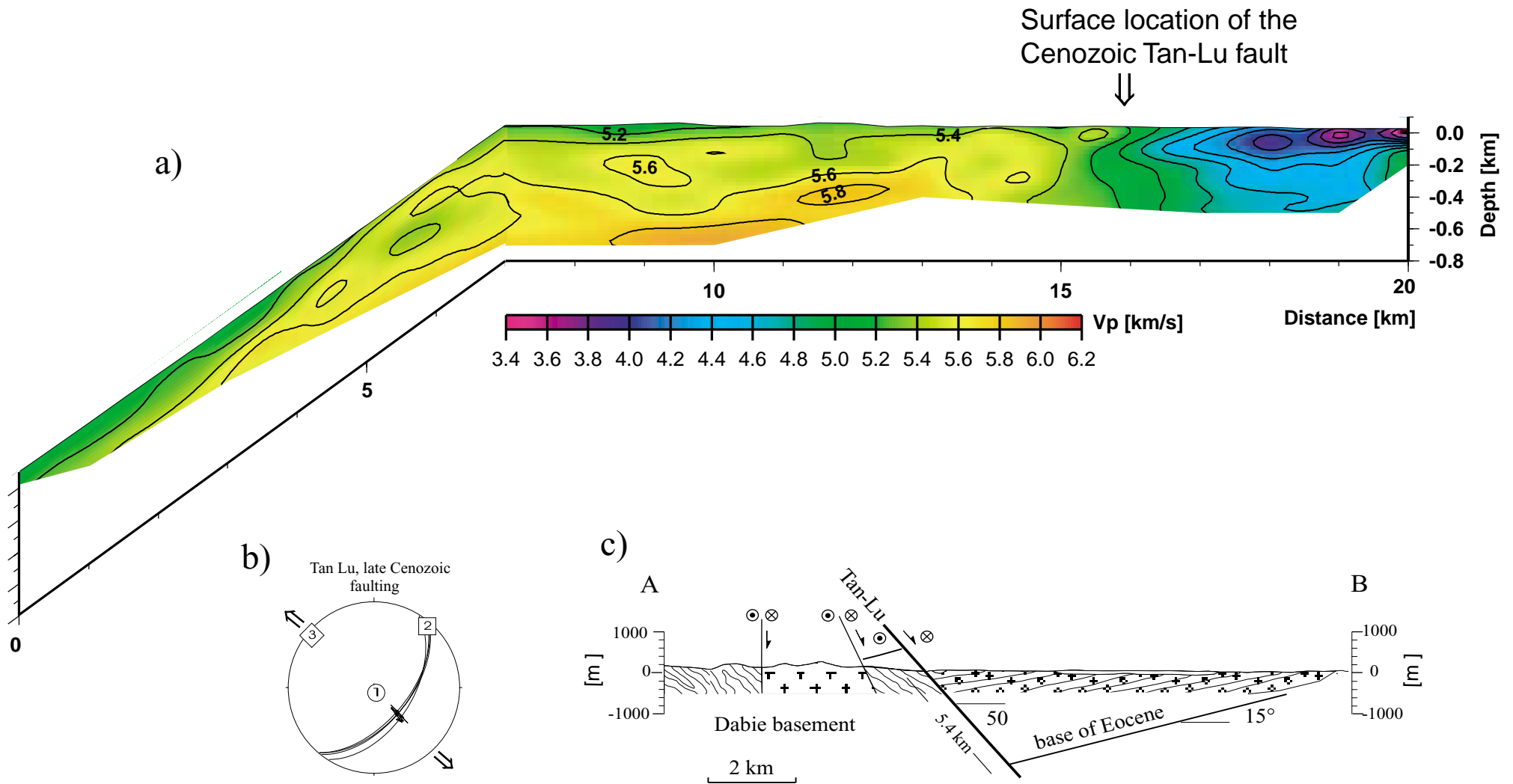
Figure 7: a) Shallow velocity model along the generalised source-receiver line (cf. Fig. 4). P-wave arrival times have been used to derive a velocity model by tomographic inversion. Note the clear separationof a low velocity region east of the Tan Lu fault from a region with increased velocities. The resolution depth of the model is controlled by the depth penetration of the direct waves. b) Last (late Cretaceous) scarp-forming slip event along the Tan Lu fault as observed in Eocene red beds; stereogram plots of fault planes as great circles and displacement directions as arrows with heads pointing in the direction of the movement of the hanging wall block. The average dip of the fault is 50 towards SE corresponding to the observation in a). c) NW-SE cross section normal to the Tan Lu fault (interpreted from1:200,000 Regional Geologic Map of Anhui province and own field data) and minimum slip along the Tan Lu. b) and c) modified from Ratschbacher et al. (2000).

2.3 GEOLOGIC INTERPRETATION

2.3.1 REFLECTION SEISMOLOGY

The short length of the profile line is a severe limitation for the interpretation of the reflectors; their regional geometry, i.e. their distribution with regard to space and true dip, can only be inferred. The line runs in part oblique and in part sub-normal to the fabric of the UHP rocks, whereas the Tan Lu fault system and the sedimentary rocks east of it are observed nearly normal to their strike. This could result potentially in complex intersection relationships. Furthermore, the velocity structure of the observed reflectors is unknown. As the potential of contrasts to be detected by reflection seismology decreases with depth, the deep crustal reflections should be more prominent than they actually appear. Apart from this, the high resolution and the clear and consistent imaging, together with the principal (refraction) velocity structure of the crust (Dong et al. 1997) provide sufficient information for a generalised interpretation of the crustal section.

The occurrence of only few reflectors in zone (i) indicates that the upper crust is seismically more or less transparent and thus rather homogeneous in terms of lithology (i.e. largely dominated by gneisses) at the observed scale. The reflectors appear mainly within the upper western portion of the profile, thus our study is unable to clarify the reflection patterns and therefore the nature of contact relationships across the Tan Lu subsurface. The apparent subhorizontal reflection geometry does not correlate to the known outcrop structures. The 30-50° SE dip of the penetrative foliation (cf. Fig. 4 insets), if picked up by the reflections, should result in a shallow easterly dipping reflectivity in the middle part, and in a subhorizontal or shallow westerly dipping reflectivity along the westernmost part of the line, both is neither clearly nor consistently indicated by the data. From the inferred lithological homogeneity of zone (i) it can be excluded that rocks other than those exposed at the surface, e.g. layers of eclogitized oceanic crust form a major constituent of the upper crust of Dabie. This is in agreement with previous refraction profiles (Gao et al. 1998) as well as surface geology. The absence of characteristic reflection patterns also indicates that nearby granitoid bodies do not extend into the profile. However, a N-S reflection profile would be required to conclusively assess the influence of the

younger granitoids and the distributed SE dipping shear zones which overprint the intrusive granitoid - UHP contacts (Fig. 4).

The transparent upper zone (i) is interpreted to trace a lithologically homogeneous crustal portion, which was involved in the UHP-orogeny, to a depth of c. 15 km, similar to the thickness estimated by Hacker et al. (2000) based on structural reconstructions. Thus a model of crustal imbrication in which a gneissic UHP slab was emplaced on top of Yangtze basement seems reasonable (cf. Chemenda et al. 1996, 1997). A major thrust contact, however, was not imaged.

The transition with depth from the upper to the middle and lower crust (from zones (i) to (ii)) is rather abrupt in both the number and consistency of reflectors. Therefore, it is suggested that the upper crust of UHP rocks is underlain by lithologically and thus seismically distinct rocks which constitute the middle to lower crust of the Yangtze craton (likely granulites, cf. Kern et al. 1998a). The different reflector geometry compared to zone (i) may trace differences in the tectonic evolution. The reported velocity for this region, 6.40-6.63 km*s^{-1} (Dong et al. 1997), implies the dominance of felsic to intermediate crust.

Between zones (ii) and (iii) no sharp boundary exists. The depth of occurrence, 10-12 s (~33-40km), the strength and the consistency of the reflectors within zone (iii) all support the interpretation that they trace the Moho. The data thus further emphasise that an orogenic root related to the UHP orogeny does not exist (cf. Wang et al. 2000; Gao et al. 1998). This implies that the Moho has been reformed and is an effect of post-Triassic tectonics (Ratschbacher et al. 2000).

Overall it can be concluded that the results of the reflection seismic survey are compatible with the existing models of the Dabie Shan, suggesting exhumation and thrusting of a coherent slab on top of a footwall unaffected by the UHP metamorphism.

2.3.2 TOMOGRAPHY

In contrast to the reflection seismology the tomographic inversion clearly reflects the contrasting surface geology across the Tan Lu fault zone to a depth of 500-700m (cf. Fig. 7b, c). The shallow velocities are influenced by the lithology and, of course, by fracturing properties of the rocks. Anyhow, a high-resolution uppermost velocity model can extend the known geology at the surface down into the subsurface. The velocities E of the fault indicate the presence of

sediments and sedimentary rocks, whereas the velocities W of the Tan Lu correspond to the experimentally determined ones for the gneisses of the UHP unit (Kern et al. 1998a, b). The horizontal to shallowly W dipping attitude of isolines in the eastern part traces either the shallow north-westerly dip of the Cretaceous-Eocene sedimentary rocks (Fig. 7c), or results from meteoric weathering effects. The striking changes towards and across the Tan Lu reflect the contrasting rock types and thus image the fault zone as a steeply E dipping structure (Figs. 3, 4).

The tomographic investigations of the rocks W of the Tan Lu demonstrate that detectable bodies (at the applied resolution) of high-velocity rocks, i.e. eclogite or marble, do not occur along the line. This corresponds to the prediction from surface mapping, showing that only small-scale eclogitic enclosures are hosted by the gneissic rocks along the line. Nevertheless, there is, although small (<10%), an increase in velocity toward depth and there are distinct layers and lenses of non-uniform velocity. Whereas the downward increase in velocity and the subhorizontal uppermost layers likely reflect increasing bulk density due to closure of fractures, it is speculated that the velocity variations trace specific structural geometries outlined by distinct rock compositions. This interpretation is guided by features observed in outcrop. Note that the tomography profile is displayed following the crooked field line (Fig. 4); in its western segment it is thus subnormal to the linear structural elements within the UHP rocks. The shape of isolines in the western part may, therefore, represent one of the characteristic structures of the UHP units, i.e. large-scale, isoclinal sheath folds (cf. Hacker et al. 2000). This may indicate that the compositional changes in the UHP rocks are on a first order bound to large-scale structures; the one rock type, which is not reported to contain mafic eclogitic rocks, i.e. the orthogneiss, may represent a major player in forming the velocity differences.

3. FIELD RELATIONSHIPS WITHIN THE UHP UNIT – DEFINITION OF BASEMENT-COVER SEQUENCES

Although the Hong´an-Dabie Mountains have been studied intensively, the detailed field relations of the UHP rocks in this area are hitherto poorly documented (cf. Xue et al. 1996), and their implications to orogeny remain to be established. Up to now there is consensus that HP and UHP eclogites (sensu latu Carswell 1990) and their host rocks crop out over an area of several thousand km^2 and were coevally metamorphosed "in situ" (e.g. Carswell et al. 1997; Hacker et al. 2000). The principal orogenic architecture is dominated by an anticlinal super-structure which suffered some degree of overprint due to Jurassic-Cenozoic extensional processes (Ratschbacher et al. 2000; cf. Figure 3). However, unpublished maps (or maps for internal use in China only; cf. Fig. 8) give more, but not all recognisable details of the field-relations and relevant lithologies. Deciphering and interpreting key field-relationships among UHP rocks is crucial to document the "in situ" metamorphism and to further constrain the petrogenesis of such rocks.

Commonly the UHP unit of the Dabie Shan is loosely described to be composed of gneisses, schists and marble layers or bands, all hosting eclogitic UHP rocks (e.g. Liou et al. 1996). Field and petrographic relationships (e.g. coesite in garnet) indicative of "in situ" metamorphism of the metabasites and metasediments were reported but only few details have been presented (e.g. Wang and Liou 1991; Xue et al. 1996). In contrast, Chinese maps (AIRGS unpubl., cf. Fig. 8) clearly reveal that the field-relationships of the UHP unit are far more complex; e.g., the "marble-formation" (henceforth Changpu Unit) forms a folded, NW-SE trending unit along its northern limit; additionally, local occurrence of the "Ganghe petrologic formation" is given. This unit (henceforth Ganghe Unit) was previously interpreted as "low grade volcanic and sedimentary rocks" (Tang et al. 1995; Dong et al. 1997). Both units are in contact to "grey" gneisses (Rowley et al. 1997) of roughly tonalitic to granitic composition in amphibolite to greenschist facies.

This chapter summarises the results of mapping at the 1:10,000 scale (based on Tang et al. unpubl.) and petrography in order to document that basement-cover sequences present in the UHP unit of the Dabie Shan and thus coherent segments of a former rifted margin of the Yangtze craton underwent metamorphism in the stability field of coesite.
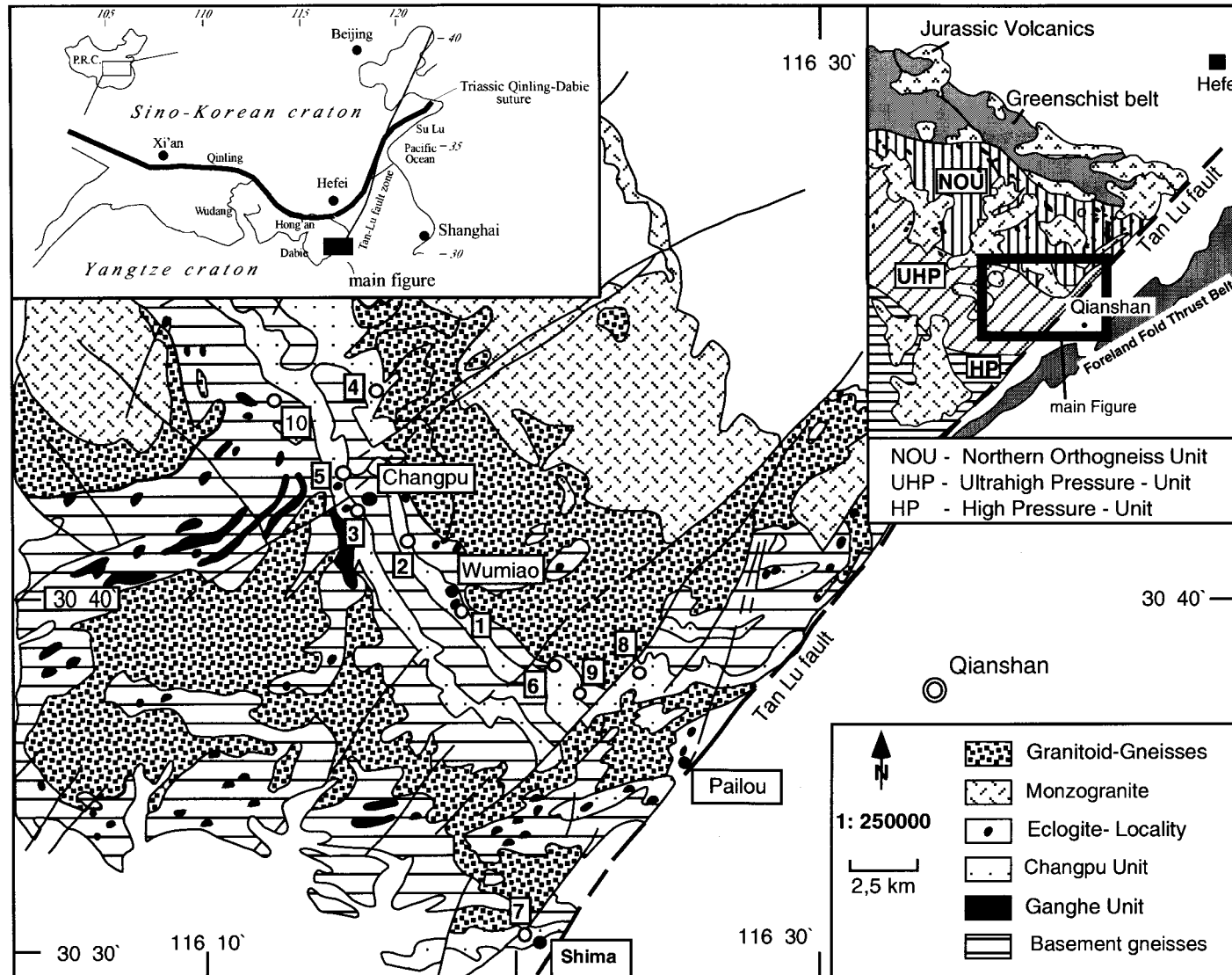
Figure 8: Geological map showing part of the UHP unit of the Dabie Shan. See insets for regional geographical context. Note the NW-SE-trend of the Changpu unit and the local occurrence of the Ganghe unit. Boxed numbers refer to sample locations (cf. chapter 4 and tables A4 and A5). Modified after AIRGS (unpublished).

Figure 9: Photograph showing a thin conglomerate layer on top of the isoclinal folded basement gneisses. The conglomerate forms the base of the Changpu unit (cf. locality 9 in Fig. 8).

Figure 14: Photograph showing an eclogite lens within carbonatic (i.e. calc-silicate) host rocks. Note the corona formation of amphibole and white mica. Locality 1 in Fig. 8.

3.1 THE CHANGPU SEQUENCE

Locally, the isoclinally-folded quartzo-feldspatic "grey gneisses" are observed to be unconformably overlain by a thin layer of strongly deformed conglomerate (cf. Figs. 8, 9). A generalised stratigraphic reconstruction of the section reveals that the conglomerate forms the base of a silici-clastic succession passing into carbonates, calc-schists and finally pelites (Figs. 10-13). Thus, the gneisses are defined here as a basement relative to the overlying (meta-) sediments. Both gneisses and metasediments are interlayered or cross-cut by mafic rocks (in eclogite-facies) interpreted to represent former lavas, tuffs or dykes.

The basement gneisses exhibit overall amphibolite- to greenschist-facies mineral assemblages, however in the village of Yehe (cf. Fig. 8; location 10), in one profile, gneissic rocks preserving eclogitic minerals (i.e. felsic-gneissic eclogite) were recognised. The section exhibits a penetrative foliation, well defined by aligned white mica, feldspar, retrogressed basic lenses and in the eclogitic portions phengite, quartz-ribbons, garnet, symplectites after omphacite and rutile. Furthermore, these rocks bear phengite-eclogite lenses. Despite the obvious differences in metamorphic grade only one foliation is observed in this outcrop. This implies that the strain-field did not change significantly from the eclogite- to the greenschist-facies but deformation/retrogression appears to have localised in such a manner that eclogite-, amphibolite- and greenschist-facies minerals and textures were produced and preserved in different portions of the rocks. P-T estimates from gneisses and eclogite-facies rocks reported so far (cf. Carswell et al. 2000; Tabata et al. 1998) and also outlined below are clearly compatible with UHP conditions.

Pristine eclogite- to greenschist-facies metabasites of the Ganghe Unit occur within, and are frequently interlayered with, partly impure dolomitic and calcitic marbles (i.e. omphacite-, phengite-, coesite-, rutile-bearing calc-silicate rocks) and locally with coesite-, garnet-, kyanite- and jadeite-bearing quartzites (the latter likely former "coesitites").

Metabasites form either small lenses (cm-dm), layers (up to 2 metres thickness) or patches (dm-m) within the calc-silicate rocks, both ranging in metamorphic grade from eclogite to greenschist facies. Contact relations observed among the rock-types indicate that they shared a common tectono-metamorphic evolution. Contacts between deformed, virtually fresh eclogite lenses and calc-silicates are characterised by a concentration of aligned phengite flakes, pointing to syn- and post-tectonic growth (Fig. 14). Compositional boundaries between eclogite and calc-silicate rocks are often sharp (Figs. 15, 16) but also diffuse. Others display multi-shell coronas of additional hydrous minerals such as amphibole,
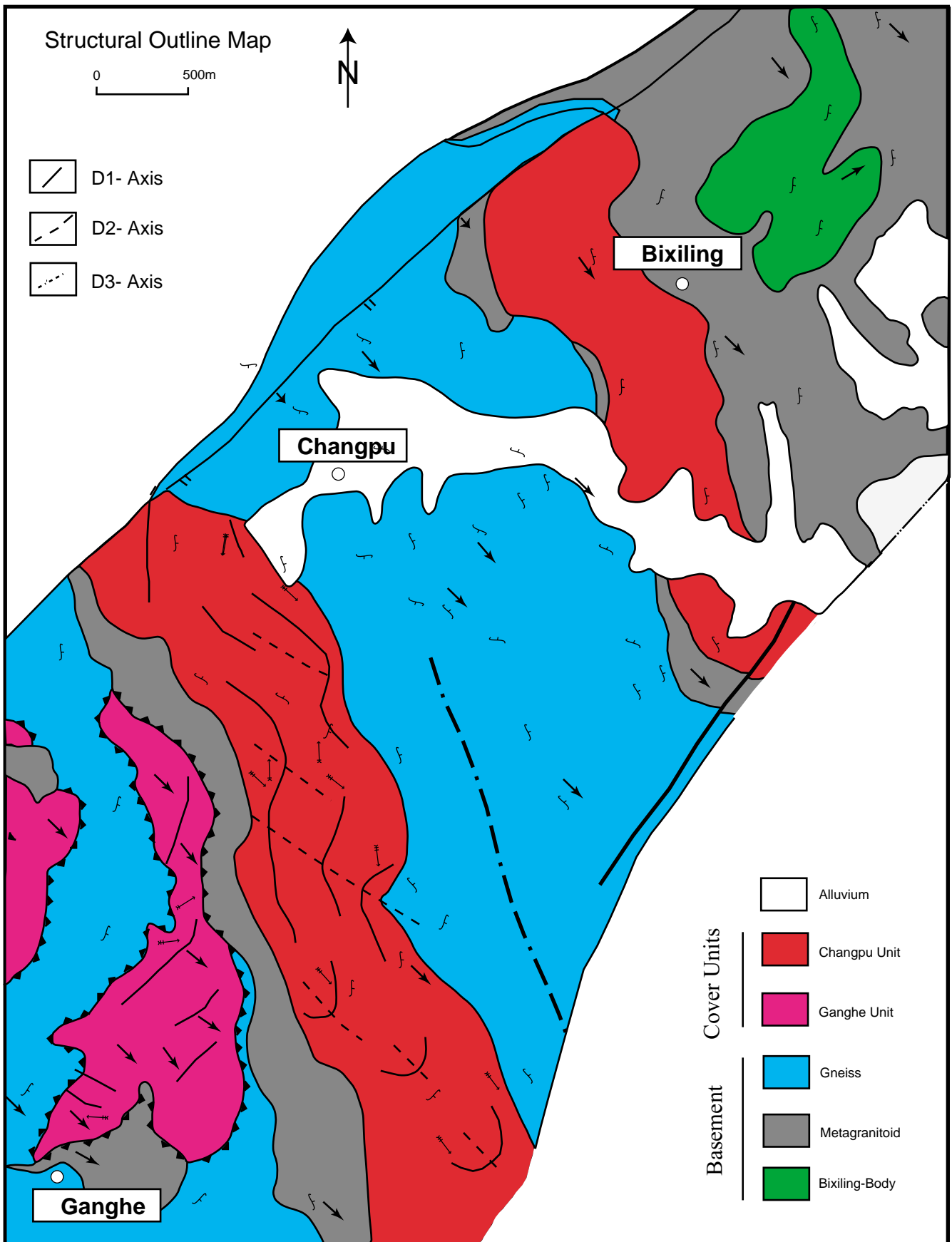
Figure 10: Litho-tectonic sketch map of the Changpu and Ganghe area (cf. Fig. 8) compilied from Tang et al. (unpubl.) and own field data. Note the different generations of fold axes, lineations foliation directions present in the basement and the cover units. See also text for discussion.

conglom. + sst

interlayer of marble/Sst
calcarenit + mafic dykes
(boudinaged Eclogite)

Mylonite

Ecl ->
Amph

basement

volcanic sediment

volc. conglomerate

N

0   0.5

[km]

Mylonite

Pillows
dyke
Mylonite

Pillows

massive Eclogite

Ecl
dyke

def. volcanoclast.
weak to undef. volcanoclast.

retro Ecl

def. volcanics

cherts
Pillow Ecl.

Ecl.

Ecl.

def. mica schist
lam. Sed

Ecl.

def. mica schist
Mylonite with Blasteses

Figure 11: Schematic geological section of the Ganghe unit along the Ganghe river (cf. Figs. 10, 12).
See also text for discussion.

Post - UHP

- ☐ Alluvium
- ☐ porphyritic dyke
- ☐ Porphyric granite

Changpu Unit

- ☐ Eclogite
- ☐ Marble
- ☐ jadeite-"coesitites"
- ☐ Garnet- biotite plagioclase Gneiss

Ganghe Unit

- ☐ Leptite
- ☐ Volcanic breccia
- ☐ Acidic ash layers
- ☐ Phyllite
- ☐ Muscovite plagioclase gneiss
- ☐ micaschist
- ☐ Eclogite

Basement

- ☐ Eclogite
- ☐ Two mica plagioclase gneiss
- ☐ Gneisses
- ☐ Biotite plagioclase gneiss
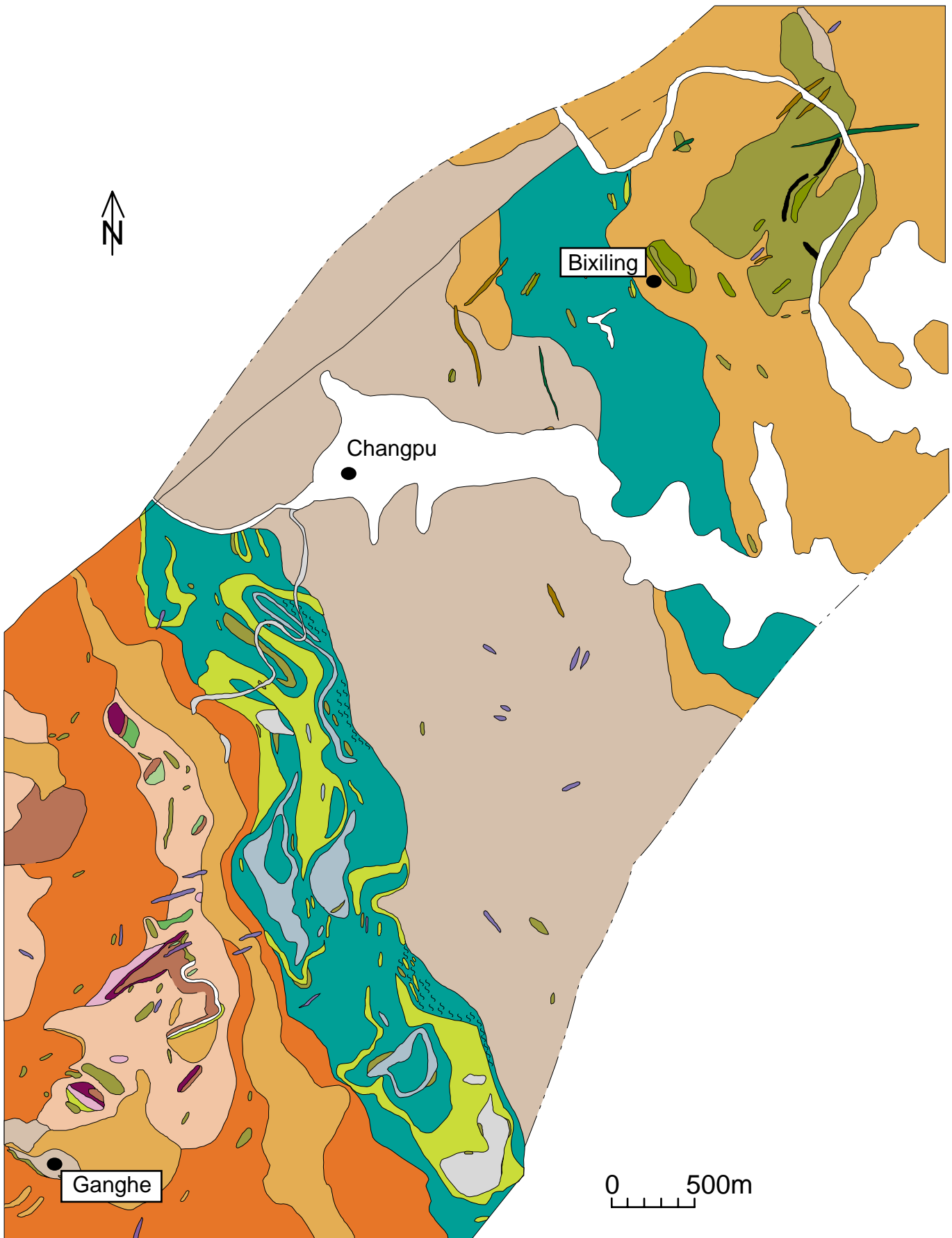
Figure 12: Geological map (1:10,000) of the Changpu-Ganghe area (modified after Tang et al. unpubl.).

epidote, rare chlorite and carbonate which is in part accompanied by pronounced retrogression of the basites. Locally, contacts between fractured metabasites and a foliated carbonate matrix can be observed (Fig. 16, 17).

The basal conglomerate layer on top of the gneisses is direct evidence for the onset of clastic sedimentation on top of an erosive surface (cf. Figs. 9, 13). Hence the gneisses form a basement which already had a metamorphic history predating deposition of the sediments. Such a rock-association is typical of a stratigraphic basement-cover sequence prior to any tectono-metamorphism (e.g. Press and Siever 1986), thus the Changpu unit (metasediments) together with the "grey" basement gneisses are defined here as the Changpu-sequence (suggested here to be named after the place where this idea was born). Occurring lithologies (clastics together with carbonates) indicate deposition within a young, rapidly subsiding but shallow basin. The HP-LT metamorphic overprint locates it likely at a rifting, thus thinned passive margin and later leading edge of the Yangtze craton during the Triassic collisional stage. The age of this rifting event, ca. 800 Ma., is alleged by Rowley et al. (1997) to be reflected by the volcanic origin of grey gneisses. However, such a large amount of felsic volcanics, as represented by this abandoned rock is unlikely within a rift.

3.2 THE GANGHE UNIT

In the area of Ganghe (cf. Figs. 8, 10, 11) a distinct and thus second cover unit is recognised. This unit is chiefly constituted by volcano-sedimentary rocks. In its lower portions it is characterised by a series of various sandstone with conglomerate layers/pockets, and coarse- to fine-grained felsic volcanoclastic rocks in part cross-cut by mafic dykes; cherts, pillow lavas, intermediate to mafic flows and tuffs, acidic ash layers, pelites and marls are present in the upper portion (cf. Fig. 13). Field observations and map relationships indicate that in this unit the original stratigraphy is exceptionally well preserved, which is documented in a generalised section along the Ganghe Valley (cf. Figs. 10, 11). Furthermore, the different lithologies are characterised by a particularly strong variation in metamorphic grade. A HP metamorphic overprint is reflected by in part compositionally layered, eclogite-facies metabasites. The acidic rocks do not reflect this HP event and range from texturally pristine and apparently non-metamorphic felsic volcanic breccias and ash-layers with syn-sedimentary structures to greenschist-facies meta-sandstones. However, a common tectono-metamorphism is evident from field-relations. The andesitic-felsic volcanic breccia, e.g., is cross cut by an eclogite-facies basic dyke which preserved eclogitic minerals in the outer portions while the
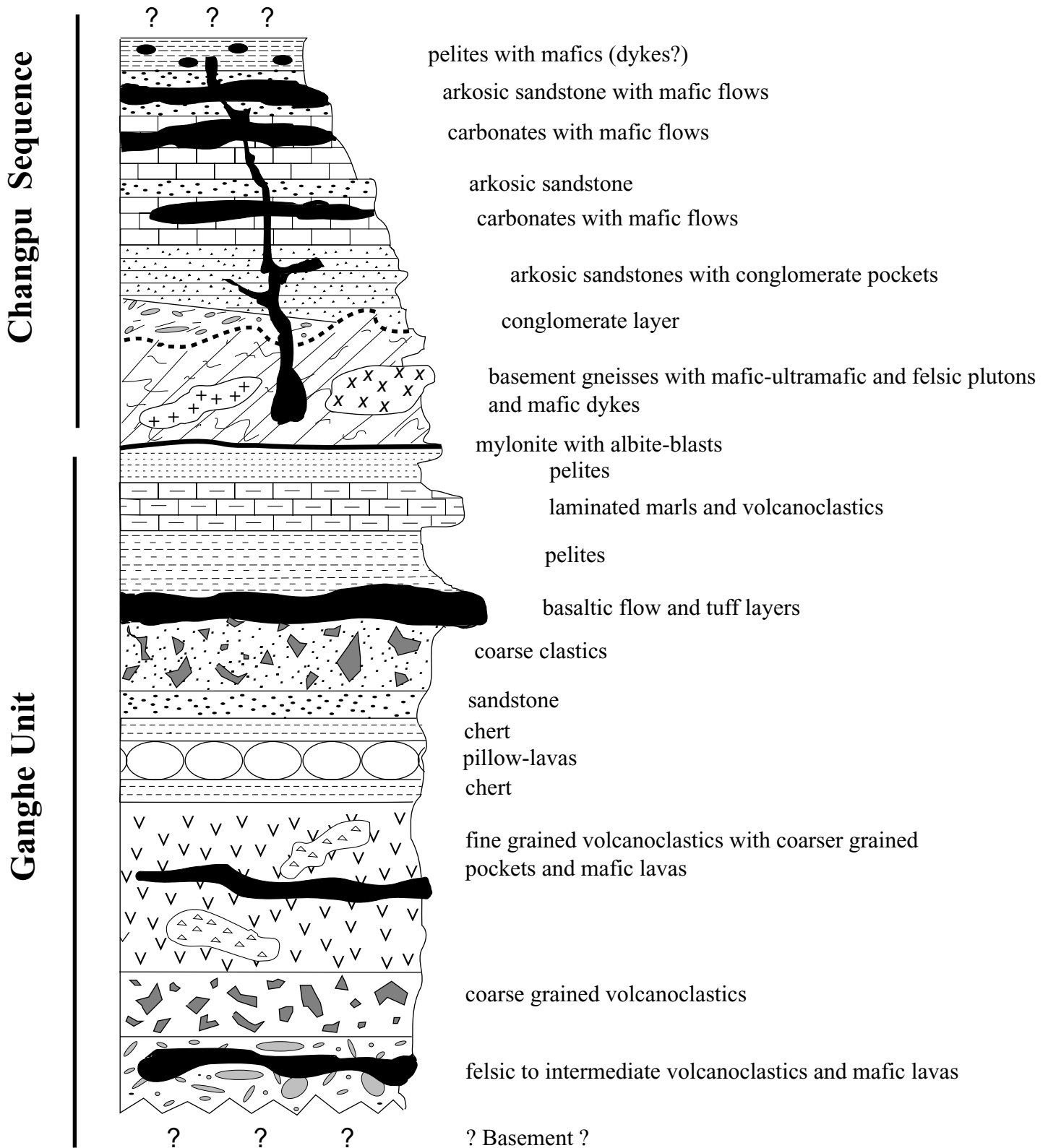
Figure 13: Schematic reconstruction of the pre-UHP stratigraphy of the basement-coversequences (Ganghe Unit and Changpu Sequence) compiled from own field data and AIRGS (unpubl.). Note the principal differences in lithology (volcanoclastic vs. clastic-carbonatic) and the stratigraphic positions of the basites. Occurring lithologies indicate formation within an initial continental rift setting (volcanoclastic) and within a shallow basin (clastic-carbonatic). **Not to scale.**

Figure 15: Photograph showing the contact of a metabasite lens with its carbonatic host rock. Note the sharp boundary and the texture of the two rock types, the metabasite is retrogressed and fine grained, whereas the marble is coarse grained but also retrogressed.

Figure 16: Photograph showing a boudinaged and retrogressed basite in marble which in turn is enclosed in mafic portions. "Diamond-locality", where Xue et al. (1992) obtained micro-diamond from eclogite. Note that 50m downstream is the stratigraphic contact of the Changpu unit and its basement, locality 9 in Fig. 8, cf. Fig. 9.

centre is retrogressed to a greenschist-facies assemblage. Petrography, microprobe and X-ray data revealed no high pressure relics in the breccia components (andesites). Thus it becomes obvious that the metamorphic grade is not solely controlled by the P-T conditions experienced. More critically are therefore the kinetic and compositional controls on mineral reactions, i.e. whether or not fluids are present/available during metamorphism. Something already previously recognised by e.g. Austrheim (1987, 1998), who proposed overstepping of reaction boundaries in the order of 5 kbar, however, in the light of the preserved sediments (felsic volcanics) it seems that in fluid-absent systems a pressure overstepping in the order of 20-40 kbar is possible.

Although the contact to its basement is not exposed, the top of the Ganghe Unit is in contact to the Changpu-basement via a blasto-mylonite, allowing its definition as a tectonic window (cf. Figs. 10, 11, 12). The mylonite occurs solely at the contact to the Changpu-basement and is up to one metre thick. It comprises a foliated two-mica-epidote-albite gneiss in greenschist-facies with preserved relics of porphyroblastic albite, pointing to greenschist - facies P-T conditions during formation.

The association of clastic sediments and the first report of bimodal volcanics, classifies the Changpu Unit as a typical cover sequence, indicating formation within an initial rift setting within the Yangtze craton. Support for this comes from single zircon ages of c. 700-750 Ma. (Romer, unpublished data obtained from andesitic lithoclasts of the volcanic breccia) post-dating the commonly reported Yangtze consolidation ages of ca. 800 Ma (Rowley et al. 1997).

3.3 DEFORMATION HISTORY

Structural observations reveal that the basement gneisses, the Changpu and Ganghe Units differ in their tectonic record (cf. Fig 10). Figure 9 illustrates that the gneisses locally display at least one earlier phase of deformation, which is expressed by an isoclinal fabric ($D_{<1}$) unconformably overlain by metasediments. Furthermore the mafic-ultramafic Bixiling Complex (cf. Fig. 10) and the immediate gneisses display an ESE-dipping foliation trend, which is oblique to the penetrative fabric. Compositional layering in the Changpu and Ganghe units is of sedimentary origin and transposed into open to isoclinal, SSE-SW-plunging folds (D_1). Refolding of the D_1-axes by folds with SE-plunging D_2 axes is solely observed within the Changpu unit and not observed in the Ganghe Unit. Penetrative ductile fabrics of D_3 (SW

to S dipping foliation and SSE plunging, <a>-type fold-axes) are present in the gneisses (cf. Hacker et al. 1998, 2000) and is evident from the map relations of the Changpu unit (Fig. 10).

The distinct tectonic record and occurrence of the mylonite, bounding the Ganghe unit, suggests a separate tectonic evolution of the two metasedimentary units during orogeny and juxtaposition at a relatively late phase of uplift in the greenschist-facies.

3.4 DISTINCT TYPES OF METABASITES

Field observation and petrography also allow definition of three types of metabasites occurring in the UHP unit. Kyanite- and coesite-bearing (cf. Fig. 18) eclogitic rocks preserving coarse-grained plutonic textures are recognised to be confined to the Changpu-basement. Although variable in size and colour, they are of the "Bixiling type" (e.g. Chavagnac and Jahn 1996), i.e. occasionally associated with ultramafic portions and in part prograde talc-, or retrograde paragonite-bearing. They occur as massive, m- to km-sized bodies within the gneisses (cf. Fig. 10). If present, similar deformation style in the gneisses and metabasites implies a common deformation. The eclogites and the ultramafic rocks must likely represent gabbroic intrusions and their cumulates emplaced into a felsic crust prior to UHP metamorphism. In contrast, other eclogite-facies metabasites occur as cm- to m-sized lenses and/or continuous layers and irregular shaped patches within both the cover units and the gneisses. They usually have a massive metamorphic texture and are further distinguished by abundant phengite, carbonate and qtz/coe as matrix phases and inclusions in eclogitic minerals. Occurrences of pillow structures, intercalation with the metasedimentary rocks and in particular the deformation style (boudinage vs. ductile recrystallisation due to rising and falling competence contrast during pro- and retrogressive recrystallisation, respectively, cf. Figs. 14-17, 19) implies that they originated from basaltic dykes and/or lava flows. In particular for sample Dab 9933 from the Ganghe Unit the original nature of a basic dyke is still recognisable in the field, where it cross-cuts the volcanic breccia. Thus this type of metabasite likely represents basaltic rocks which were emplaced during a rifting stage. Finally, metabasites exhibiting a mm-cm-scale compositional layering and a strongly preferred orientation of the eclogitic mineral phases are recognised in the gneisses and the Ganghe Unit (samples Dab 99206). They do not differ in their principal mineral assemblages from the basaltic eclogites, however they are usually less coarse grained than the former basites and bear larger quantities of kyanite, zoisite and/or epidote-group minerals aligned in the foliation. Their compositional layering may be due to penetrative metamorphic

Figure 17: Photograph showing partly fractured metabasite in a ductile carbonatic matrix.
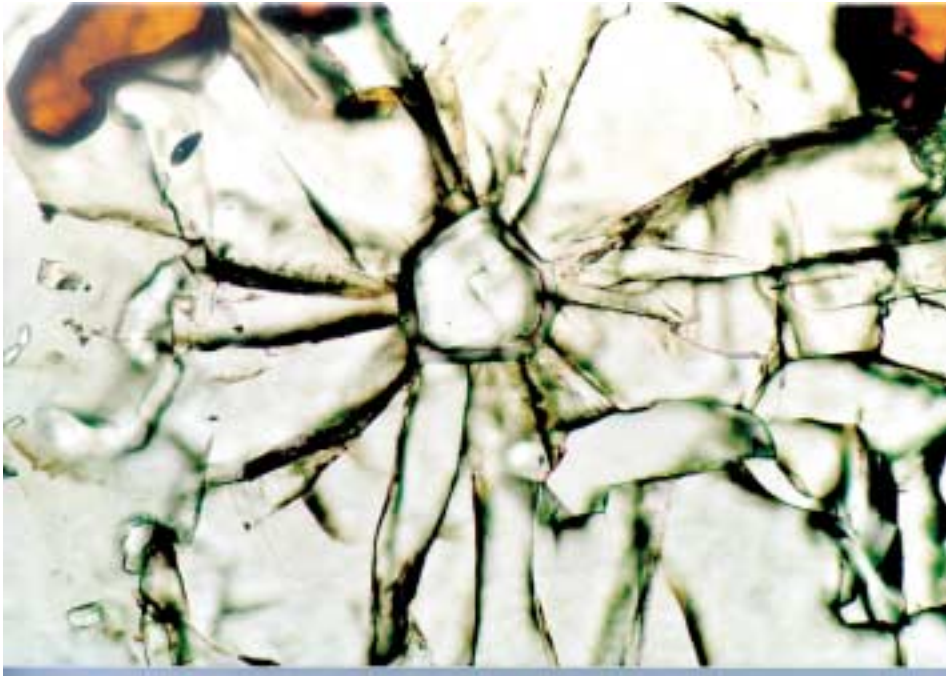
Figure 18: Microphotograph showing a coesite inclusion within garnet of gabbroic eclogite sample Dab 99178. Note the replacement of coesite by quartz at inclusion rims. PPL, long side is approx. 0.88 mm.

differentiation or to their protolith nature, i.e. originating from mafic tuffs. The latter seems more likely, because a fine-grained sediment is expected to be more easily converted into a foliated metamorphic rock with shape alignment of its minerals.

4. ECLOGITE, ECLOGITE-FACIES AND NON-ECLOGITIC ROCKS

Mineral chemistry and thermobarometry of eclogite-facies rocks from the Dabie Shan has been presented and applied in a number of studies, establishing the principal metamorphic paths of the rocks and proposing models for the lithospheric collision and exhumation (e.g. Wang and Liou 1993; Eide 1995; Liou et al. 1996). However, only a few papers have defined and addressed different types of eclogite-facies rocks (sensu Carswell 1990) present in the Dabie, and furthermore the zonation patterns of their minerals used for the calculation of their specific P-T conditions are so far not well documented in detail (cf. Okay 1993; Carswell et al. 2000; Schmid et al. 2000). Hence, the reliability of absolute pressure-temperature conditions recorded in these rocks, and in particular the potential spatial variation of them in the light of different rock types and their field relations (cf. Chapter 3) are less well constrained.

Pressures experienced by bi-mineralic (garnet and omphacite) eclogites are commonly determined via the jadeite content in omphacite (Holland 1980, 1990) or the occurrence of critical index-minerals like coesite (Bohlen and Boettcher 1982) and/or diamond (Berman 1979, Chatterjee 1991) or their pseudomorphic replacements. Therefore, only minimum pressures are estimated in most cases, whereas metamorphic temperatures can often be constrained in a much better way (Fe-Mg exchange, e.g. Krogh 2000a). Some eclogite-facies rocks, however, including the ones under consideration, offer more possibilities for determination of the P-T regime because they are not eclogites sensu strictu (Carswell 1990).

Recently, Waters and Martin (1993) derived a geobarometer based on the Tschermaks exchange between garnet, omphacite and phengite, thus delivering a promising tool for the determination of absolute pressures in phengite-bearing eclogites (e.g. Wain 1997). Thus, this chapter focuses on application of this barometer, although additionally cation exchange thermometry and net-transfer reactions are evaluated to constrain in particular the peak P-T conditions of the rocks stemming from the different units defined above. Evaluation of the peak conditions is crucial for understanding the field-relations of such rock-types, constraining a common metamorphic path, exploring the thermal and physical regimes in orogenic roots and thus reconstructing the subduction and exhumation path of the Dabie in better detail to establish boundary conditions for tectonic models.

Evaluation of the Ferric Iron Content of Garnet, Omphacite and Phengite

The Fe^{3+}/Fe^{2+} ratio present in the minerals used for thermobarometry is an important issue (see, e.g., Carswell et al, 1997, 2000 for discussion). Standard charge balance methods for the microprobe analyses of Fe-poor omphacite (e.g. Droop 1987) and phengite (e.g. Schliestedt 1980) revealed inconsistent values, resulting, if applied, in unsystematic and unreasonable temperature calculations. However, some omphacite from samples of the Ganghe Unit revealed a higher Fe_{tot} and also less variable Fe^{3+} contents by charge balance than others.

In order to enlighten the "iron-problem" the estimation of the Fe^{2+} contents for omphacite from an eclogite (Dab 9872) and for omphacite from a calc-silicate sample (Dab 98408) were approached by means of wet chemical titration methods. Two rock chips where hand-crushed and the calc-silicate sample was put overnight in 10% HCl for carbonate dissolution. Mineral separates were obtained by multi-step sieving and hand picking under a binocular microscope. Two runs of standard titration methods revealed 2.03 wt.% ($\pm$ 0.1) Fe^{2+} for omphacite in Dab 9872, whereas omphacite in Dab 98408 was analysed to have 2.36 wt.% (± 0.16) ferrous iron. Contents of the ferric iron where then calculated with the mean Fe_{tot} (Dab 9872: 3.13 wt.%; Dab 98408: 2.91 wt.%) as analysed with the EMP from all grains from each of the two samples. Thus, the omphacite of Dab 9872 yields 35 % and the one in sample Dab 98408 has 19 % Fe^{3+}/Fe_{tot}.

A Fe^{3+}/Fe_{tot} ratio of 0.5 for Dabie Shan omphacite was reported in Carswell et al. (2000) from the Bixiling eclogite-body; this, together with the values presented here, indicates that the Fe^{3+} contents in omphacite may vary considerably among eclogite localities in the Dabie Shan. Such local disequilibria of oxygen fugacity are handled here by "adjusting" the Fe^{3+} content in the mineral formulas used in the single calculations. However, in order to be consistent among groups of samples studied here, and with regard to potential analytical errors due to zoning of Fe^{3+} in omphacite, the Fe^{3+}/Fe_{tot} ratio for most calculations is fixed conservatively to 0.5, except for samples from the Ganghe Unit where the ferrous iron is assumed "from-case-to-case" with respect to the higher Fe_{tot} values and charge balance results from the corresponding analyses. From the thermobarometric results outlined below it seems reasonable to do the same for phengite, whereas the values obtained by charge balance for the garnet analyses are used in the P-T calculations. Potential overestimation of Fe^{3+} for omphacite and phengite would result in lower temperatures calculated from the corresponding analyses. Pressure estimates, however, are only

marginally affected by Fe^{3+} contents, because the barometer mainly used below (garnet-clinopyroxene-phengite) does not consider a Fe-endmember reaction.

Applied Methods

Mineral analyses were obtained from Cameca SX 50 and SX 100 electron microprobes at the GFZ Potsdam as well as on a JEOL 8800 electron microprobe at the Humboldt University in Berlin with standard conditions of 15 kV, 20 nA and counting times of 20 s for all elements. Natural and synthetic standards were used for calibration procedure.

In order to evaluate metamorphic temperatures, the following Fe-Mg exchange equilibria were applied: (i) garnet-clinopyroxene (Powell 1985, used for garnet with $X_{Ca < 0.35}$; Krogh 2000a, used for garnet with $X_{Ca > 0.35}$), (ii) garnet-phengite (Green and Hellman 1982), (iii) garnet-amphibole (Graham and Powell 1984; Krogh 2000b). Metamorphic pressures were mainly calculated using the equilibrium:

$3KAl_3Si_3O_{10} (OH)_2 + 6 CaMgSi_2O_6 \Leftrightarrow Mg_3Al_2Si_3O_{12} + 2Ca_3 Al_2Si_3O_{12} + 3 KMgAlSi_4O_{10}(OH)_2$

3 muscovite + 6 diopside $\Leftrightarrow$ pyrope + 2 grossular + 3 celadonite
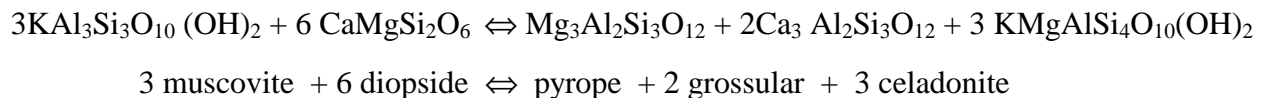
calibrated by Waters and Martin (1993, updated 1996) considering the recommendations by Carswell et al. (1997, 2000), i.e. using the activity models of Newton and Haselton (1981) for garnet, that of Holland (1990) for omphacite, and assuming ideal mixing in phengite with

$a_{inv. Phe} = X_{Al M1} \times X_{Al T1} / (X_{MgM1} \times X_{SiT1})$.

With the help of the TWQ program of Berman (1991; Ba1995a, Ba1996 database) further focus is placed on the equilibria:

- grossular + almandine + 2 $SiO_2 \Leftrightarrow$ 2 kyanite + 3 hedenbergite
- pyrope + grossular + $SiO_2 \Leftrightarrow$ 2 kyanite + 3 diopside
- jadeite + kyanite + $H_2O \Leftrightarrow$ paragonite
- 3 grossular + 5 rutile + 2 $SiO_2 + H_2O \Leftrightarrow$ 5 titanite + 2 zoisite
- coesite $\Leftrightarrow$ α-quartz
- kyanite $\Leftrightarrow$ sillimanite $\Leftrightarrow$ andalusite

The following activity models for calculation of the latter mineral reactions were applied:

Garnet – quaternary regular solid solution (cf. Hodges and Spear 1982)

Clinopyroxene – 2-site mixing with regular solid solution employing the "ax" program of Holland (unpublished, and references cited therein)

Titanite – a = $X_{Ca} * X_{Ti} * X_{Si} * (X_O)^5$, with $X_O = (5-X_{Al} - X_{Fe3+})/5$ (cf. Carswell et al. 2000)

Zoisite – a = $X_{Ca}^2 * X_{Al}^2 * (1-Fe^{3+})*X_{Si}^3$ (cf. Carswell et al. 2000)

Paragonite – non-ideal; using the "ax" program of Holland (unpubl.)

SiO_2, Alumo-silicates, rutile, albite, H_2O - fixed at 1

The fluid phase, if involved, was assumed to be pure, i.e. $X_{H2O} = 1$

Assumptions

Using the "true" compositions for thermobarometry involving minerals which are assumed to form a textural equilibrium, is a difficult issue, thus some assumptions have to be made prior to calculation. The low variation in chemical composition in central parts of most of the garnet (cf. below) is interpreted to be diffusion controlled during high-grade metamorphism, whereas the rims and also smaller grains record to variable degree a retrogressive overprint. On the other hand one sample (Dab 9854, cf. below) exhibits a compositional pattern compatible with growth zoning. However, the in part complex zonation patterns are not straightforward with respect to simple core-rim relationships. Thus, the activity value for garnet (i.e. $a_{py} * a_{grs}^2$) used for the geobarometry of Waters and Martin (1993), may serve as a better tool to evaluate the "peak" composition of the garnet. In plots of compositional microprobe profiles for garnet, omphacite and phengite, the used activity value is plotted with an exaggerating factor, thus systematic vs. erratic variations in composition can easily be visualised (cf. Carswell et al. 2000, and pers. comm.). Due to the algorithm of the geobarometer, higher activity values for garnet, but lower ones for omphacite and phengite, result in higher pressures, thus analyses with the maximum and minimum values, respectively, were chosen to calculate the PT climax. For omphacite and phengite, the evaluation of peak compositions is somewhat easier. Because they have clearly distinct cores and rims it is reasonable to assume that the cores reflect equilibrium composition during the peak stage and that the rims originated from retrogressive modifications. In order to be consistent, the analyses of garnet, omphacite and phengite used for pressure calculations were also used for temperature calculations (garnet-clinopyroxene and garnet-phengite). The upper stability limit for kyanite is evaluated using the peak compositions, whereas paragonite formation is assumed to be related to the jadeite content in the rims of omphacite. For the titanite- and zoisite-forming reactions, analyses which calculate the highest activity for the two phases are used. Although this is somewhat arbitrary, it is justified by the interpretation of resulting in

"maximum minimum-pressures". The assumption of a pure aqueous fluid (i.e. a_{H2O}, $X_{H2O} = 1$) during the peak and retrogressive metamorphic stages is not evident from the presented data, especially for the calc-silicates any contribution of CO_2 is ignored, thus fluid involving reaction-equilibria may shift with regard to future knowledge concerning the fluid composition. In general, lower H_2O activity would move the reactions towards lower P-T conditions. However, fluid-inclusion studies on HP eclogite-facies veins and eclogitic host rocks (Franz et al. in press), from samples of the Bixiling UHP eclogite complex (You et al. 1996; Xiao et al. 2000) and preliminary data from various UHP eclogite samples (Klemd et al. in prep.) support the assumption of a dominantly hydrous fluid phase.

4.1 PETROLOGY OF BASEMENT ROCKS

4.1.1 PETROGRAPHY

Samples from the basement are classified based on their hand-specimen textures into gabbroic, basaltic and gneissic eclogite as well as gneisses. The full range of observed mineral assemblages are listed in Table A1, however only the major phases and textures which are important and also used in the mineral chemistry and thermobarometry sections are discussed.

One small eclogite body (ca. 10x5 m) is hosted by, and shows alignment within the foliation of, the surrounding gneisses and is the source of sample Dab 99178. The sample preserves a gabbroic texture with up to mm-sized mineral grains showing no preferred orientation. They exhibit a granoblastic, equigranular texture with straight grain boundaries, often intersecting at a 120° angle at thin-section scale. The eclogitic paragenesis consists of garnet, omphacite, kyanite, rutile and relict coesite inclusions in garnet and omphacite (cf. Fig. 18). White mica (paragonite), bluish-green amphibole, clinozoisite/epidote, quartz and carbonate occur solely in the matrix and on fractures showing irregular grain shapes or corona-textures around garnet, indicative of their formation at the expense of the primary UHP minerals. Furthermore, omphacite shows at its margins symplectitic intergrowths, indicating the common breakdown-reaction together with SiO_2 and an aqueous fluid phase to form ab-rich plagioclase and amphibole.
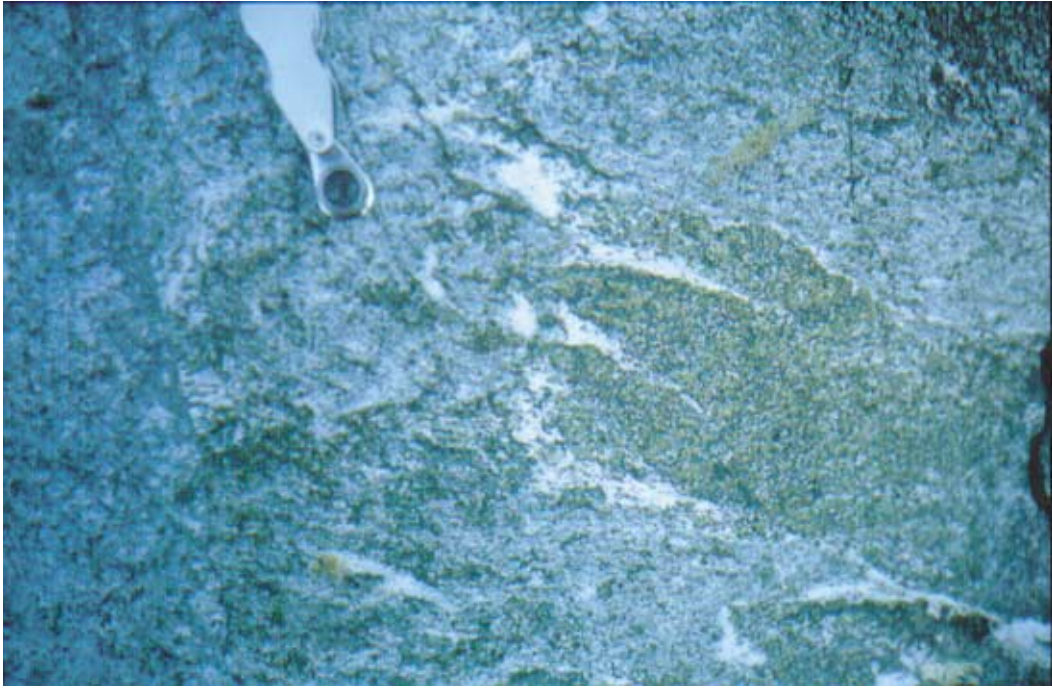
Figure 19: Photograph of a boudinaged and subsequent retrogressed metabasic layer (dyke) within the basement gneisses.
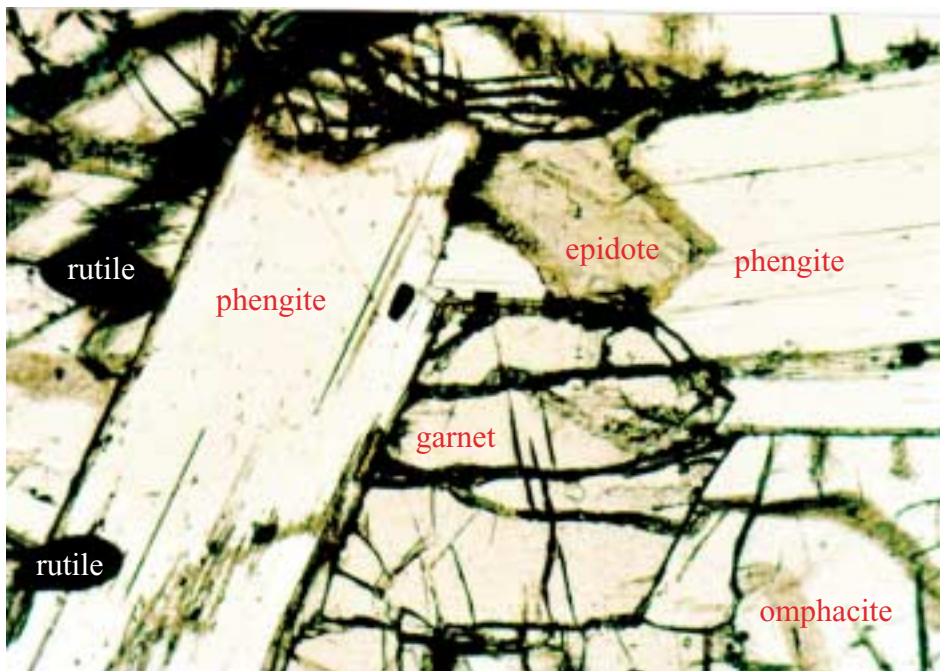

Figure 20: Photomicrograph showing the eclogitic parageneses (grt, omp, ph, rt) beside late epidote of sample Dab 99102. PPL, long side is 5.4 mm.

Lensoid or angular bodies of eclogite (up to dm size) occur in the immediate vicinity of, and are aligned within the foliation of, the gneissic eclogite and gneisses (below). Their shape implies that they are metamorphosed boudins of former dykes (cf. Fig. 19). In contrast to the above described type, pristine eclogite sample Dab 99102 is less coarse grained and further characterised by a lack of kyanite, but abundance of white mica (phengite) as inclusions and as a matrix phase in addition to garnet, omphacite, rutile and coesite-inclusions. The minerals are more or less equigranular and mainly omphacite exhibits a preferred orientation although some domains are randomly intergrown. Garnet, omphacite and phengite are often well preserved, however, garnet and omphacite are intensively fractured; a feature lacking in phengite (cf. Fig. 20, 21). Some epidote and amphibole formed at garnet rims and symplectites of biotite and plagioclase replace the white mica at its margins. Rutile is partly rimmed or replaced by titanite aggregates. The overall amount of retrogression present in this sample is limited, thus no granoblastic plagioclase, biotite or epidote are present. However, other metabasic lenses are fully converted to greenschist-facies assemblages.

The gneissic eclogite samples (Dab 9837 and 99101) are distinguished from the former types by only relict occurrences of omphacite as inclusions in garnet (Fig. 22). However, frequent intergrowths of plagioclase and green amphibole apparently replace abundant former omphacite grains (cf. Fig. 23). Furthermore, larger quantities of polycrystalline quartz-ribbons/aggregates with wavy extinction, zoisite, white mica and rare orthoclase are observed in the matrix together with rutile and epidote-bearing garnet. Coesite or unequivocal quartz-pseudomorphs are not identified in these samples, but the quartz-ribbons often posses coronas of amphibole or plagioclase in the vicinity of symplectites after omphacite and phengite (cf. Fig. 24), indicating the presence of SiO_2 prior to the formation of the corona phases. The gneissic eclogite is compositionally layered with alternating mafic and felsic/silicic domains. The foliation of the hosting gneisses is parallel and the two rock types have a diffuse rather than sharp compositional contact zone. Layered eclogitic domains within the hosting gneisses (up to m-thickness and continuous for tens of metres) may represent an inhomogeneous protolith, likely Tuff.

Gneiss samples Dab 99103 and 99104 were collected with progressive distance from the former two rock types. A variation in the foliation was not observed but the mineral assemblages change accordingly. Thus garnet and apparent textures after omphacite are less abundant but show some degree of recrystallisation as evident from coarser amphibole-plagioclase intergrowth
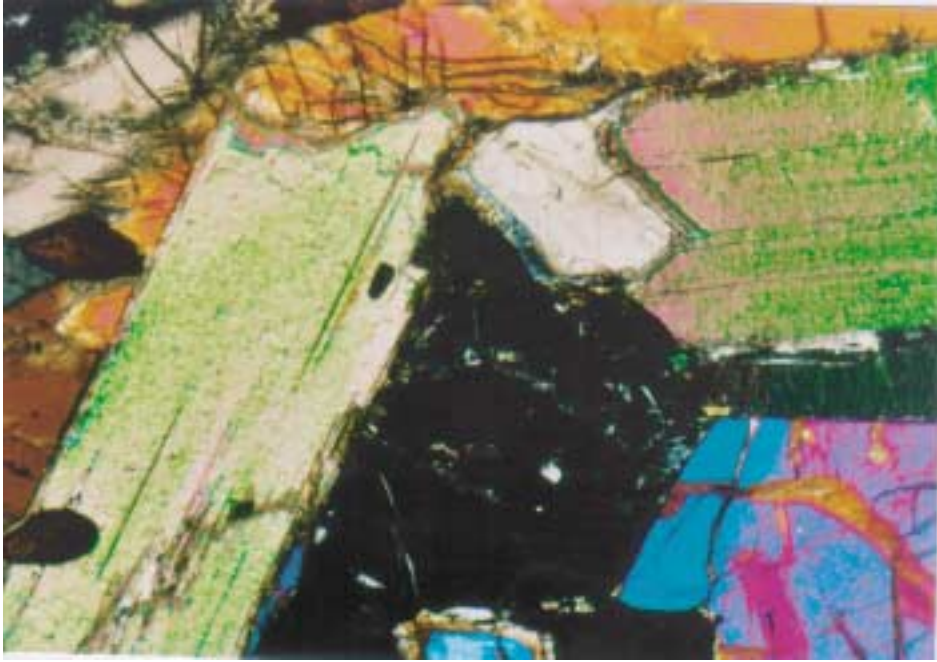
Figure 21: Photomicrograph showing the same as Figure 20 but in XPL
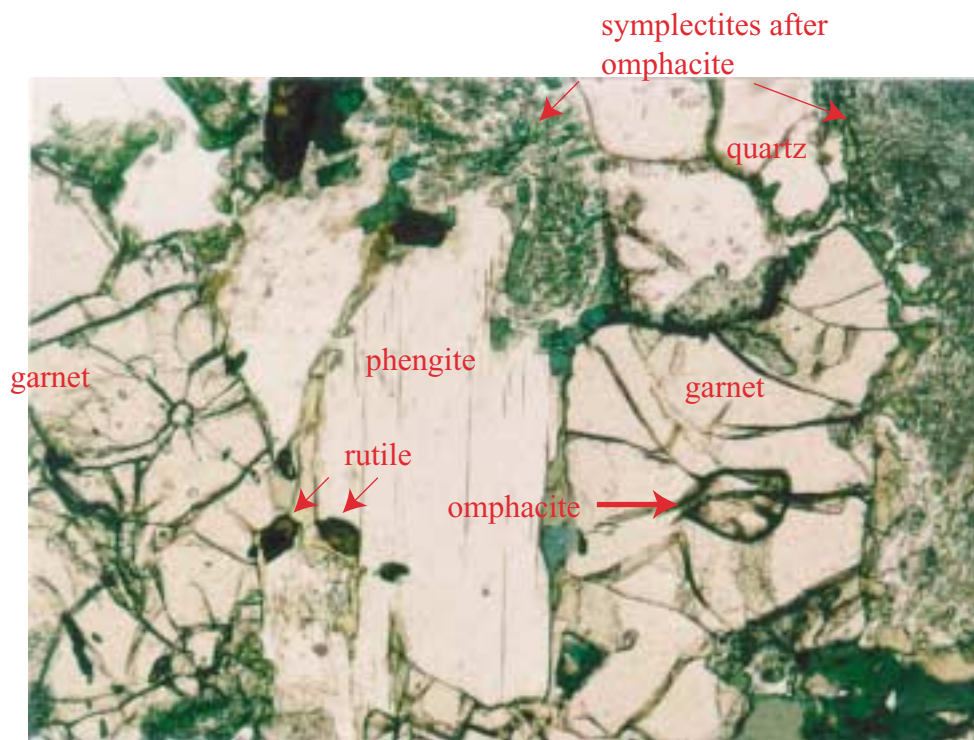

Figure 22: Photomicrograph showing a relict omphacite inclusion within garnet, beside a large phengite of the matrix. The matrix consists largely of symplectites formed after omphacite and minute amphibole porphyroblasts (greenish). Note that the garnet on the left contains a quartz inclusion with radial fractures. Gneissic eclogite sample Dab 9837. PPL, long side is 3.6 mm.
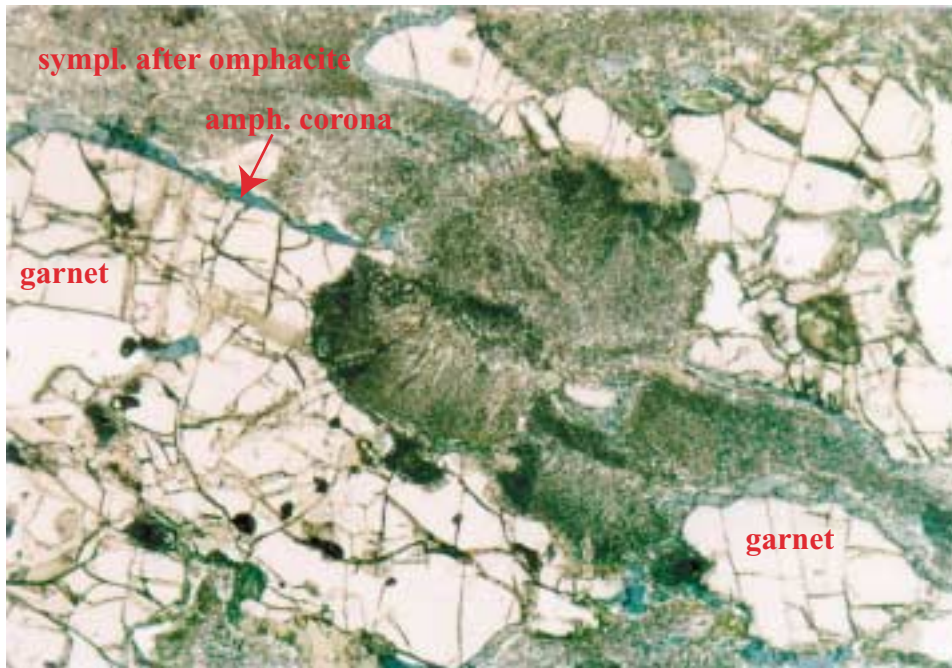
Figure 23: Photomicrograph showing symplectites after omphacite, and garnet in the matrix of gneissic eclogite Dab 9837. Note the amphibole coronas around garnet and the undeformed texture of the symplectites implying that no deformation occured after eclogite formation. PPL, long side is 3.6 mm.

Figure 24: Photomicrograph showing amphibole coronas around garnet and quartz, indicating that coesite/quartz was present in the matrix prior to amphibole growth. Gneissic eclogite sample Dab 99101, PPL, long side is 3.6 mm.
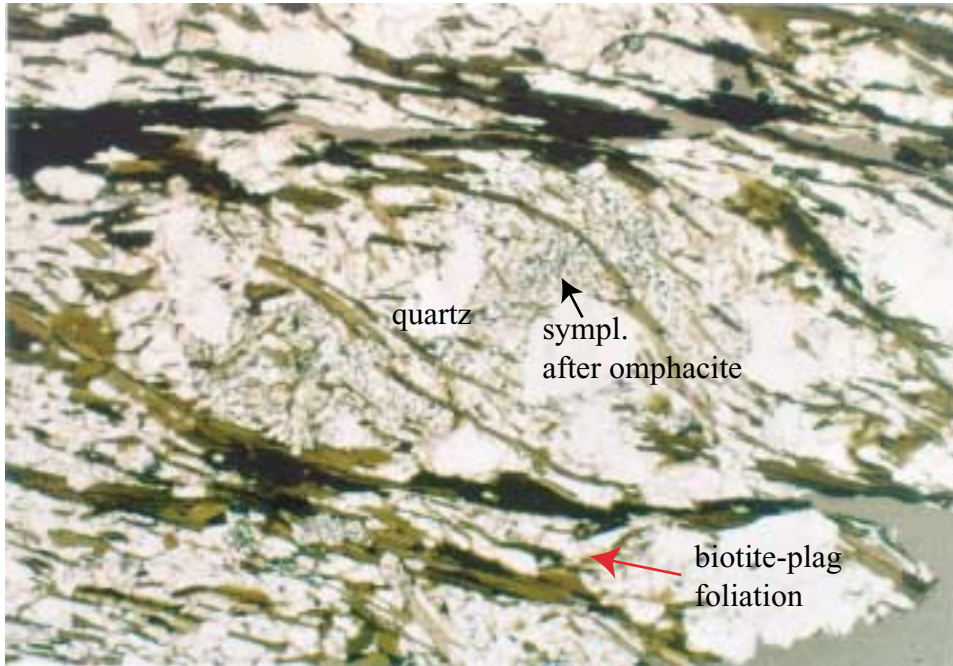
Figure 25: Photomicrograph showing a relict sigma-shaped portion of plagiclase and amphibole together with quatz wrapped in a biotite- Na-plagioclase foliation. Such a texture is indicative of replacing former omphacite grains (gneiss sample Dab 99104). See also text for discussion. PPL, long side is 8.6 mm.
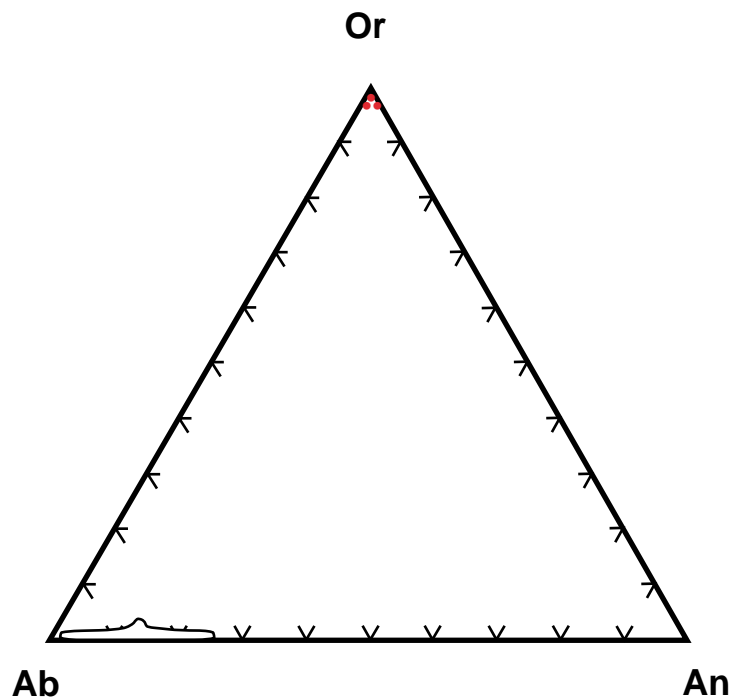
Figure 32: Ternary plot showing endmember compositions of feldspar from gneissic eclogite sample Dab (9837) - red dots - and gneiss samples (Dab 99103, 99104) -field at lower left.
Note that only Dab 9837 bears orthoclase and no plagioclase.

and porphyroblastic epidote. At the expense of the former phases, ab-rich plagioclase, epidote, biotite, titanite and in part calcite enter the paragenesis. A foliation is defined by aligned biotite flakes and granoblastic but shape-oriented plagioclase and quartz grains, which show undulous extinction. Epidote is mainly granoblastic, with quartz blebs included in its margins and generally overgrows the foliation, and in sample Dab 99103 rutile is still present. However, Dab 99104 preserves sigma-shaped structures, wrapped by a biotite foliation, where symplectites likely after omphacite are still recognisable (cf. Fig. 25).

Based on the above description the sample suite defines a continuous evolution from a UHP metamorphic stage to a greenschist-facies one.

4.1.2 MINERAL CHEMISTRY

Garnet

Compositions of all analysed garnet crystals from the basement rocks are plotted in terms their grossular, pyrope and almandine + spessartine endmembers (Fig. 26) in triangular diagrams. They clearly form two groups, both with a very narrow range: i) grains of the gabbroic eclogite sample Dab 99178 are richer in pyrope and grossular than ii) garnet from eclogite, gneissic eclogite and gneiss samples (Dab 99101, 99102 and 99103, respectively) which are almandine enriched. All garnets are very poor in Mn and Cr but they have Fe^{3+}-contents of ca. 2-8 % Fe_{tot} (determined by charge balance). Microprobe profiles indicate that a pronounced chemical zonation pattern is present at the grain margins whereas the cores show only weak zoning (cf. Figs. 27, 28). Rim compositions vary depending on the neighbouring phase. Garnet-garnet rims in the gabbroic eclogite (Dab 99178) show a strong increase in Fe_{tot} at the expense of pyrope and grossular components, in contrast a slight increase of Ca and Fe is present from core to rim which decrease again at contacts to omphacite (cf. Fig. 28). Garnet crystals from the other rock types (i.e. group ii)) record a similar but in part more complex style of zonation pattern from core to rim with an increase in Ca and Mg towards the outer parts which in turn decreases at grain rims. Garnet from the eclogite lens (Dab 99102) shows an especially complex pattern and a wider rim section where Ca and Mg decrease, while grains whereas the gneiss sample (Dab 99103) show a continuous decrease in Ca and Mg (cf. Fig. 27).
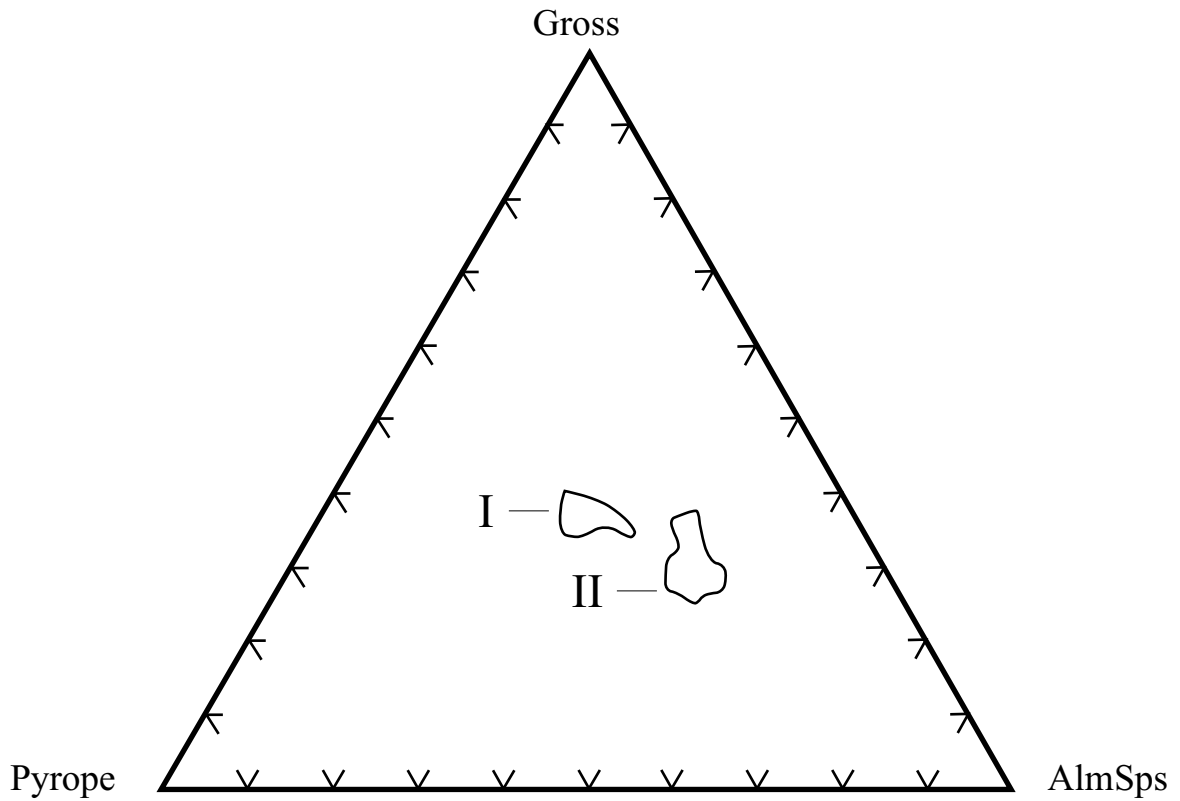
Figure 26: Ternary diagram showing fields of endmember compositions of garnet from all basement samples. I - analyses from gabbroic eclogite (Dab 99178); II - analyses from gneissic eclogite, eclogite lens and gneiss (Dab 99101, 99102, 99103, respectively). Gross - grossular, AlmSps - almandine + spessartine.
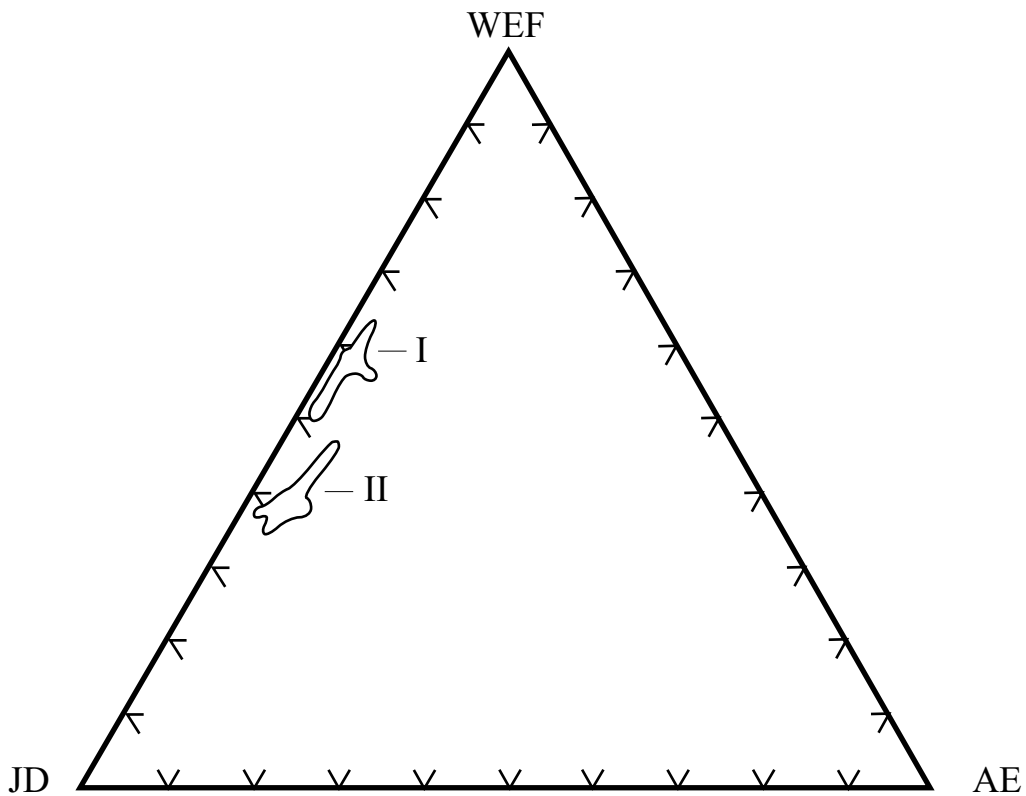
Figure 29:Ternary diagram showing fields of endmember compositions of clinopyroxene from two samples. I - analyses from gabbroic eclogite (Dab 99178); II - analyses from eclogite lens (Dab 99102). WEF - wollastonite+enstatite+ferrosilite; JD - jadeite; AE - aegerine
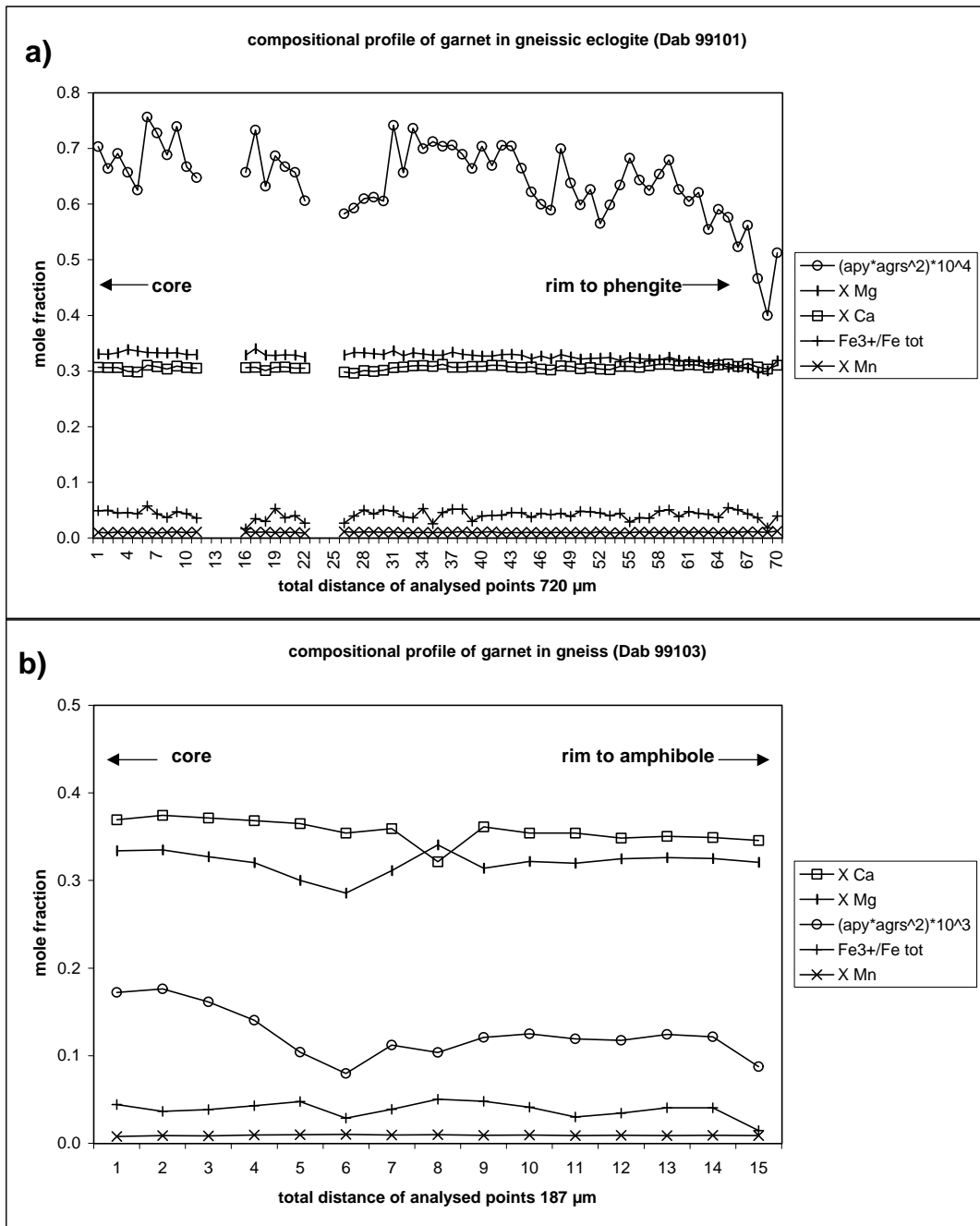
Figure 27: Chemical composition of garnet within a) gneissic eclogite and b) gneiss samples from the basement calculated from equally spaced microprobe profiles. Activities for pyrope and grossular are calculated after Newton and Haselton (1981) at 700 °C and are plotted - with an additional exaggerating factor - as used in the barometer of Waters and Martin (1993).

X Mg = Mg/(Mg+Fe2+); X Ca = Ca/(Mg+Ca+Mn+Fe2+); X Mn = Mn/(Mg+Ca+Mn+Fe2+); Fe 3+ contents are calculated using charge balance criteria.
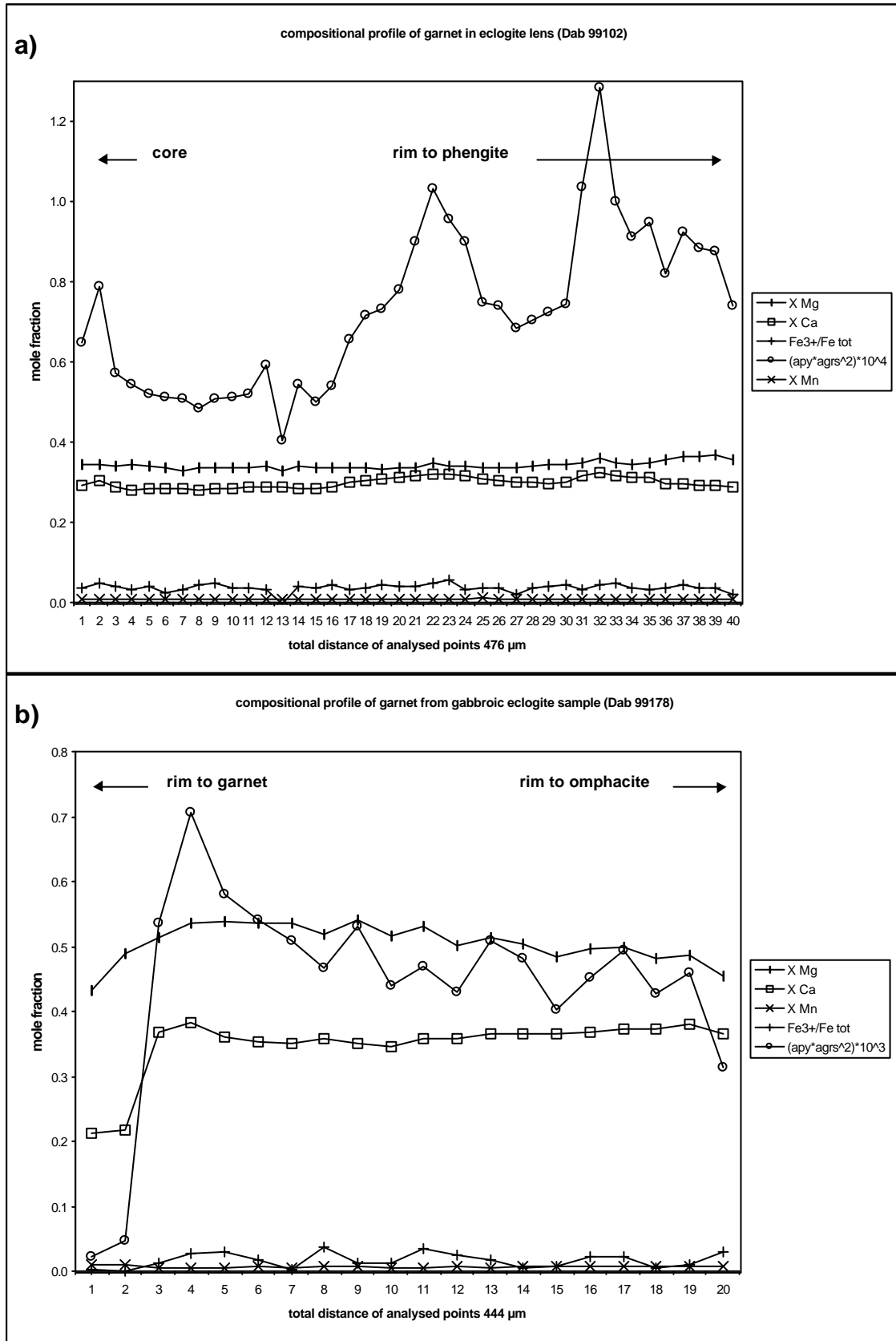
Figure 28: Chemical composition of garnet within a) eclogite lens and b) gabbroic eclogite samples from the basement calculated from equally spaced microprobe profiles. See Fig. 27 for explanation of the legend.

Clinopyroxene

Omphacite grains are present in only three of the analysed samples and are distinct in their jadeite content (cf. Fig. 29). Sample Dab 99178 (gabbroic eclogite) has a maximum of Jd_{50} whereas Dab 99102 (eclogite lens) has up to Jd_{63} and a single analysis of omphacite in Dab 9837 (gneissic eclogite) revealed $Jd_{67}WEF_{28}Ae_5$ (not plotted). Due to the low Fe_{tot}-contents of all the analysed omphacite, the Fe^{3+} was fixed at 50% (see above) but the aegirine component is not higher than about 8 mol%. Individual omphacite grains are quite homogeneous except at their rims and close to fractures. The gabbroic sample Dab 99178 shows omphacite with a clear decrease in X_{Na}, a slight decrease in X_{Mg} and an increase of Fe_{tot} at the rim, but grains from the eclogite lens (Dab 99102) lack a Na decrease and varies only slightly at contacts to garnet but strongly close to fractures (cf. Fig. 30a, b). Inclusions within garnet of the eclogite lens sample (Dab 99102) have the same composition as matrix grains (cf. Fig. 30c). The well preserved homogeneity in large parts of the grains indicates equilibration during the peak of metamorphism, whereas the rims reflect a retrogressive exchange with plagioclase-amphibole symplectite formation at some grain rims documenting omphacite consumption/breakdown in the presence of silica and a fluid phase.

Mica

White mica in the matrix of eclogitic and gneissic samples (Dab 99101, 99102 and 99103, respectively) is phengite with quite constant Si contents of about 3.4-3.5 p.f.u. and an X_{Mg} of about 0.9 in their central and outer parts. At grain rims a significant decrease in Si p.f.u. and an increase in Na is recognised (cf. Fig. 31a, b). The X_{Mg}–values do not perfectly correlate to this pattern, especially in the gneissic eclogite (Dab 99101) a slight increase in X_{Mg} at contacts to garnet was detected, whereas the eclogite lens (Dab 99102) records a decrease of X_{Mg} in this position. However, the central portions with high Si-content of phengite likely reflect equilibrium during a period of elevated pressures and thus should have formed at the peak of metamorphism. In the gneiss sample Dab 99104 only biotite was recognised, which is unzoned and shows a high X_{Mg} (Fig. 31c). Paragonite is confined to the gabbroic eclogite (Dab 99178) and is rather uniform in composition (Fig. 31d).
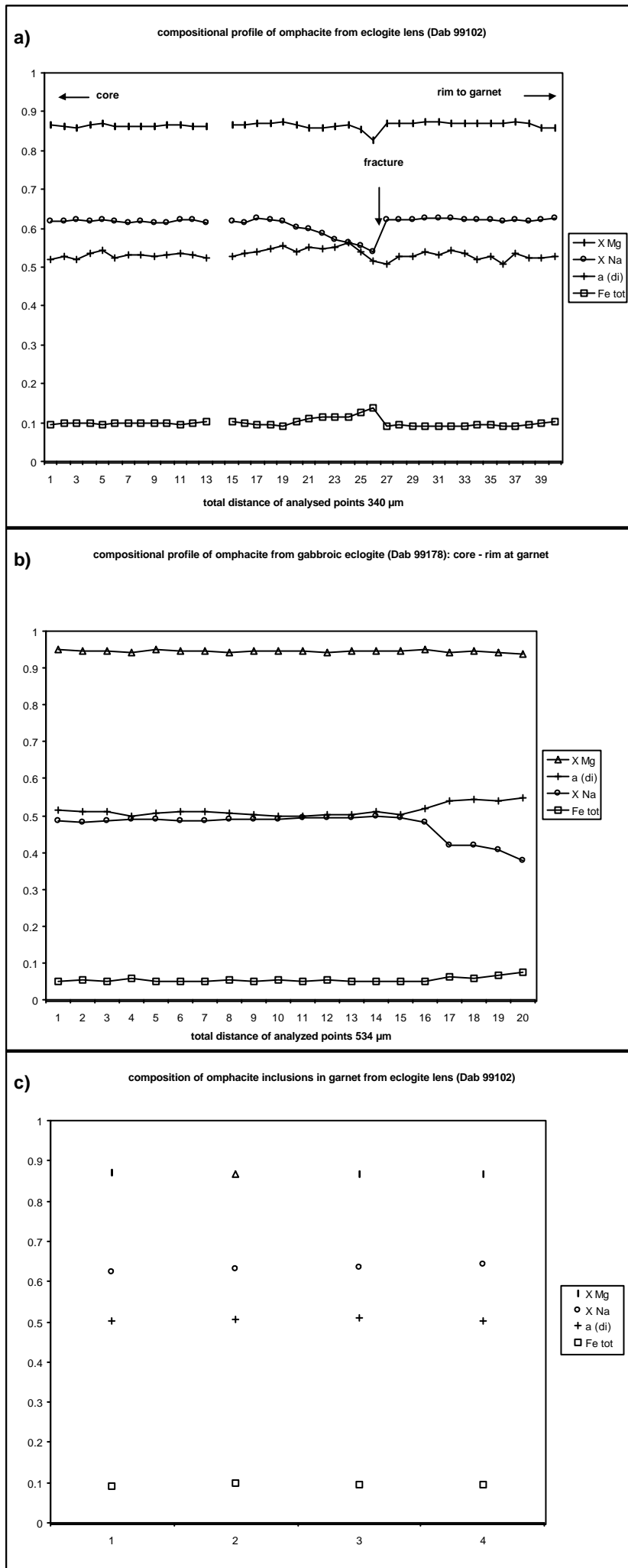
Figure 30: Chemical composition of omphacite within a) eclogite lens, b) gabbroic eclogite and c) garnet of eclogite lens. A) and b) are calculated from equally spaced microprobe profiles. Diopside activity is calculated after Holland (1990) at 700 °C. X Mg = Mg/(Mg+Fe2·. X Na = Na A / sum A. Note that the ferric iron content is fixed at 50 %, see also text for discussion.
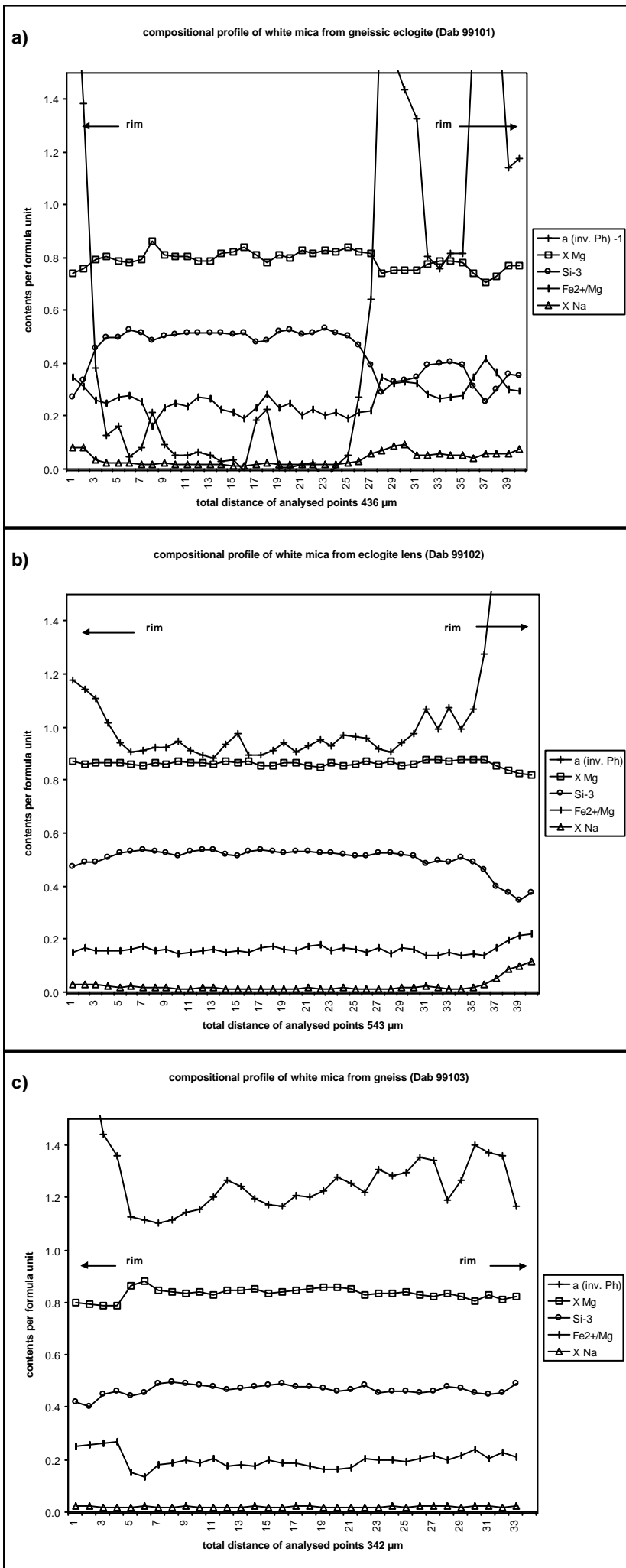
Figure 31 a, b, c: Chemical composition of phengite within a) gneissic eclogite, b) eclogite lens and c) gneiss samples from basement rocks calculated from equally spaced microprobe profiles. The activity is calculated as ideal (cf. chapter 4). Activity and Si contents per formula unit are manipulated to fit the diagram-scale. X Mg= Mg/(Mg+Fe2+); X Na = Na A / sum A. Note that the ferric iron content is fixed at 50 %, see also text for discussion.
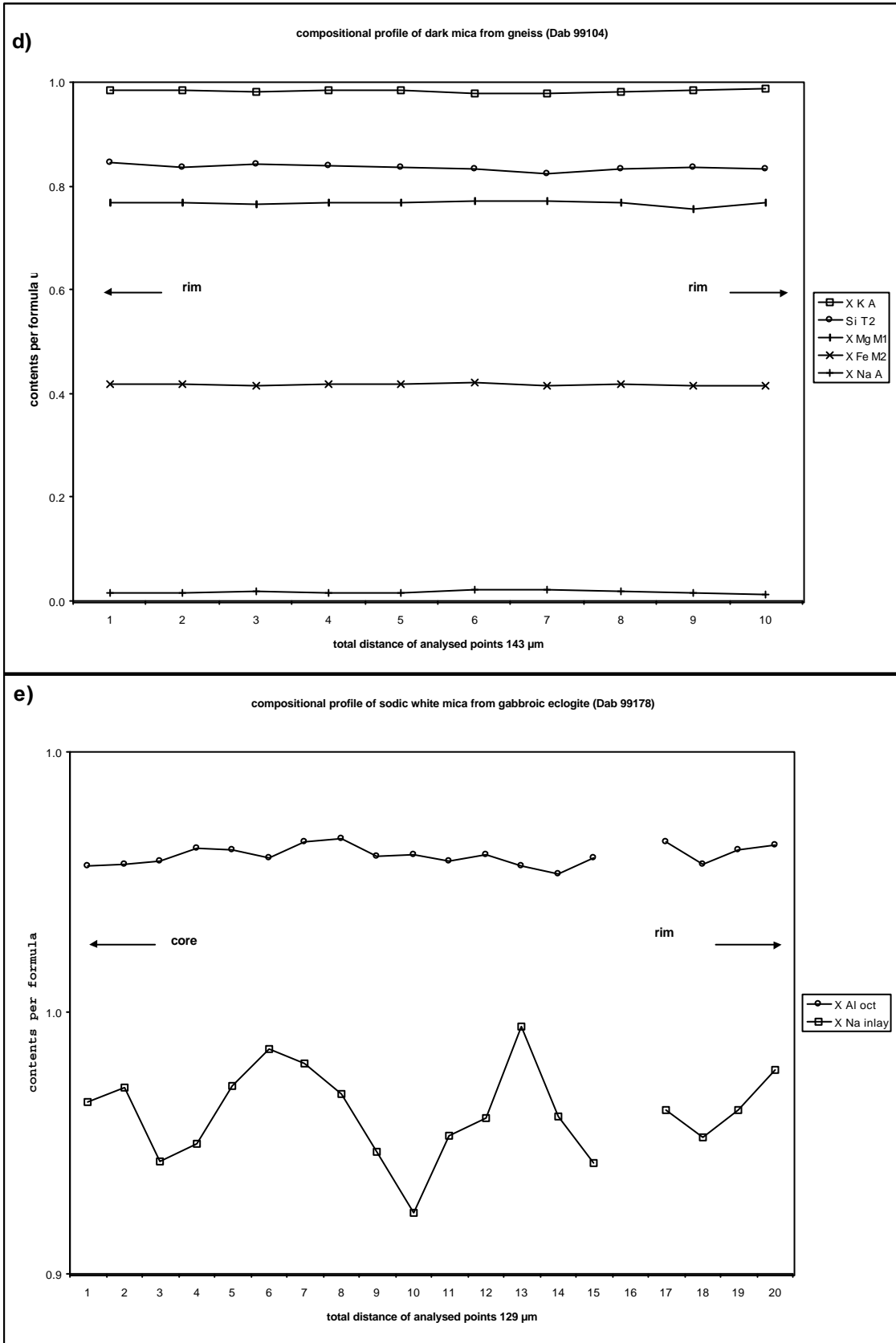
Figure 31 d, e: Chemical composition of mica in a) gneiss and b) gabbroic eclogite samples from the basement calculated from equally spaced microprobe profiles.

Amphibole

According to the classification of Leake et al. (1997) amphibole in Dab 99103 is pargasite and edenite, in 99104 magnesiohornblende occurs, whereas Dab 99178 bears barroisite. Amphibole in the symplectites likely formed after omphacite (Dab 99101) is also magnesiohornblende. Any textural control of amphibole composition was not checked in detail, mainly because most emphasise was placed on the P-T-x parameters during the peak of metamorphism.

Feldspar

Two different types of feldspar are recognised in the samples; orthoclase occurs as a matrix phase in Dab 9837, whereas matrix grains of plagioclase with ab_{75-90} are similar to plagioclase in symplectites next to amphibole (cf. Fig. 32).

4.1.3 THERMOBAROMETRY

Most emphasis is placed here on the determination of the absolute peak P-T conditions and/or, if accessible, maximum or minimum pressure constraints recorded by the samples, in order to document a common UHP overprint of the different lithologies. The rock and mineral textures described above already indicate that they shared a common eclogite-facies metamorphic event, although critical assemblages are not preserved in all samples. A representative set of mineral analyses is listed in Table A2.

P-T results

The calculated equilibria for the various applied thermobarometers are graphically shown for the mafic and gneissic rocks (Fig. 33). For all samples a clear UHP overprint within the coesite stability field can be documented. The pressure estimates for samples Dab 9837 (gneissic eclogite) and Dab 99102 (eclogite lens) are in especially good agreement (33-35 kbar at ca. 680° C), whereas for the coesite-bearing gabbroic sample Dab 99178 P-T conditions are estimated by the stability of kyanite; paragonite formation constrains the lower P-T limit for the eclogitic paragenesis (cf. Fig. 33). The estimated minimum pressures for the gneissic eclogite and gneiss (Dab 99101 and 99103, respectively) are also above the coesite-α quartz equilibrium (cf. Fig. 33).
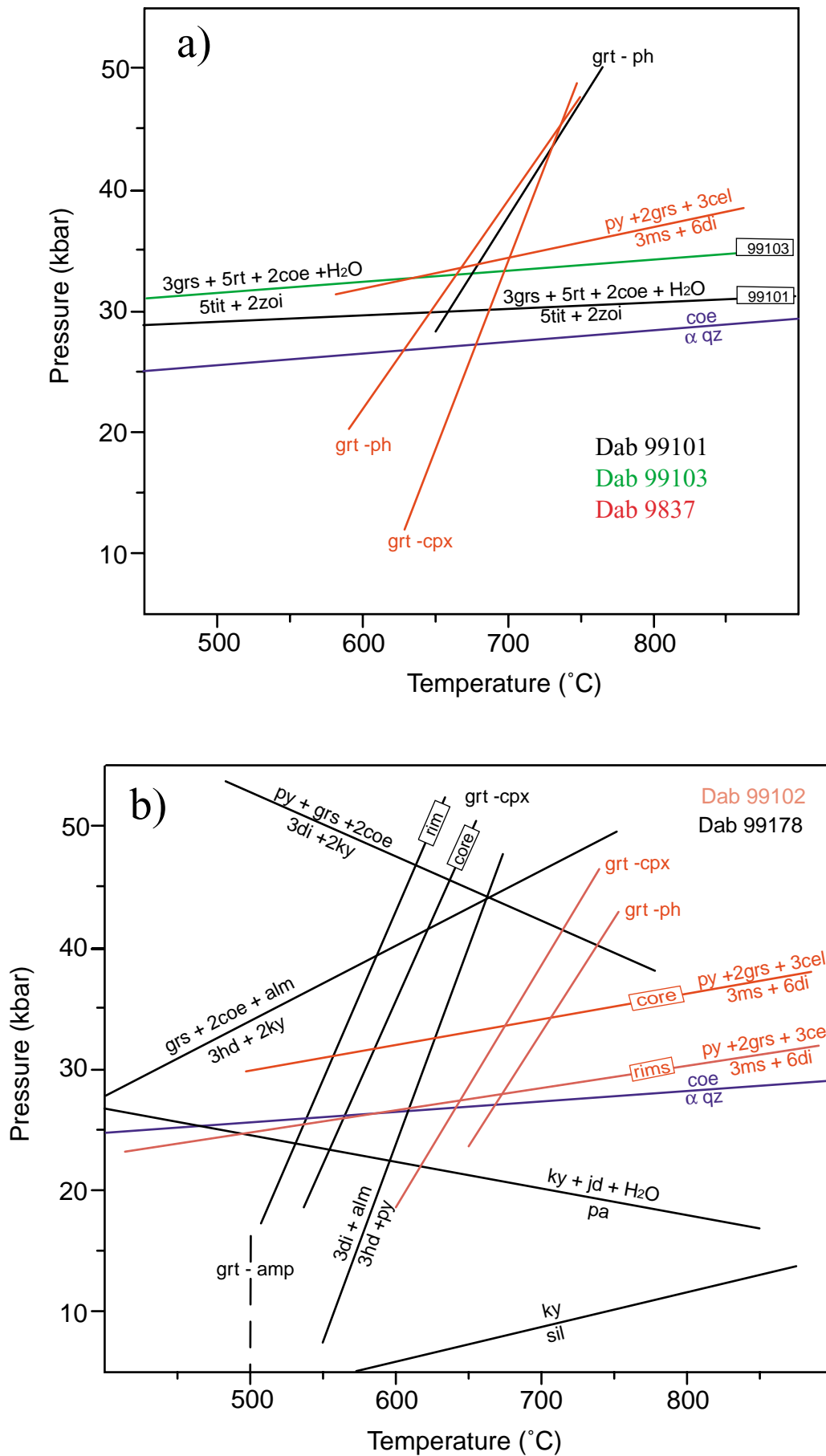
Figure 33: P-T plots for samples from the basement. a) gneissic eclogite samples Dab 9837 and Dab 99101, as well as for gneiss sample 99103; b) eclogite lens Dab 99102 and gabbroic eclogite Dab 99178. Note that all samples calculate UHP conditions. For sample Dab 99178 a discrepancy in temperature estimates is due to different handling of the ferric iron content in the applied method. See also text for a detailed discussion.

Temperature estimates are more variable, especially for garnet-clinopyroxene if using the TWQ program (Berman 1991) or the formulation of e.g. Powell (1985) for the gabbroic sample (Dab 99178). The difference can be explained by the fixed Fe^{3+} content in using Powell (1985) and the integrating procedure of the TWQ program, due to a lack of aegirine data. However, in this case the invariant point calculated with Berman (1991) and defined by the garnet, clinopyroxene, SiO_2 and kyanite equilibria puts more constraints on the reliability of results. It is further closer to the temperature estimates of the other samples (cf. chapters 5.2, 5.3), thus in this case the 50% Fe^{3+} is apparently an overestimate. However, the garnet-phengite and garnet-clinopyroxene temperatures for the rest of the sample suite are in good agreement for the given errors of the calibrations (cf. Fig. 33).

Calculation of P-T conditions using the rim compositions of the minerals only yielded reasonable result for the eclogite lens (Dab 99102) pointing to decreasing pressure (ca. 28 kbar at 650° C). The temperature calculations are somewhat ambiguous because the K_D among garnet-clinopyroxene and garnet-phengite is not changing very much, although the composition is modified. Thus it is questionable if the rim compositions are solely due to the Fe-Mg exchange reactions but reflect a change (due to fluid influx?) in the effective bulk composition participating in the reactions.

Nevertheless, the P-T estimates document a common UHP overprint for all the basement rocks studied here and are in fair agreement with the results of Carswell et al. (2000) for similar (but non-eclogitic) rocks.

4.2 PETROLOGY OF THE CHANGPU UNIT

4.2.1 PETROGRAPHY

Eclogite-facies rocks from the Changpu Unit were preferentially sampled from outcrops and localities where they occur within and/or together with calc-silicate rocks in order to provide petrologic evidence of their postulated common genesis. The samples are subdivided into phengite-eclogites, carbonate-eclogites and calc-silicate rocks; the different rock-types with their observed mineral assemblages are listed in Tables A3. This distinction is somewhat arbitrary because sharp boundaries between carbonatic and basic rocks are sometimes lacking, thus the
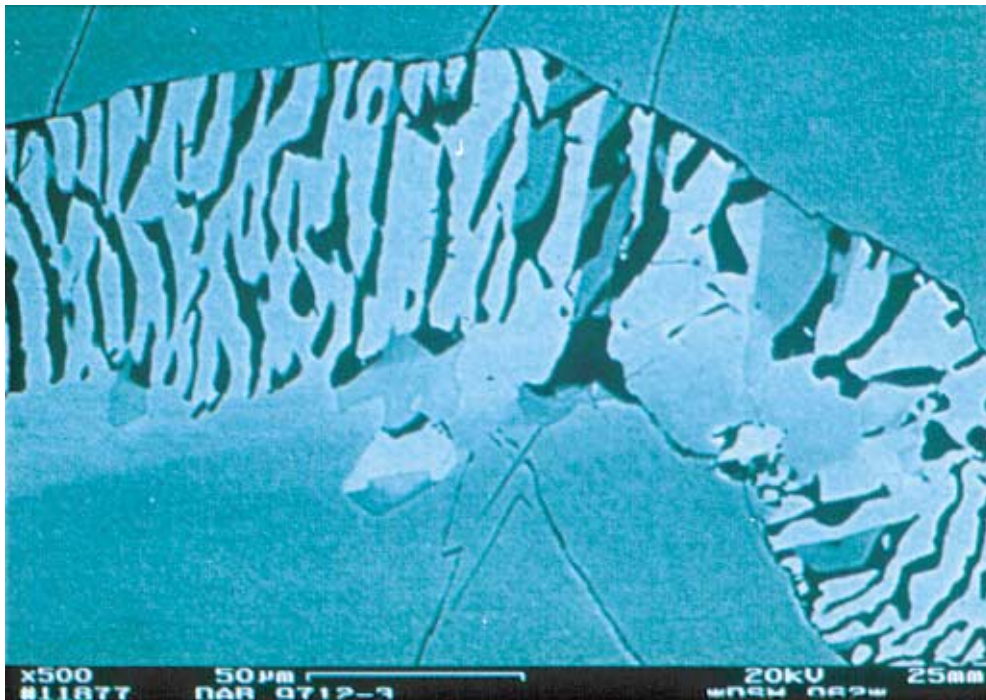
Figure 34a: Back-scatter-electron image showing symplectites of albite (black) and clinopyroxene (white) together with amphibole (grey) developed between two adjacent omphacite grains. Note the slight zoning present in lower omphacite grain close to symplectite. Fractures in omphacite do not penetrate the symplectite, thus they are older.
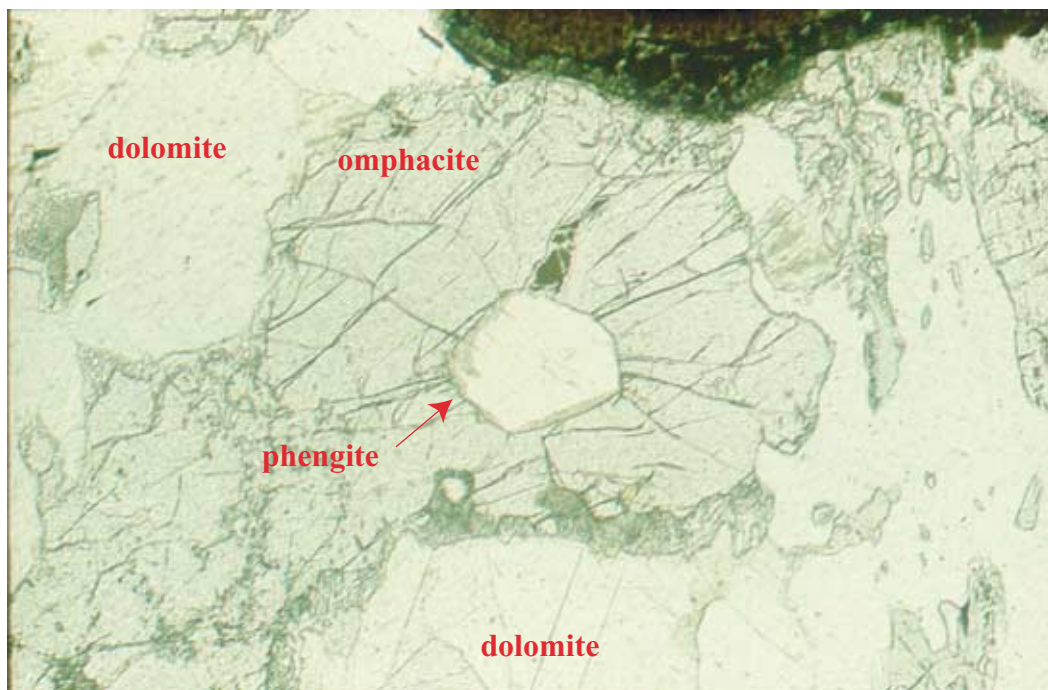
Figure 34b: Photomicrograph showing a phengite inclusion within omphacite of calc-silicate sample Dab 9712. Note the radial fractures developed around phengite, which has about 3.7 Si a.p.f.u. (cf. Fig. 44). Omphacite and phengite have symplectites developed at their grain rims. PPL, long side is 0.88 mm.

rock types are classified and described based on their textures in thin-section.

Eclogite

Phengite-eclogites are often well preserved and are dominated by garnet and variable amounts of omphacite, phengite, rutile, ± coesite and, in case of samples Dab 9719 and 9857, additional zoisite and kyanite, respectively.

Carbonate-eclogites are often more retrogressed than the former type and are characterised not only by less abundant garnet but also by additional carbonate in the matrix and inclusions in garnet and omphacite. Both types of eclogite show relict coesite inclusions or textures indicative of quartz-pseudomorphs after coesite in garnet and omphacite (e.g. samples Dab 9854, 98409). Furthermore, common textures indicative of breakdown of omphacite + SiO_2 to symplectites of clinopyroxene/amphibole and An-poor plagioclase (cf. Fig. 34a) as well as quartz-grains in the matrix of undeformed samples imply the former stability of coesite as a matrix phase during UHP conditions. The major eclogitic phases often display granoblastic textures with straight grain boundaries, but some samples show a preferred orientation with the alignment of elongated garnet, omphacite and zoisite (Dab 9719). Phengite and rutile commonly form inclusions in garnet, omphacite and kyanite. Notably, garnet and omphacite reveal an intense fracturing, which terminates at contacts with retrograde phases. Around inclusions and matrix grains of phengite spectacular sets of radial fractures are developed in host and neighbouring grains of garnet and omphacite (Fig. 34b). Because all these fractures terminate at contacts to non-eclogitic minerals, they predate any retrogressive mineral growth and are interpreted as an expression of volume increase due to pressure release and differences in elastic properties of host grain and inclusion during the initial exhumation of the rocks.

Calc-silicate rocks

Calc-silicate rocks, whether or not hosting eclogites, show a broader variation in texture and metamorphic grade. Whereas virtually pristine UHP mineral assemblages are dominant in many samples, others experienced a complete retrogression under amphibolite- to greenschist-facies conditions. At thin-section scale, calc-silicates are distinguished from eclogites by a lack of garnet. Pristine calc-silicates mainly consist of calcite or dolomite with additional omphacite, phengite and rutile; rare coesite inclusions or quartz aggregates after coesite appear in omphacite
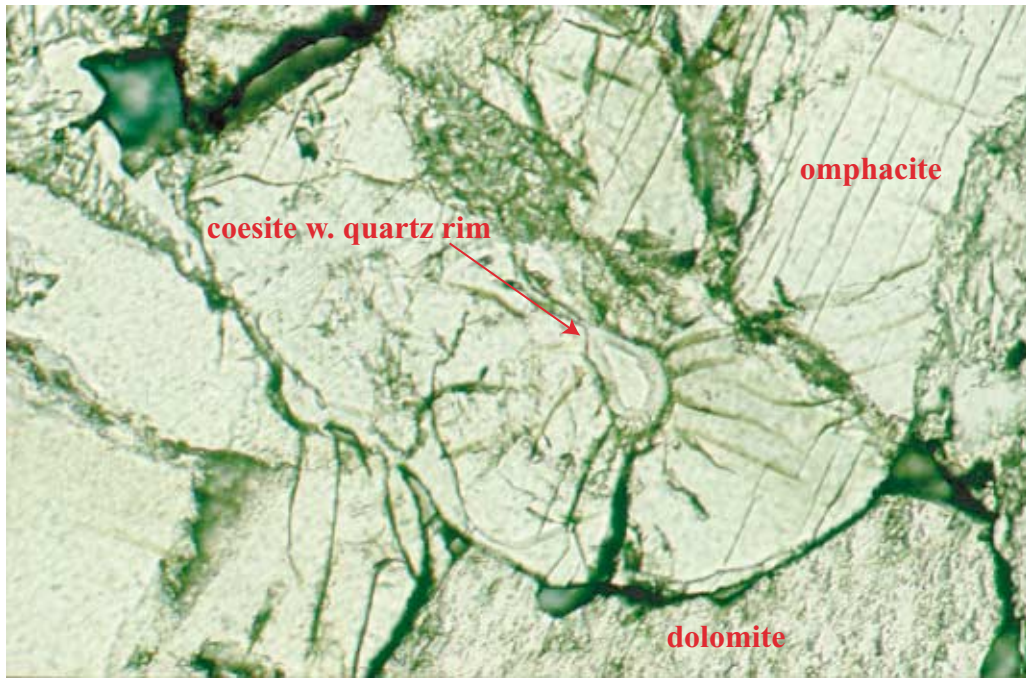
Figure 35a: Photomicrograph showing an inclusion of relict coesite rimmed by quartz within an omphacite grain of calc-silicate sample Dab 9712. Note the typical radial fractures around the inclusion. Figure 35b gives the Raman probe spectra of quartz and coesite. PPL, long side is 1.8 mm.
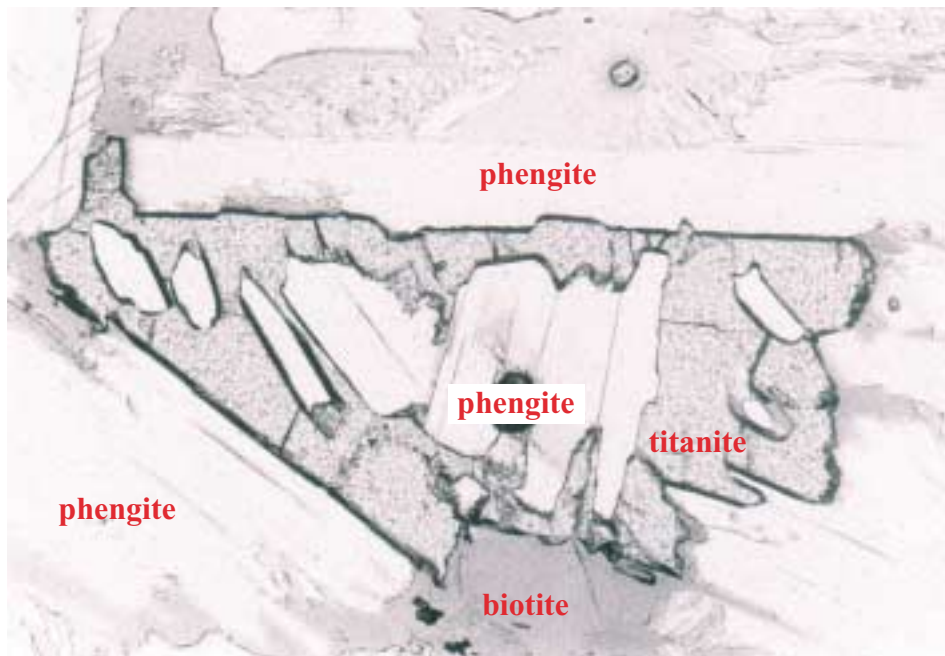
Figure 36 : Phengite inclusions within hyp-idioblastic titanite of calc-silicate sample Dab 9712. Thermo-barometry with phengite inclusions reveals decreasing P-T conditions following the peak of eclogite-facies metamorphism, further supported by the calculated titanite-reaction-equilibrium (cf. Figure 45). PPL, long side is 2.34 mm.
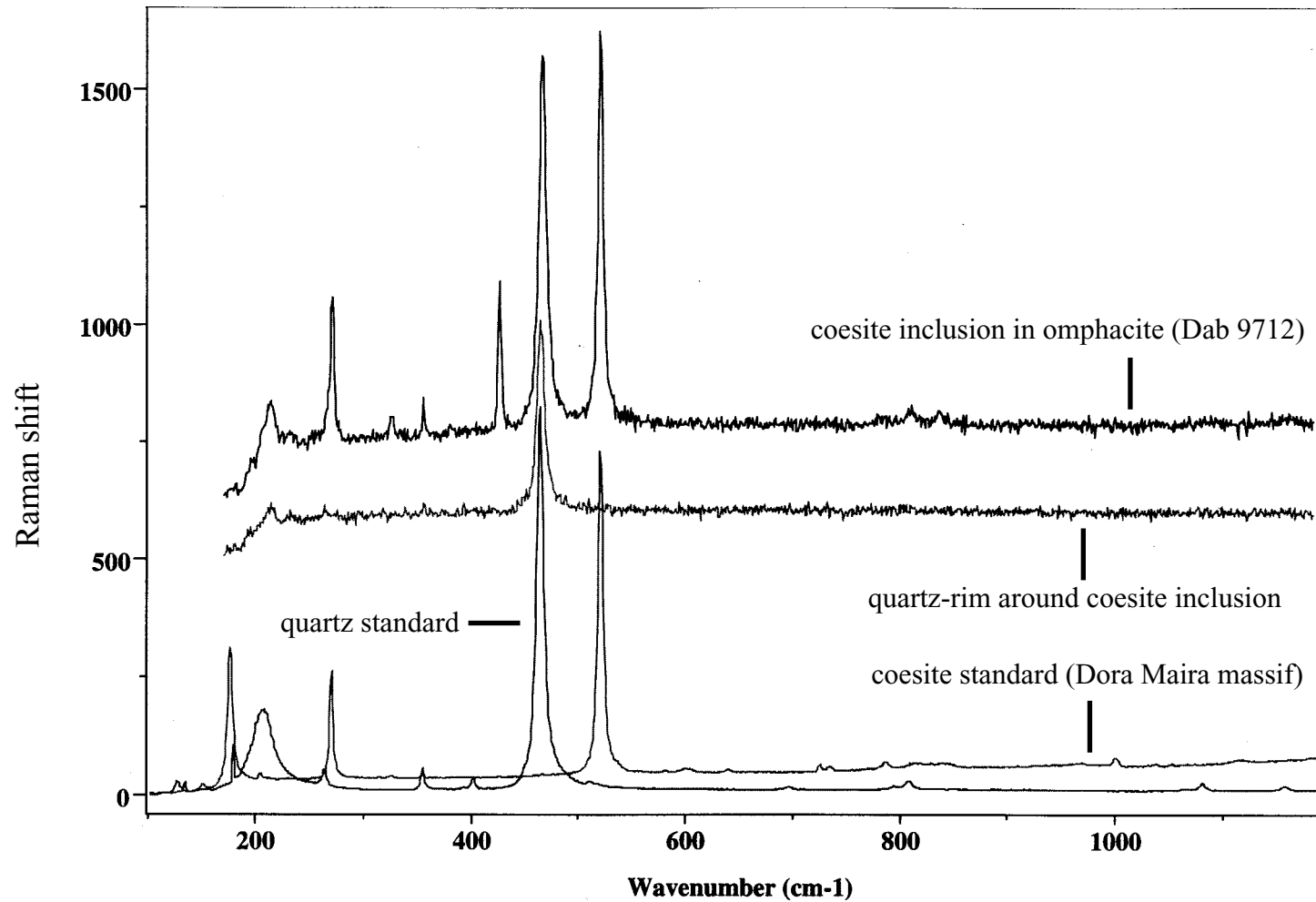
Figure 35b: Raman spectra of coesite inclusion in omphacite (Dab 9712), quartz-rim around the inclusion and of two standards. Note that the spectrum of the coesite inclusion includes also the main peak of quartz which is lacking in the standard. Note that coesite and quartz spectra from the sample have been shifted upward to avoid overlap with the standards, which are shown with their true Raman shift. Coesite and quartz standards are from the Raman laboratory of the ETH Z rich.

(cf. Fig. 35). In one sample phengite forms inclusions in omphacite and titanite (Dab 9712, cf. Figure 36). Carbonate has often a granoblastic shape but some grains show dynamic recrystallisation with the formation of small neoblasts at their margins. Omphacite and phengite are more or less aligned in the foliation but are randomly oriented in some specimen. Whereas omphacite shows only minor marginal replacement by symplectites, most of the former phengite has completely broken down to aggregates of biotite and plagioclase.

Retrograde hydrous minerals, replacing the pre-existing assemblages in different quantities, include coronitic amphibole, biotite, epidote-group minerals, titanite and rare chlorite, and occasionally display an alignment with the formation of a foliation. This shows that tectonic activity prevailed during exhumation, creating foliated amphibolite- and greenschist-facies fabrics. At thin-section scale it is often possible to clearly differentiate between preserved eclogitic and later retrogressive domains, which indicates localised access of fluids and/or deformation, promoting mineral reactions.

4.2.2 MINERAL CHEMISTRY

14 rocks were selected for microprobe analysis in order to sample the different mineral assemblages and metamorphic grades, but most attention was addressed to the composition of peak metamorphic phases. Therefore, a large number of measurements were performed on garnet, omphacite and phengite to identify potential peak and retrogressive compositions. The set of mineral analyses used in thermobarometric calculations and plots (cf. Table A5; Figs. 45, 46) is listed in Table A4. For reasons outlined above, the content of Fe^{3+}/Fe_{tot} used in all calculations and plots involving omphacite and phengite was fixed to 50%, while ferric iron in garnet was determined by charge balance methods.

Garnet

Garnet, as the most abundant mineral in the eclogites, varies greatly in endmember composition among the individual samples, thus six groups can be distinguished and are plotted in Figure 37a. The wide scatter is caused by highly variable contents of pyrope, almandine and grossular, whereas Mn-, Fe^{3+}-, and Cr-bearing endmembers are generally below 1 mole-%. Group I garnet, which is the richest and most variable in Ca, is present in small eclogite lenses (i.e.
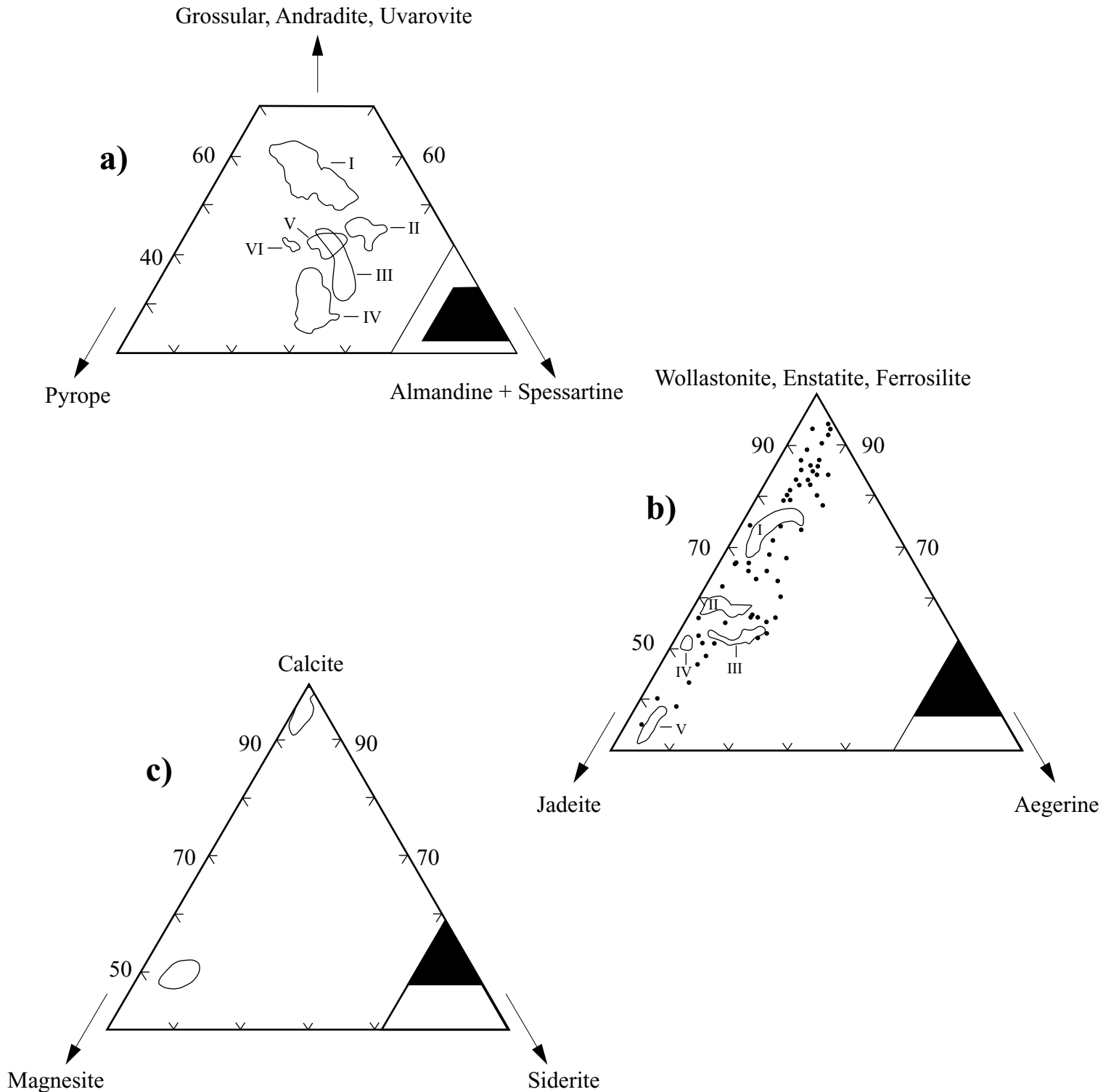
Figure 37: Ternary plots giving fields of endmember compositions for a) garnet, b) clinopyroxene, c) carbonate of all samples from the Changpu Unit. Roman numbers in a) and b) refer to groups of samples as discussed in the text. Note the small triangles in the lower right for plotted area of the larger one.

compositional profile of garnet (Dab 9712): rim at calcite-rim at epidote

(a)

total distance of analysed points 945 μm

compositional profile of garnet (Dab 9712): rim at phengite-core region

(b)

omphacite inclusion

total distance of analysed points 1750 μm

compositional profile of garnet (Dab 9854): rim at amphibole-rim at amphibole

(c)

coesite/quartz inclusion

total distance of analysed points 1900 μm

Fig. 38: Microprobe profiles for garnet from two samples from the Changpu Unit (Dab 9712 and 9854). Note the distinct zonation pattern and the respective behaviour of the plotted activity values (after Waters and Martin 1993, Newton and Haselton 1981).
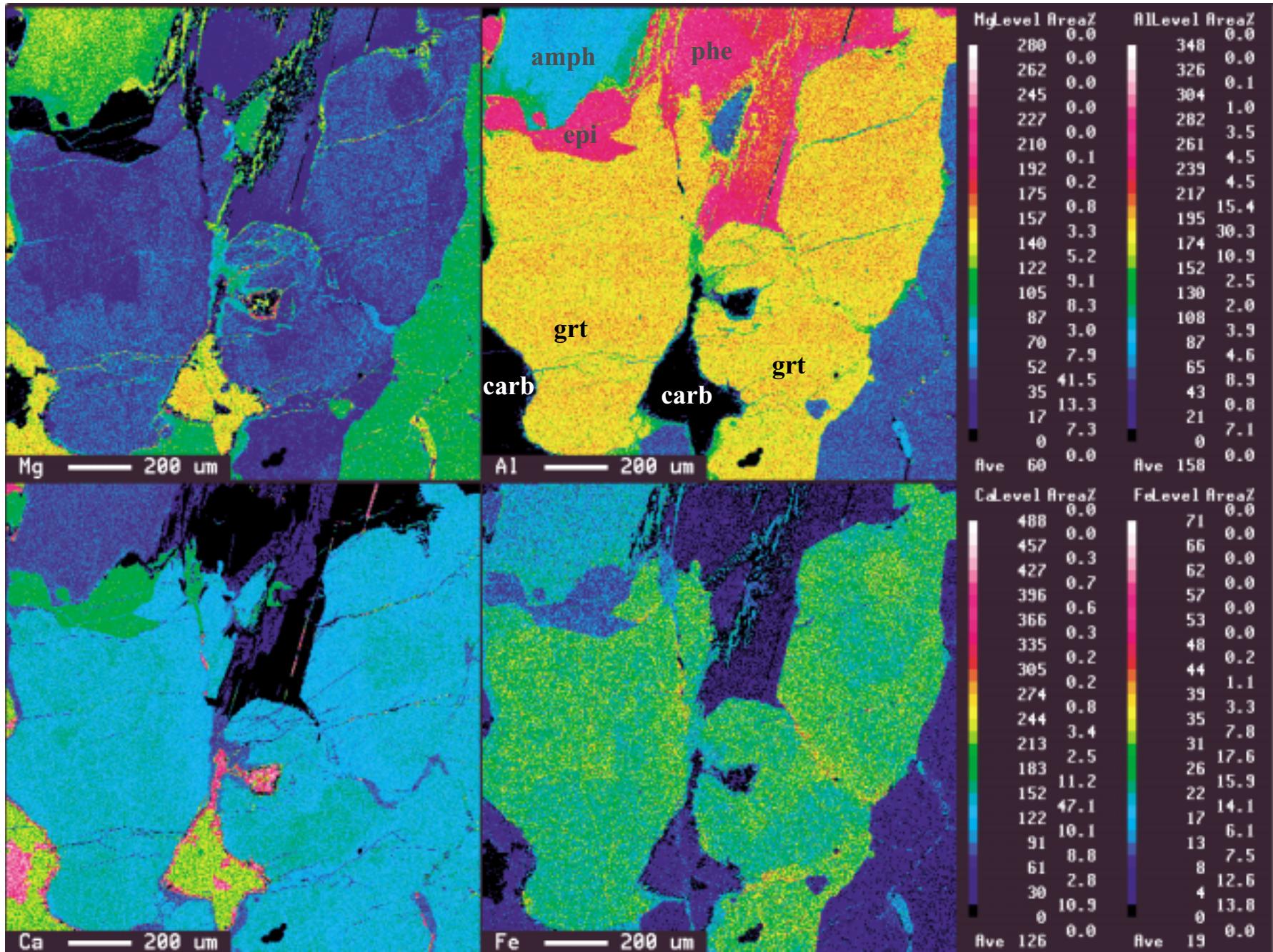
Figure 39: X-ray map of garnet from eclogite Dab 9712 for the elements Mg, Al, Ca and Fe. Note the distinct zonation in core and rim, cf. Fig. 38.

samples 9712, 9867, 98411, 98409 from locality 1; 98335, 9857 from localities 4 and 5, respectively; cf. Fig. 8). Group II, V and VI are richer in almandine and partly also in pyrope and show a smaller spread in endmembers. Considerably richer and more variable in almandine with higher pyrope contents are the groups III and IV. Garnet in part exhibits pronounced compositional zonation patterns (cf. Fig. 38). Spatial differences in chemical composition among garnet crystals in the same sample are depending on their grain size and the neighbouring phase. For example, large garnet porphyroblasts from a cm-sized eclogite lens surrounded by a calc-silicate matrix (Dab 9712) exhibit a flat compositional profile low in almandine but high in pyrope and grossular in the centre, and with distinctly higher X_{Fe}-values and lower Mg- and Ca-contents recorded in the rim section (Figs. 38, 39). A particularly strong increase in X_{Fe} at the expense of Mg (and in part of Ca) is recognised close to neighbouring Fe-Mg-silicates like phengite, omphacite and amphibole whereas this pattern is partly inverted at contacts to epidote and calcite. At rims of neighbouring garnet grains irregular zoning pattern are present, with an increase of X_{Fe} and a decreasing X_{Mg}, thus along grain boundaries a significant amount of exchange took place, likely promoted by a fluid phase (cf. Fig 40).

In principal all large garnet porphyroblasts show these core-rim relations, whereas such characteristic zonation patterns are by far less pronounced or absent in smaller garnet grains, which roughly approach the composition of the rim sections of the porphyroblasts.

Remarkably, one garnet porphyroblast (sample 9854) shows increasing Mg- and Ca-contents towards the rim and also towards inclusions of coesite/quartz in the centre of the grain (see Figs. 38c, 41). This increase towards the outer section and towards the inclusions may be due to equilibration processes in the course of the garnet growth. Smaller garnet grains of the same sample lack this zonation pattern showing a homogeneous composition corresponding to the outer sections of the garnet porphyroblasts with the highest X_{Mg}-values.

Compositional variations in the garnet porphyroblasts with the flat zoning profiles in the centre (Fig. 38a, b) are interpreted to be diffusion driven. The inner regions with the highest Mg and Ca contents likely reflect the temperature peak of metamorphism (see also thermobarometric calculations below), whereas the almandine-rich rims are assigned to have developed during retrogression and are also diffusion driven. In contrast, the garnet with the increasing Mg- and Ca-contents from core to rim shows prograde growth zoning with superimposed retrograde features at the rim section (cf. Fig. 38c).
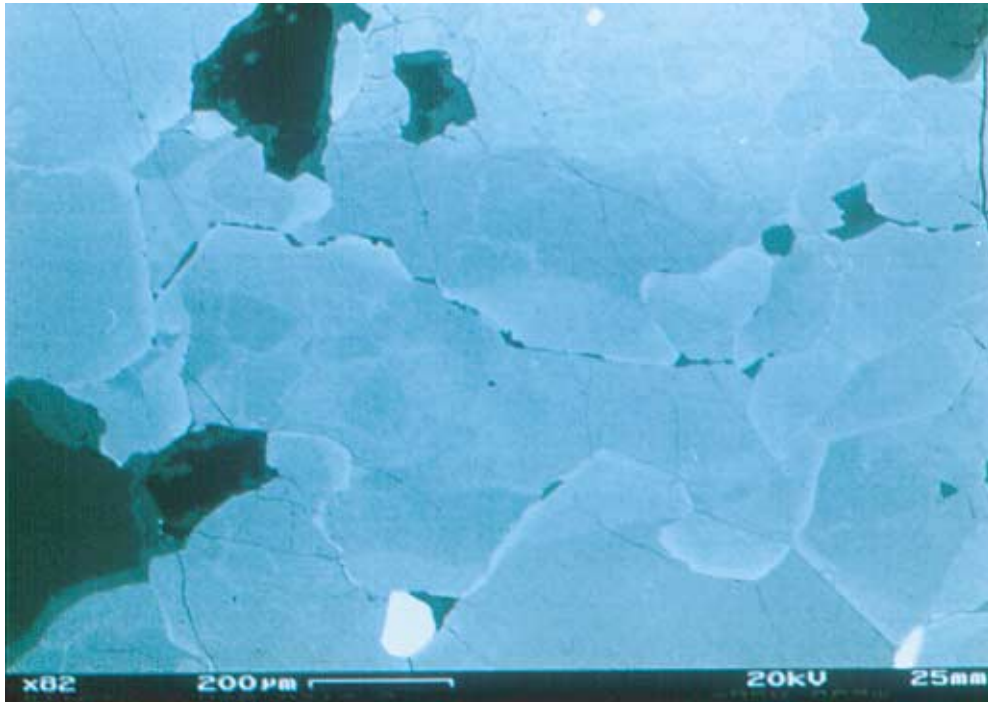
Figure 40: Back-scatter electron image showing garnet grains (bright) and dolomite (black) with calcite-corona (grey) from eclogite lens Dab 9712. Note the irregular zoning present in garnet as indicated by brightness variations. See Figure 38a and 39 for a typical compositional patterns of such grains.
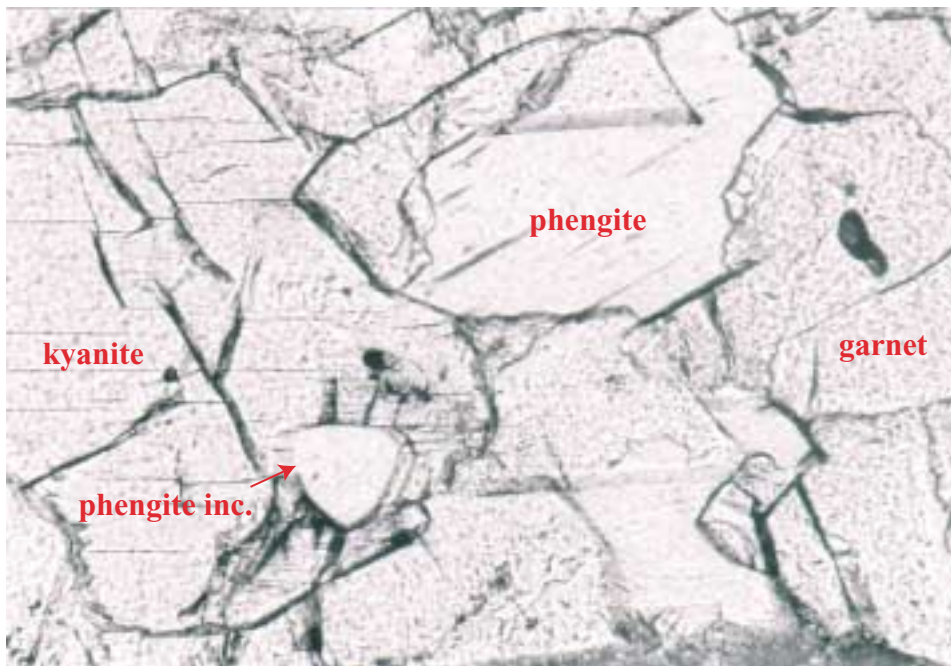
Figure 43a: Phengite inclusion within kyanite beside matrix phengite and garnet. Kyanite stability together with garnet and omphacite give additionally constraint to P-T conditions recorded in this sample (Dab 9857), see Figure 46a for other P-T estimates. PPL, long side is 0.88 mm.
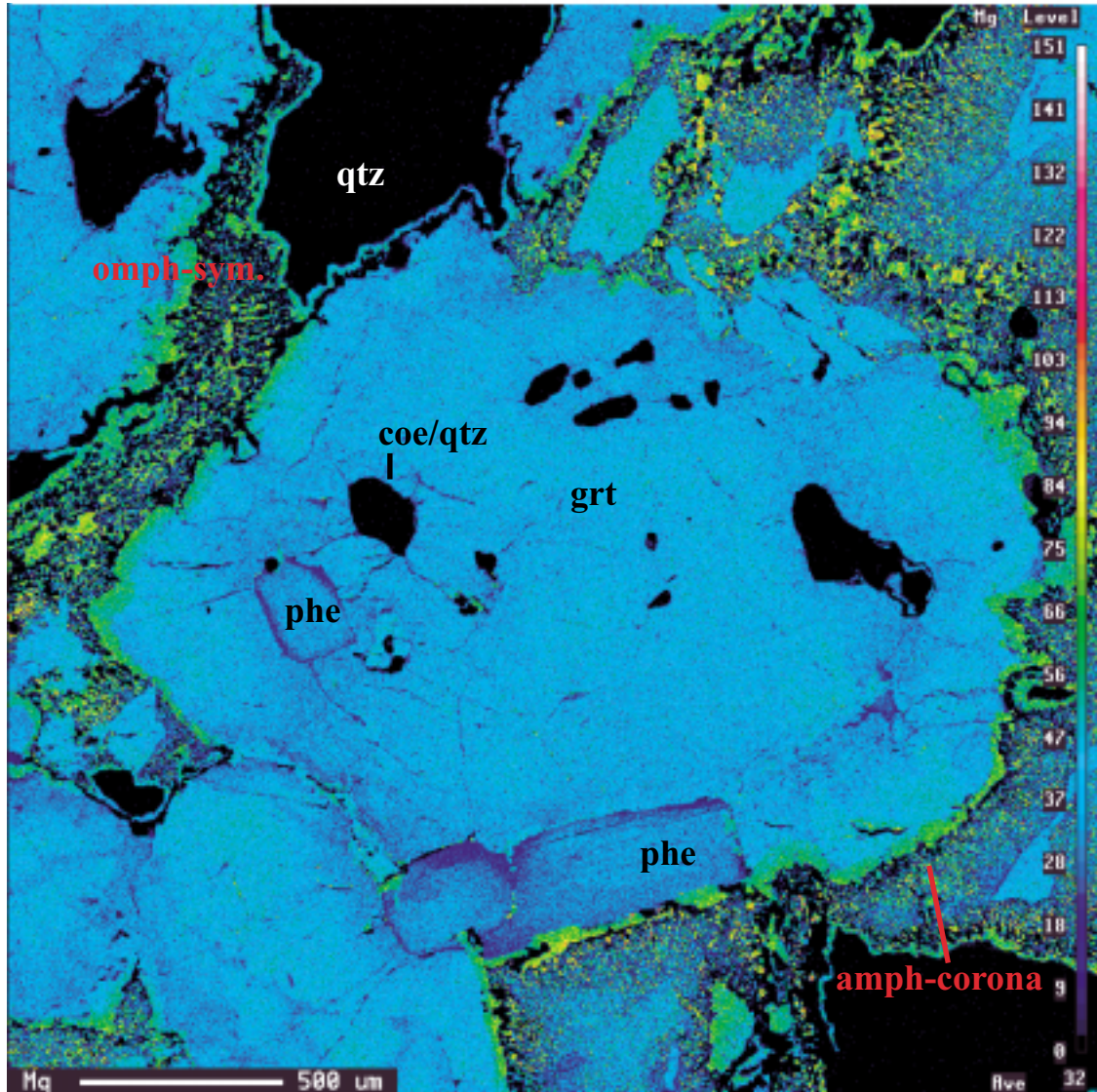
Figure 41: X-ray map for Mg of a large garnet with an amphibole corona (amph) and inclusions of
phengite (phe), coesite/quartz (coe/qtz) in eclogite sample Dab 9854. Note the distinct contents
in core and rim, especially at contact to phengite inclusions (cf. EMP profile of the same grain (Fig. 38c)).

Clinopyroxene

Two types of clinopyroxene occur in the samples. Omphacite is part of the eclogite facies mineral assemblages, whereas diopside-rich clinopyroxene is present in symplectites together with plagioclase or amphibole. In samples with strong retrogression, omphacite may be completely absent (cf. Table A3). Based on the classification of Morimoto (1988), six groups of clinopyroxene can be distinguished with a maximum aegirine content (Fe^{3+}/Fe_{tot} fixed at 50%) for all grains of less than 15 mole-% (Figure 37b): i) omphacite low in jadeite (Jd_{20-33}) occurs in samples 9712, 98411 and 98408; ii), iii) and iv) are omphacite with Jd_{33-47} but distinct diopside and aegirine contents (cf. samples 9718, 98382; 9719, 9872; 98335, respectively); v) grains with Jd_{57-65} were recognised in samples 9854, 9857 and 98133; finally, vi) clinopyroxene within symplectites of all samples show a strong variation towards higher $Ca-Mg-Fe^{2+}$ and lower Jd contents. In contrast to most garnet porphyroblasts, omphacite of all samples exhibit, if any, only a very weak compositional zoning for large parts of the individual grains (cf. Figure 42a). Prominent chemical changes mainly occur at grain rims and fractures. However, in some eclogite samples (e.g. 9718) omphacite was recognised to attain slightly lower X_{Mg}-values towards their rims (0.87-0.85), whereas others are virtually homogeneous. In contact to symplectitic intergrowths of albite-rich plagioclase ($Ab_{>80}$) and diopside or amphibole as well as near the contact to garnet, omphacite reveals a decrease in Jd and X_{Fe} at the expense of Mg at its rim.

Phengite

All investigated eclogite and calc-silicate samples are phengite-bearing. Phengite occupies various textural positions, which coincide with distinct compositional features. Phengite in eclogite occurs as a matrix phase as well as included in, and in contact to, garnet and kyanite (Dab 9857; Fig. 43). In the case of eclogite lens Dab 9712, phengite additionally occurs near the contact to the surrounding calc-silicates. In calc-silicate rocks, matrix phengite and phengite inclusions in omphacite and titanite were recognised (Dab 9712; Figs. 34b, 36, respectively). The variability of the Si content per formula unit (p.f.u.) and other cations of phengite in texturally different positions is best documented in sample Dab 9712 (cf. Figs. 42c, 44). Matrix phengite and phengite in contact to garnet in all eclogites reveal Si contents of 3.71-3.15 p.f.u., which is similar to the Si contents of the phengite inclusions in garnet (i.e. 3.69-3.15 Si p.f.u.). Phengite inclusions in kyanite yield Si contents of about 3.50 p.f.u. In calc-silicates, phengite included in
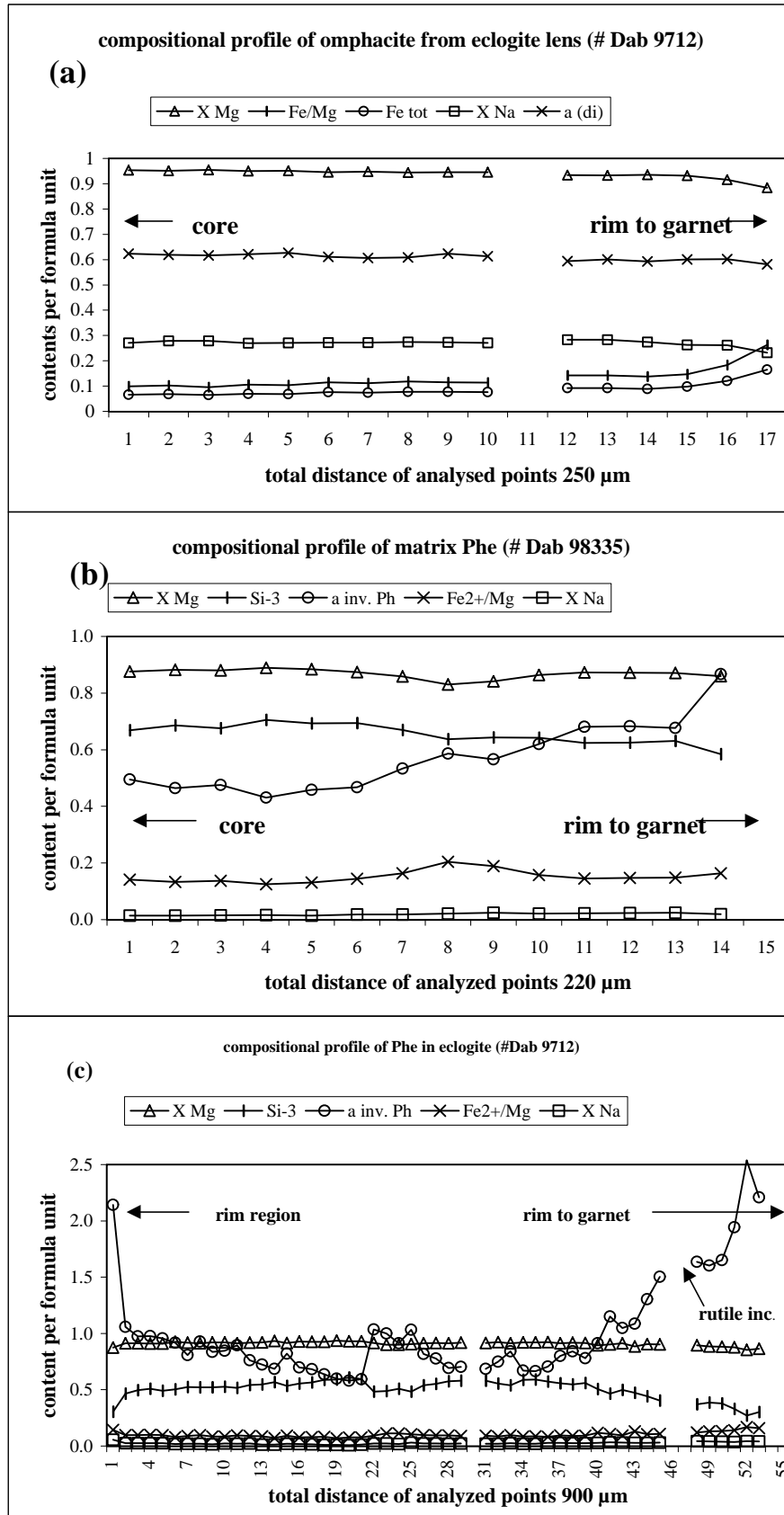
Figure 42: Chemical composition of a) omphacite and b) + c) phengite from eclogite samples calculated from equally spaced microprobe profiles. Diopside activity in a) is calculated after Holland (1990) at 700 °C, inverse Tschermaks activity for phengite is calculated as ideal (cf. Carswell et al. 1997). X Mg = Mg / Mg+Fe2+; X Na = Na A / sum A; Si-3 = Si p.f.u. - 3. Note that the ferric iron content is fixed at 50 %, see text for detailed discussion.

omphacite has Si contents of 3.71-3.58 p.f.u., those in titanite have Si of 3.53-3.51 p.f.u. (Dab 9712) and grains occurring in the matrix show Si of 3.59-3.30 p.f.u. Phengite occurring at the contact of eclogite to calc-silicate rock (Dab 9712) shows Si contents of 3.6-3.21 p.f.u. Notably, neither all grains within a single sample, nor all samples, bear phengite with high Si contents (cf. Table A5). Especially, matrix grains are considerably lower in Si in certain samples, although, inclusions of phengite always show elevated celadonite-component, justifying the assumption that at least high Si-phengite is part of the peak-paragenesis.

The highest Si contents are recorded in or towards the centre of the single phengite grains. Si contents decrease towards grain rims, which also holds true for Fe^{2+}, Mg and the X_{Mg}. An increase in $X_{Na\ A}$ (up to 0.11) towards grain rims is most prominent in phengite at the contact of eclogite and calc-silicate rocks. It is less pronounced in the matrix and inclusion grains of eclogites ($X_{Na\ A}$ 0.04) and calc-silicates ($X_{Na\ A}$ 0.06). The inclusions in titanite and kyanite have $X_{Na\ A}$ 0.03 and $X_{Na\ A}$ 0.05, respectively (cf. Fig. 44).

Carbonate

Two different types of carbonate occur within the eclogites and calc-silicates (Fig. 37c). In samples Dab 9712, 98408, 98411, and 9867, Fe-bearing dolomite occurs as a granoblastic matrix phase and sometimes as inclusions in omphacite. Whereas mineral zoning is absent in the inclusions, the matrix grains show a minor increase of calcite component (2-3 mole-%) at their straight grain boundaries. Carbonate in domains of retrogression is near pure calcite, which displays lobate grain boundaries to the other retrograde phases. At contacts to garnet, i.e. at the eclogite/calc-silicate boundary, formation of coronitic calcite around dolomite is observed (cf. Fig. 43b).

In sample Dab 98409 almost pure calcite inclusions surrounded by fractures are found in garnet, indicating probable aragonite stability during UHP metamorphism. Next to these carbonate grains, inclusions of relict coesite are found (Fig. 43c). Dolomite is the dominant carbonate phase in the matrix and occasionally shows irregular coronas of calcite. These observations suggest that calcite was the primary carbonate in the sedimentary protolith (at least in this specific sample) and dolomite probably formed by interaction with the metabasites.

Carbonate in other samples is exclusively Mg-Fe-bearing calcite, exhibiting variable grain shapes due to different degrees of deformation and/or recrystallisation experienced by the rocks.
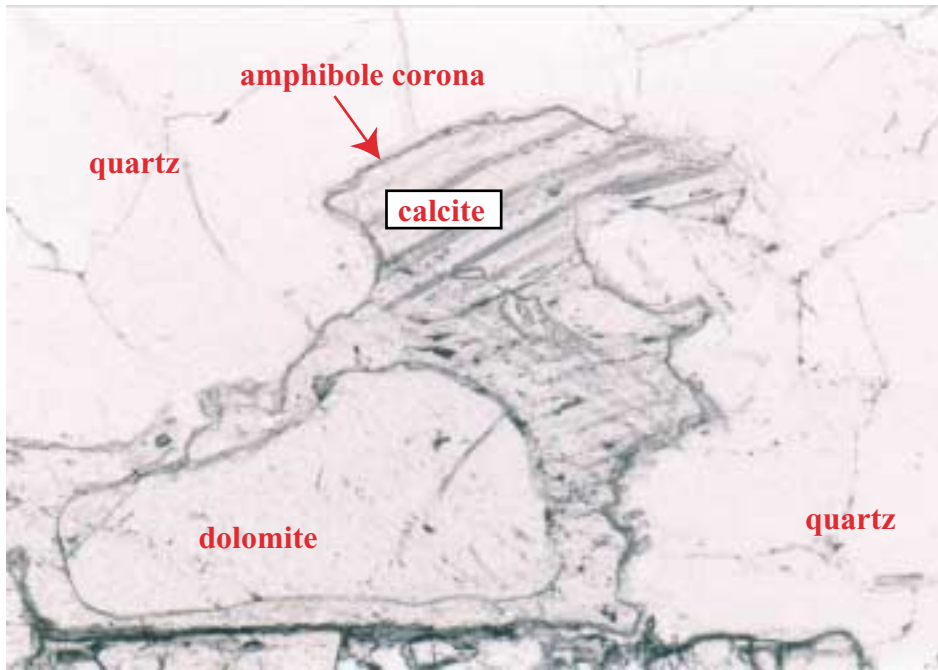
Figure 43b: Photomicrograph showing a dolomite grain with an irregular shaped calcite corona carbonate inclusions within garnet of the same sample are calcite (cf. Fig. 43 c). Note that an amphibole corona has developed between quartz and calcite. Sample Dab 98409, PPL, long side is 1.8 mm.
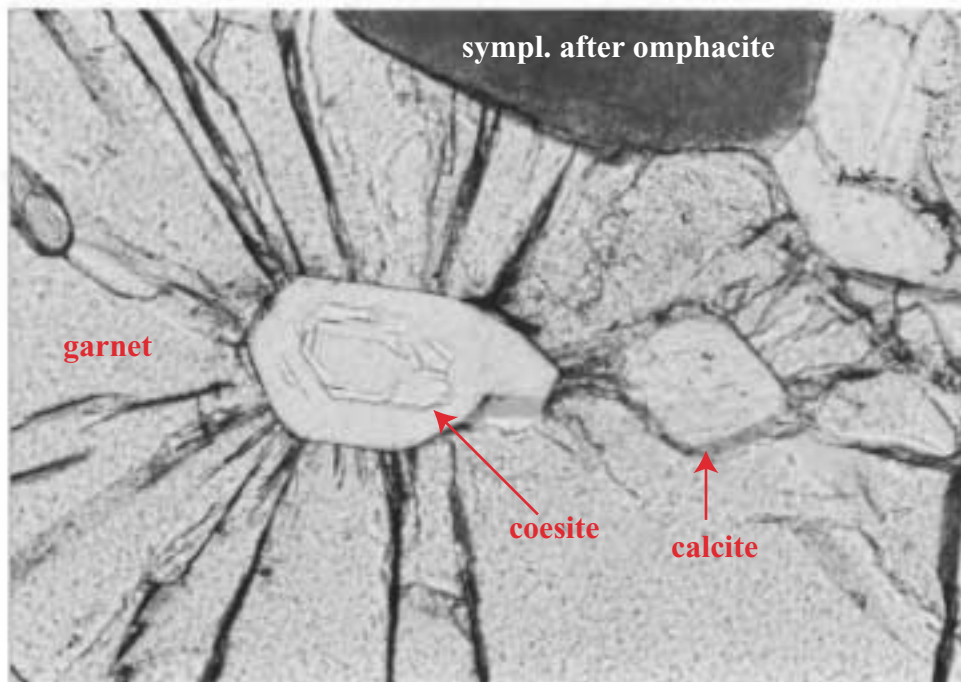
Figure 43c: Photomicrograph showing a relict coesite inclusion next to a calcite inclusion in garnet of sample Dab 98409. Note radial fractures around both inclusions and that carbonatic matrix grains are dolomite (cf. Figure 43b), see also text for discussion. PPL long side is 0.88 mm.
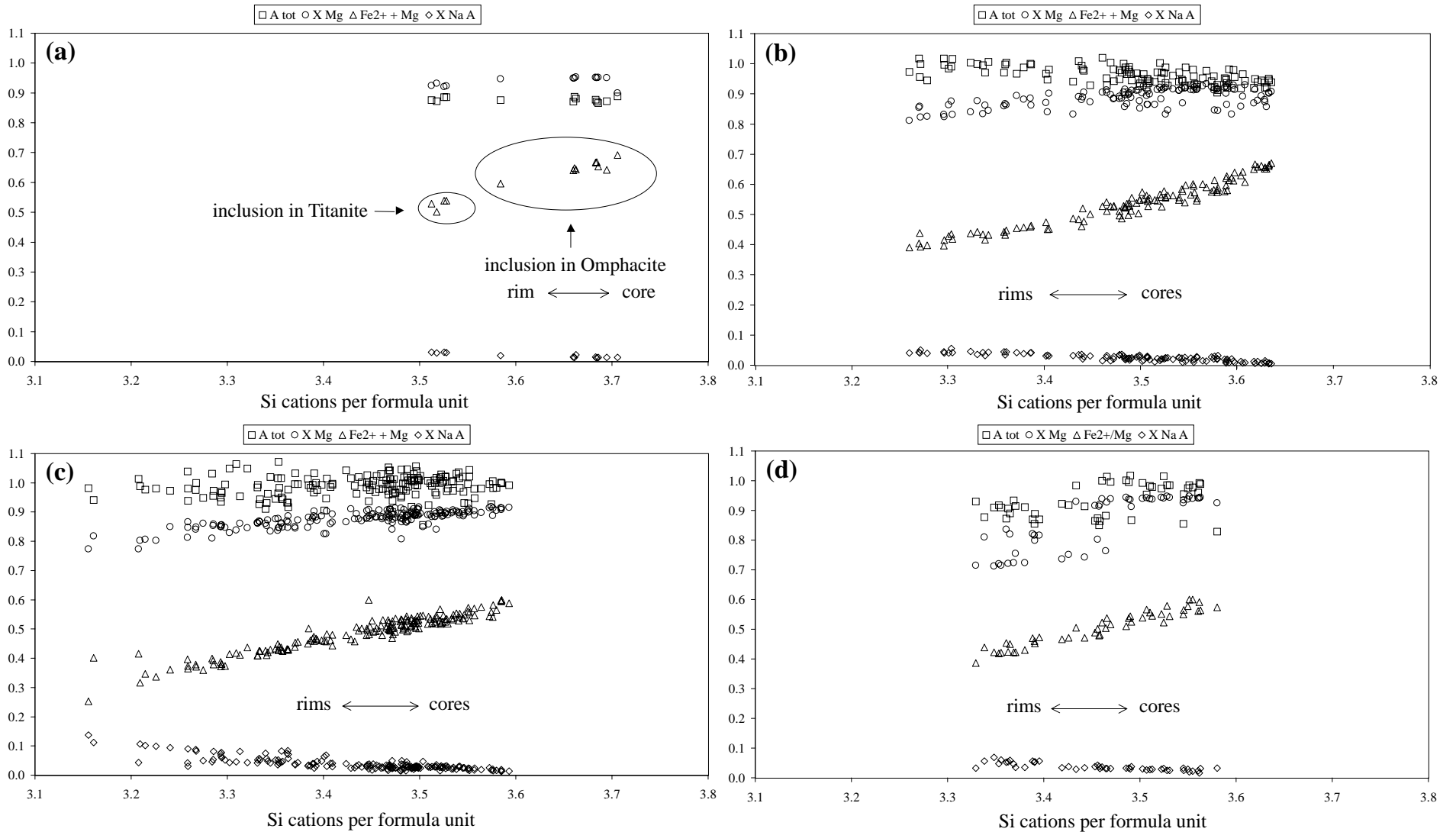
Figure 44: Plots of chemical parameters for phengite in distinct textural positions of eclogite and calc-silicate sample Dab 9712. a) inclusions in omphacite and titanite; b) in garnet/eclogite; c) at contact of eclogite lens and calc-silicate; d) in the matrix of calc-silicate. Note the core-rim trends present in relation to silica content per formula unit for a) - d) and the marked increase in Na for phengite with low Si contents occurring in the matrix of calc-silicate rock. See text for discussion and cf. Fig. 42b, c.

Amphibole

Amphiboles are classified according to the scheme recommended by Leake et al. (1997); the majority of the amphibole is calcic with ferro-pargasitic/pargasitic to edenitic compositions (Si 5.51 - 7.51 p.f.u.; X_{Mg} 0.38 - 0.8) but also tschermakitic to tremolitic species occur (Si 6.4 - 7.75 p.f.u.; X_{Mg} 0.71 - 0.95). In sample Dab 98382 calcic and sodic-calcic amphibole was recognised, ranging from ferro-pargasitic to pargasitic hornblende and magnesiotaramite, respectively, whereas barroisite is confined to sample Dab 9872.

5.2.3 THERMOBAROMETRY

Acquisition of equilibrium sub-assemblages

The investigated, high Si-phengite bearing rocks are suitable for a comparative thermobarometric evaluation because they span a large area of the marble-gneiss unit with differing bulk compositions, as indicated by Fe and/or Ca dominated garnet, and omphacite with variable Jd contents (cf. Figs. 37a, b). Furthermore, they offer a wealth of textural relationships among the considered phases (especially phengite, cf. Fig. 44) and show different grades of retrogressive overprint. Therefore, this suite of samples is ideal to test whether or not phases in textural equilibrium also reflect a chemical equilibrium as well as to obtain confidence on the P-T data for the rock association. Although the minerals show a good degree of homogenisation, the applied thermobarometry is highly sensitive to small compositional variations which can result in large differences in P-T data; this is exemplified by the plots of the activity values/factors used in the barometric expression (Waters and Martin 1993; cf. Figs. 38, 42). Those analyses of texturally identified kindred mineral sets with, in each case, the highest activity-values for garnet and those with the lowest a_{di} and $a_{inv\ Phe}$ for omphacite and phengite, respectively, were used to reflect different stages of the metamorphic history, manifested in the mineral compositions (cf. Table A5). For the peak of metamorphism these are compositions at or near the core; the values calculated from the rim compositions of the same grains were, whenever possible, used to calculate retrogressive P-T data.

Phengite occurring in the matrix with low Si contents and thus high inverse-tschermaks-activity values, are not considered to reflect UHP-related zonation patterns, instead they likely re-
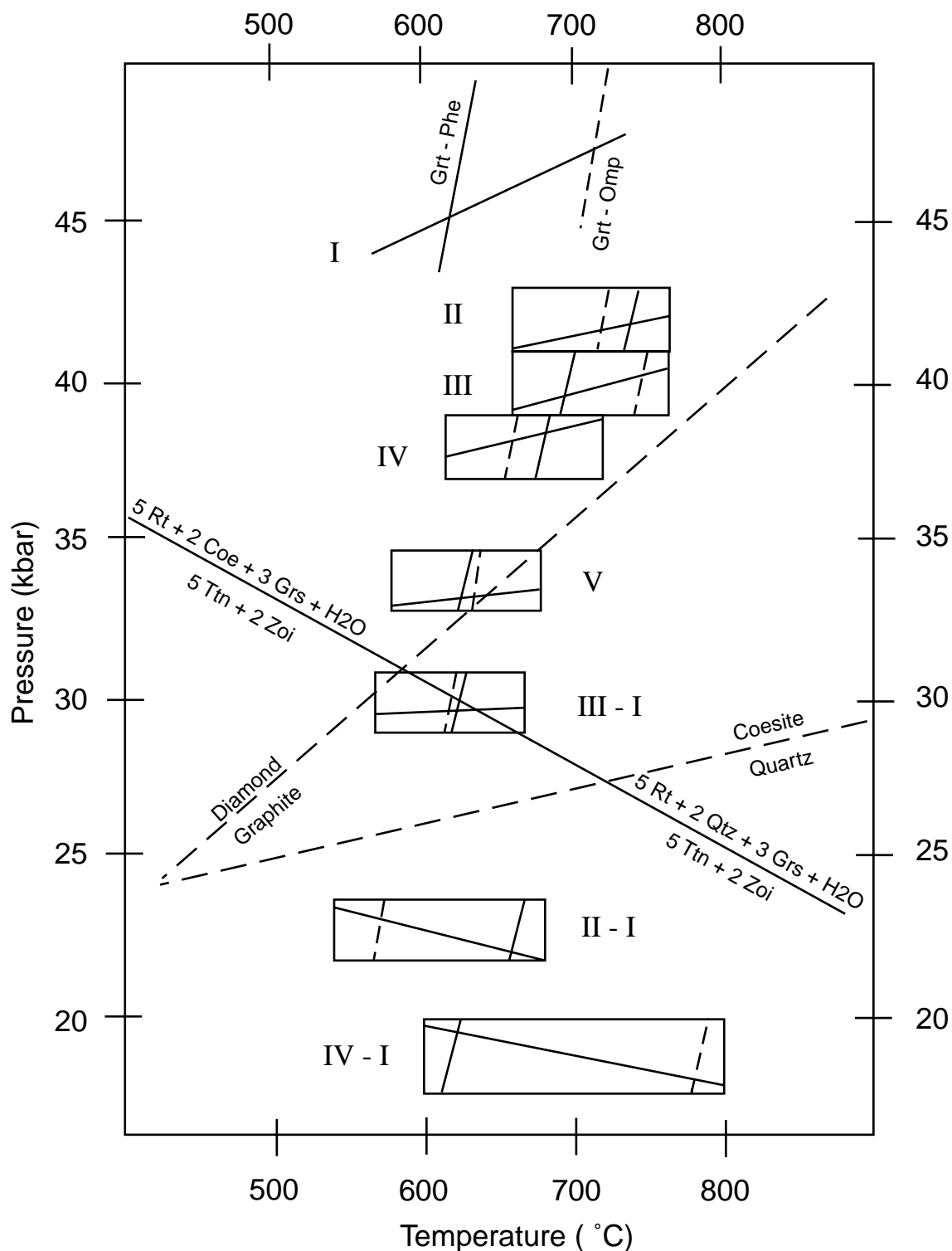
Figure 45: Summarising P-T diagram for eclogite and calc-silicate sample Dab 9712. Numbered boxes represent defined textural mineral triplets of garnet, omphacite and phengite (cf. Table A4, 5). Note that highest pressures with a large temperature spread are calculated if textural constrainst are ignored (I), while texturally related mineral triplets reveal fair agreement among the used thermometers (garnet-clinopyroxene, garnet-phengite) (II - V). Rim compositions of such minerals (II-I - IV-I) define a progressive cooling and decompression under upper mantle pressures during exhumation of the rocks. See also text for a detailed discussion.
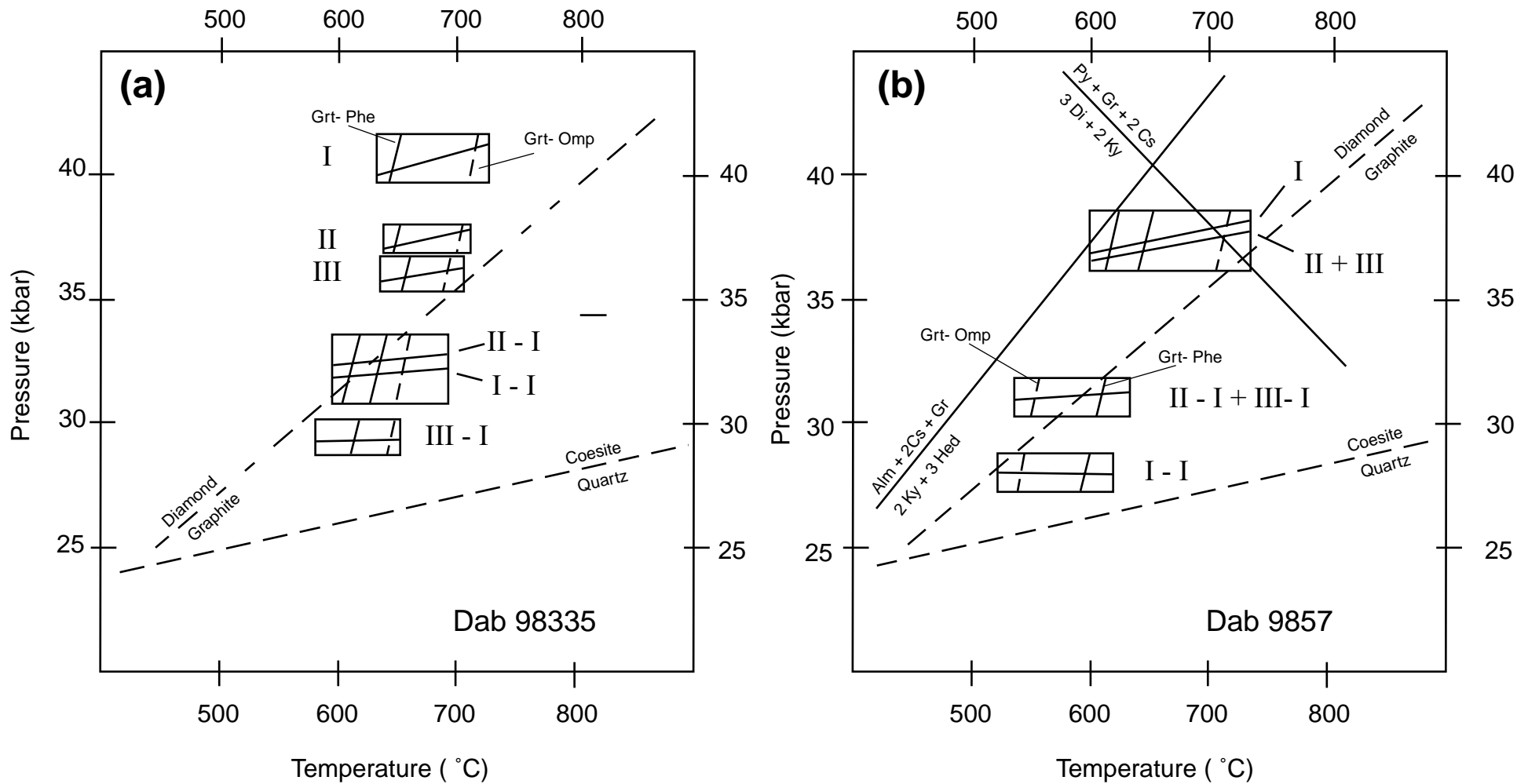
Figure 46: P-T diagrams for eclogite samples Dab 98335 and Dab 9857. Formation of kyanite and thus minimum pressures for sample Dab 9857 are indicated by the alumosilicate producing reactions and the P-T conditions calculated using phengite inclusion of the same grain (III); the use of matrix grains (I) only results in slightly higher pressures. Note that all mineral rim compositions define a similar cooling- and decompression-path as for sample Dab 9712 (cf. Fig. 45, Table A4, 5).

equilibrated fully or may have grown in response to thermal disturbance caused by intrusion of nearby Cretaceous plutons (e.g. Ratschbacher et al. 2000). The approach of Carswell et al. (2000) in strictly defining P_{max}, P_{min} and T_{max} compositional sets is not applied here, largely because i) from the textures in our samples such an approach cannot be justified and ii) the zonation patterns in the minerals do not constrain separate P_{max} and T_{max}.

P-T results

The calculated data are plotted for three key samples in Figs. 45 and 46 and are listed correspondingly for all samples in Table A5; the mineral analyses used for the P-T plots are listed in Table A4.

For the two eclogite samples with the highest Si contents in phengite (3.69-3.72 p.f.u.), UHP conditions of 42kbar at 730°C (Dab 9712) and 40kbar at 725°C (Dab 98335) were calculated using core analyses of phengite in the matrix of the eclogites and cores of adjacent garnet and omphacite. However, it has to be noted that in Dab 98335 only one relic omphacite inclusion was analysed in a garnet (Table A4). Furthermore, testing a potential equilibrium between an eclogite lens and surrounding calc-silicate rocks, (Dab 9712) maximum P-T conditions of 45-48kbar at 620-710°C were produced ignoring textural constraints and using the phengite with the highest Si contents (Si 3.71 p.f.u.) and its host omphacite (cf. Figure 34b) as well as the garnet with the highest activity value inside the eclogite lens. Somewhat lower pressures of 40 kbar at 720°C are calculated using the phengite (Si 3.58 p.f.u.) and omphacite in the matrix of the calc-silicates. From Figs. 45, 46 and Table A5 it becomes evident that P-T calculations of other sets of minerals, which define a textural equilibrium, reveal an evolution towards progressively lower pressure and temperature conditions. This is exceptionally well documented in Dab 9712, where a decrease in P-T values (down to ~30 kbar and ~600°C) is coincident with textures indicative of changing metamorphic grade (e.g. phengite included in porphyroblastic titanite; cf. Fig. 36). In contrary, one sample (Dab 9712, cf. Figure 45) reveals an increase in temperature (up to 780°C) at the lowest obtained pressures (< 20kbar), with a large spread between the garnet-omphacite, the garnet–phengite geothermometer. This may be assigned to mineral chemical disequilibria possibly induced by the thermal effect of the Cretaceous granitoids.

Thus, the P-T data constrain a cooling in the order of >10°C/kbar following the peak of UHP

metamorphism, still under pressures, corresponding to upper mantle depth.

4.3 PETROLOGY OF THE GANGHE UNIT

4.3.1 PETROGRAPHY

As the goal of this thesis is documentation of a common UHP overprint in the different lithological units, petrographical description of the Ganghe Unit is restricted to selected aspects of the metabasites relevant for thermobarometry and only touches on the felsic and non-eclogitic rocks. Thus these two rock types are described separately and their mineral assemblages are listed in Table A6.

Eclogite

As evident from field relations (above) metabasites (tuffs, lavas etc.) occupy stratigraphic positions, thus only four samples are selected for description.

Dab 9933 stems from the outer portion of a dyke cross-cutting the "non"-metamorphic volcanic breccia and is therefore one of the key samples to provide evidence for field-relations and P-T conditions. The central part of the 1 metre thick dyke underwent strong retrogression and exhibits an epidote-amphibolite facies assemblage with only relict garnet. In thin-section Dab 9933 has two generations of garnet, one defined by quite large and intensively fractured porphyroblasts (half a mm in size): Small, partly euhedral or xenomorphic garnet grains coexisting with equigranular epidote, rare omphacite, rutile (partly replaced by titanite) and quartz in the matrix form the second group. Epidote is hyp-idiomorphic whereas quartz often exhibits lobate grain shapes. Omphacite is a little bit coarser grained and fractured what is absent in the other phases. The minerals show no preferred orientation. The large garnet grains contain quartz inclusions with radial fractures (cf. Fig. 47), possibly formed after coesite, whereas the smaller garnet and omphacite lack such inclusions. However, epidote frequently has mono-crystalline quartz inclusions, some of which have fractures developed around them, but they are by no means texturally comparable to those definitely/assumed formed after coesite. Thus an eclogitic paragenesis includes large garnets, omphacite and rutile. Due to the low-pressure silica polymorph inclusions in epidote, this phase should have formed after the rocks crossed the
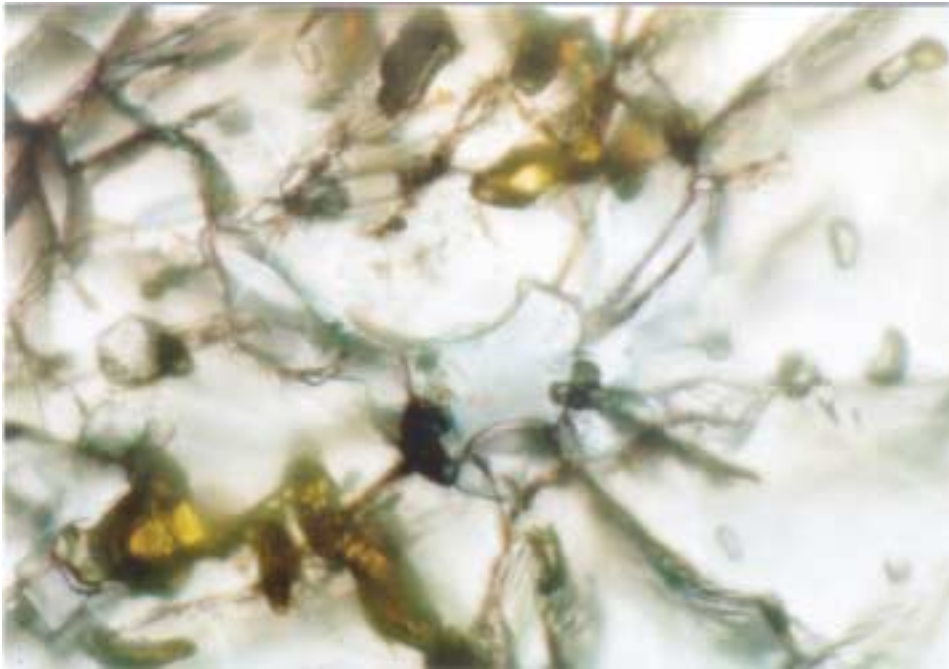
Figure 47: Photomicrograph showing a possible former coesite inclusion completely replaced by quartz within garnet of eclogite sample Dab 9933 (mafic dyke). Note the radial fractures around the inclusion. PPL, long side is 0.22 mm.
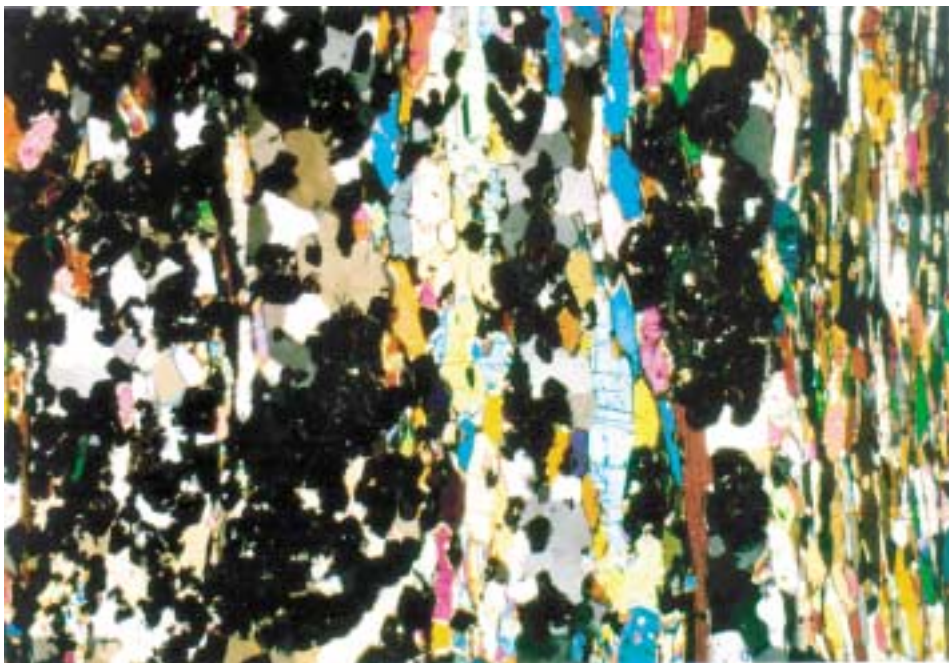
Figure 48a: Photomicrograph showing the compositional layering in eclogite sample Dab 99206. See text for discussion. XPL, long side is 6.48 mm.
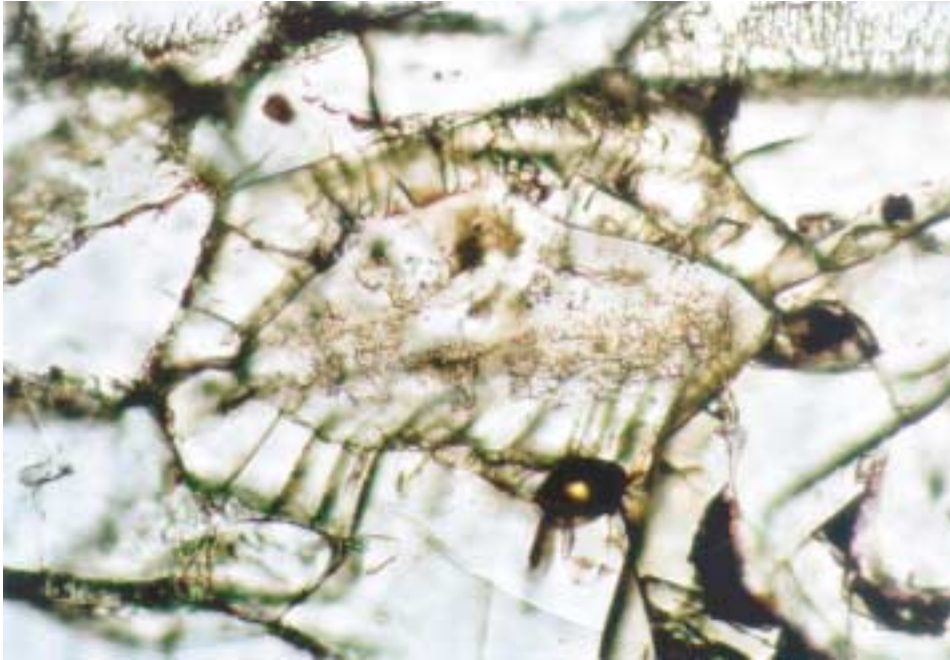
Figure 48b: Photomicrograph showing a possible former coesite inclusion within omphacite of eclogite sample Dab 99119. Note the radial fractures around, and the mineral with a higher relief within, the inclusion (likely chlorite, cf. Parkinson 2000). PPL, long side is 0.88 mm.

coesite - α quartz boundary.

Other metabasites are either strongly compositionally layered, and/or foliated (Dab 99119, 99206) as well as unoriented (Dab 99122). In particular Dab 99206 shows a strong chemical zoning with alternating porphyroblastic garnet-quartz, stretched and aligned omphacite-quartz-garnet-zoisite and omphacite-phengite-zoisite/clinozoisite-rutile layers (cf. Fig 48a). Most of the minerals exhibit a granoblastic shape indicating that recrystallisation post-dates texture formation; kyanite is rarely present but not aligned in the foliation. Porphyroblastic amphibole overgrows the foliation, signaling formation after the penetrative deformation-recrystallisation event. Coesite could not be identified positively, however a quartz inclusion with probable chlorite points to the former stability of the high-pressure polymorph (cf. Parkinson 2000, Fig. 48b). Omphacite is only marginally affected by breakdown to symplectites of amphibole and plagioclase. Although this sample is classified as a metabasite, large quantities of quartz occur in the matrix. The large amount of quartz and the strong compositional layering (cf. Fig. 48a) likely originates from the protolith nature which is proposed here to be a mafic-intermediate tuff.

Sample Dab 99119 is also a layered metabasite but it is not compositionally zoned. Stretched zoisite/clinozoisite and rare phengite define a foliation. Garnet, rutile, quartz and omphacite are hardly stretched. Coesite or textures indicative for its former stability are not present, however the minerals, and especially quartz exhibit a granoblastic shape voting for a recrystallisation event post-dating the possible coesite stability. Amphibole and epidote overgrow the foliation, again pointing to their retrogressive nature, and the same is true for symplectites after omphacite and rare amphibole coronas around garnet. As for the above sample, large quantities of quartz indicate an intermediate rather than strictly mafic composition of the protolith.

In contrast, Dab 99122 is an unfoliated sample of a metabasite, consisting of porphyroblastic garnet, omphacite with some phengite, kyanite, rutile and rare quartz. Large amphibole crystals, zoisite and minor chlorite have likely formed at the expense of the former phases, however, most of the eclogitic minerals are well preserved.

Non-eclogitic rocks

Three samples from the Ganghe unit were chosen for petrologic studies. The first is the felsic volcanic breccia, which is cross cut by a mafic dyke (Dab 9933, see above), and the second

is an acidic ash layer, which preserves syn-sedimentary textures (Dab 99125). The porphyroblastic mylonite, bounding the unit to the basement gneisses of the Changpu Unit is the source of the third sample (Dab 99210).

The volcanic breccia consists of grey- to black angular to rounded clasts which are aligned in a fine-grained white matrix. The lithoclasts are variable in size and range from mm to c. 6 cm, and neither reaction rims nor individual minerals are obvious in hand specimen among both the matrix and the lithoclasts. Whereas whole rock analyses classify the dark lithoclasts (Dab 99186) as andesites (not shown), the composition of the matrix was not analysed in great detail. However, thin-section studies revealed poly-crystalline quartz grains, epidote and opaque minerals embedded within a extremely fine grained matrix, which was also "homogeneous" at EMP magnification. Thus an XRD analyses was performed in order to detect potential relicts of the UHP overprint (cf. Fig 49a). According to the obtained spectra, quartz is the major component with some albite and muscovite, ferrosilite is very weakly indicated and no X-ray peak could be attributed to any high-pressure mineral (e.g. garnet or jadeite). However, since only minerals with about 5 vol.% can be detected by this method it is a valuable tool to document that, if any, minor amounts of reaction took place during metamorphism. Alternatively, any record of an possible UHP overprint has been ereased during a greenschist-facies overprint.

The ash layers are commonly mm-sized whereas coarse grained layers or pockets with angular minerals (max. mm) are rare. Thin-section studies revealed only feldspar, quartz and opaque minerals in the fine grained portions, whereas the coarser minerals are feldspar. An XRD spectrum indicates, as for the breccia, quartz, albite and probably muscovite (fit with a synthetic standard) as the major components and no peaks fit to minerals indicative of a high pressure metamorphic overprint (cf. Fig. 49b).

As mentioned earlier, the mylonite sample (Dab 99210) consists of large feldspar porphyroblasts (up to 4 cm in size) in a well foliated two-mica, epidote, titanite, rare chlorite, quartz- and feldspar-bearing matrix. The rims of the porphyroblasts are nearly inclusion free but the central parts have large amounts of quartz-blebs, white mica, epidote, calcite and also rare garnet (cf. Fig. 50). The inclusions are aligned and define a foliation which is oblique to the main foliation of the matrix. The porphyroblasts show in some domains recrystallisation textures and also pressure-twins, as indicated by the conic shape of the twins.
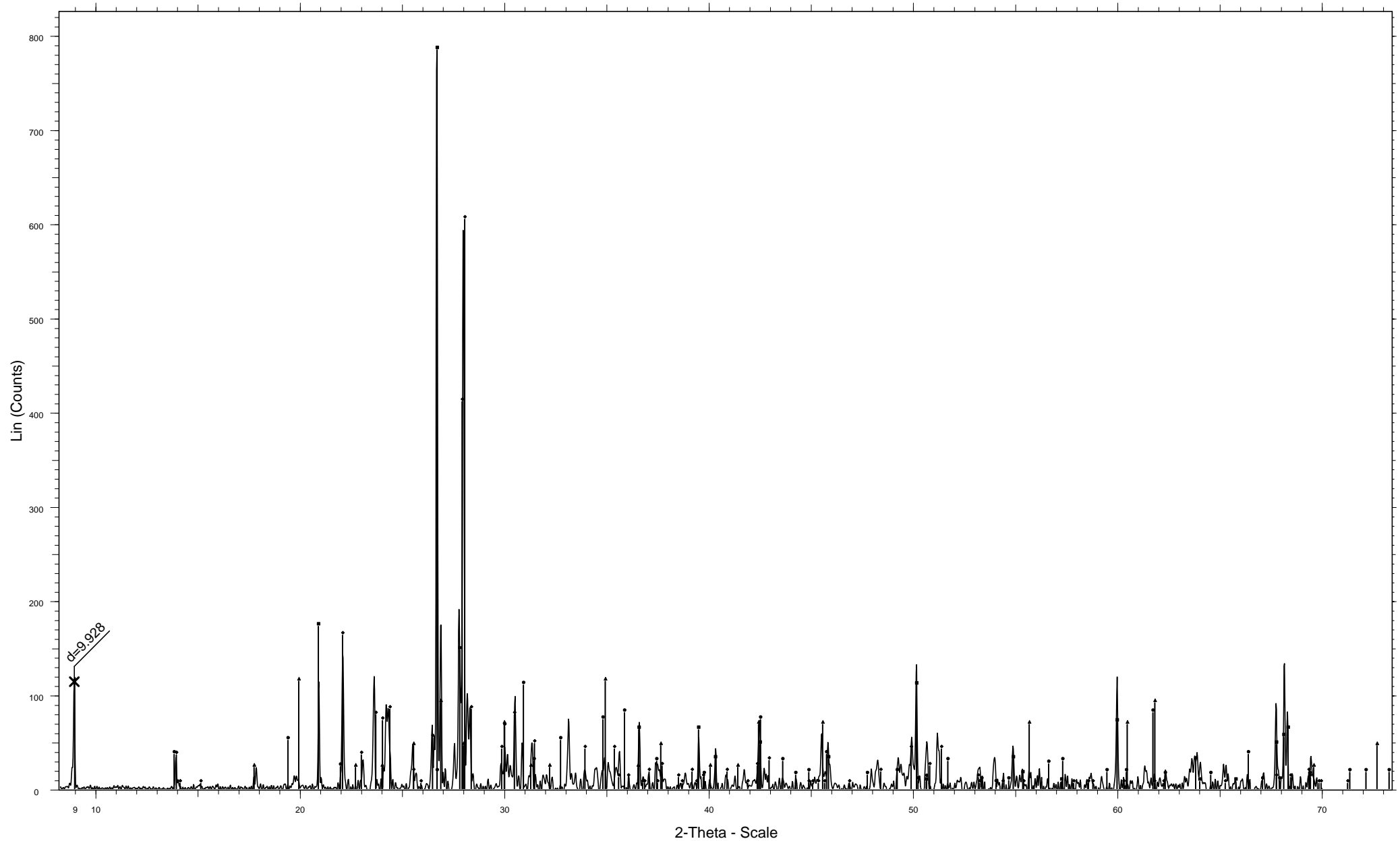
Figure 49a: XRD pattern of andesitic components in volcanic conglomerate (Dab 99186).
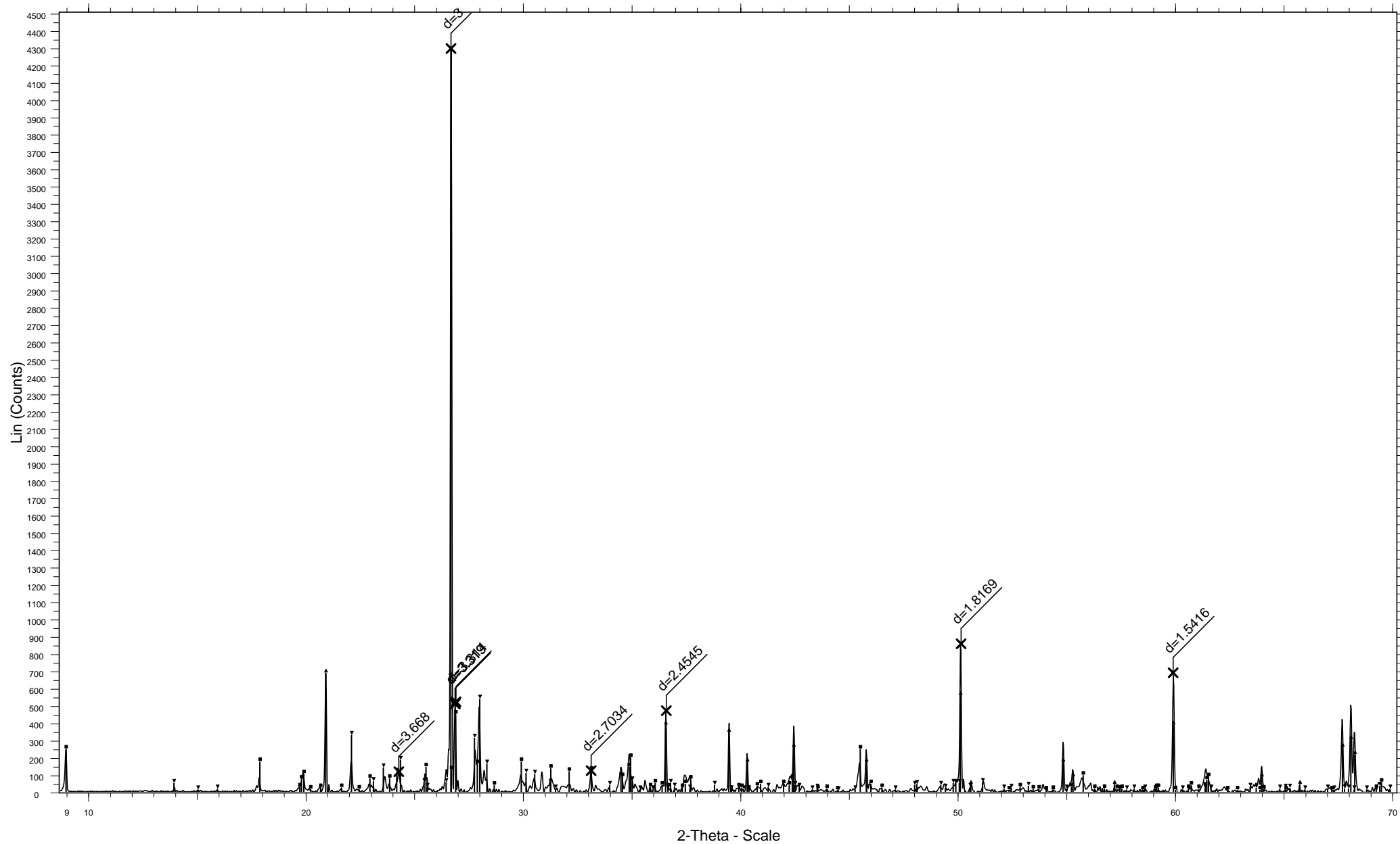
Figure 49b: XRD pattern of ash-layer sample Dab 99125.

muscovite layer

a narrow muscovite layer. See text for discussion. Sample Dab 98210, XPL, long side is approx. 15 mm.

4.3.2 MINERAL CHEMISTRY

Dab 9933 eclogite-facies dyke

The compositions of the two different types of garnet reveal a complex reaction history and form at least two groups in a ternary diagram (cf. Fig. 51). The cores of the large porphyroblasts likely represent an eclogitic stage but increasing X_{Mg} and decreasing X_{Ca} in their rim section point to changing P-T conditions. In contrast, the small garnets are non-uniform from grain to grain and also from core to rim of individual but neighbouring grains (cf. Fig. 52a). At contacts to quartz no reaction textures, like formation of plagioclase is observed. Since epidote formation signals influx of a fluid phase during retrogression, the highly variable garnet compositions of both the large and small grains may reflect interaction with, or formation in the presence of, an aqueous fluid phase and/or locally disturbed reaction kinetics not only for the bulk rock but also among garnet-garnet (cf. Fig. 52a). Further it is worth considering that the smaller garnets might be pieces of the larger ones, broken off during a possible brittle deformation, and later recrystallised later with the influx of a fluid phase. However, the garnet chemistry was not checked thoroughly enough to constrain their true nature.

Omphacite revealed no prominent compositional zoning, except for the Fe^{3+} content, which decreases from core to rim and in some grains again increases at the rim (cf. Figs. 53a). Due to the higher Fe_{tot} (c. 6 wt.%) charge balance values (Droop 1987) are applied and an average value of 70% is used in thermobarometry. Their endmember plot further emphasises their homogeneous composition (Fig. 54).

Dab 99119, 99122, 99206 - Eclogite
Garnet

Garnet in part shows a pronounced zoning from core to rim (cf. Figs. 51, 52c). Dab 99122 especially has a strong increase in X_{Ca} but a near constant X_{Mg} towards grain rims, whereas Dab 99206 garnet has decreasing X_{Ca} and X_{Mg} from core to rim. In contrast, garnet from Dab 99119 exhibits a flat compositional profile but a complex pattern of the plotted activity value which possibly reflects two-stage growth history. Again the garnet sections with the highest activity values are assumed to reflect the peak of metamorphism.
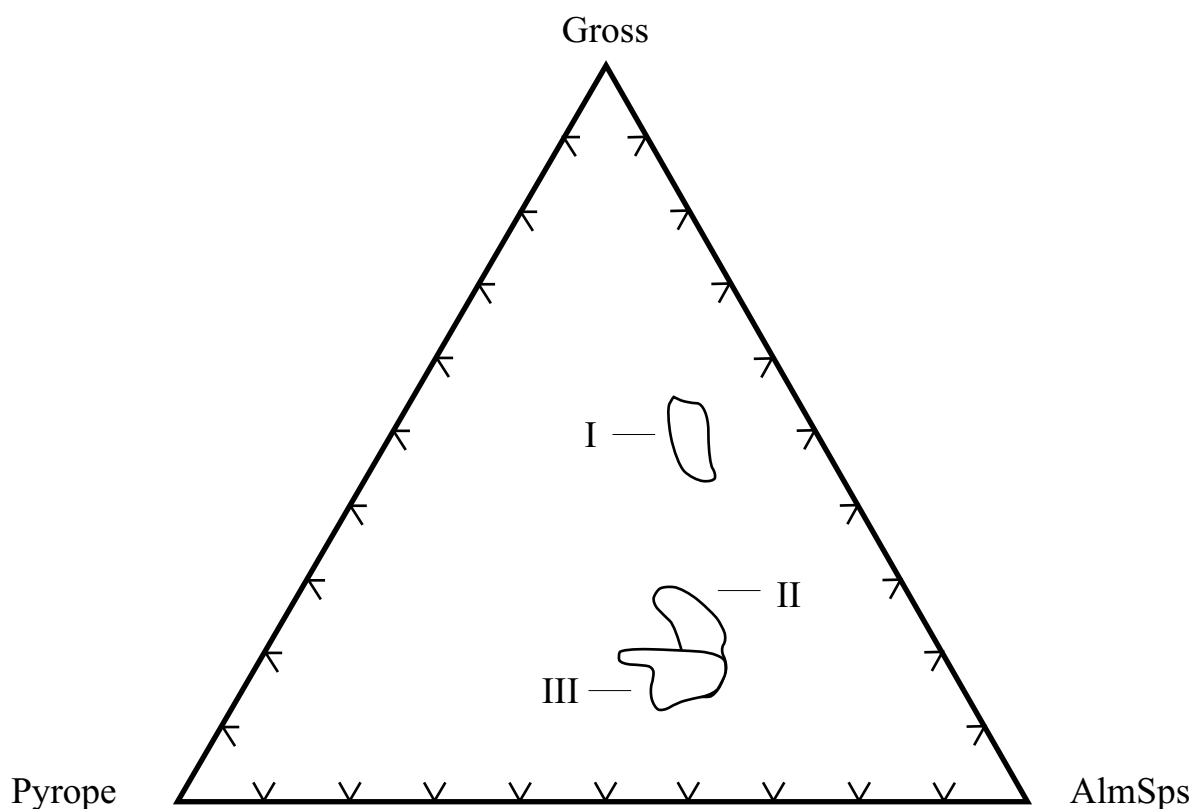
Figure 51: Ternary diagram showing fields of garnet endmember compositions from eclogite samples of the Ganghe unit. I - Dab 9933; II - Dab 99122 and 99206; III - Dab 99119. Gross - grossular; AlmSps - almandine + spessartine.
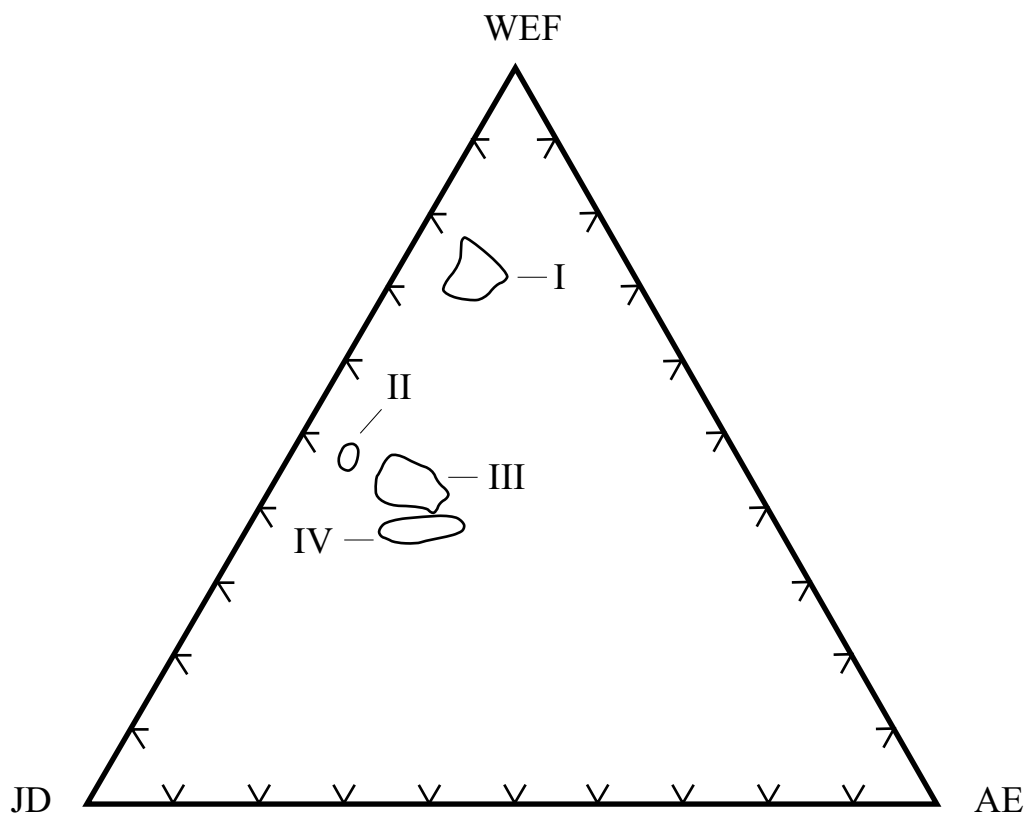
Figure 54: Ternary diagram showing fields of endmember compositions of omphacite from eclogite samples of the Ganghe unit. I - Dab 9933; II - Dab 99122; III - Dab 99119; IV - Dab 99206. WEF - wollastonite, enstatite, ferrosilte; JD - jadeite; AE - aegerine.
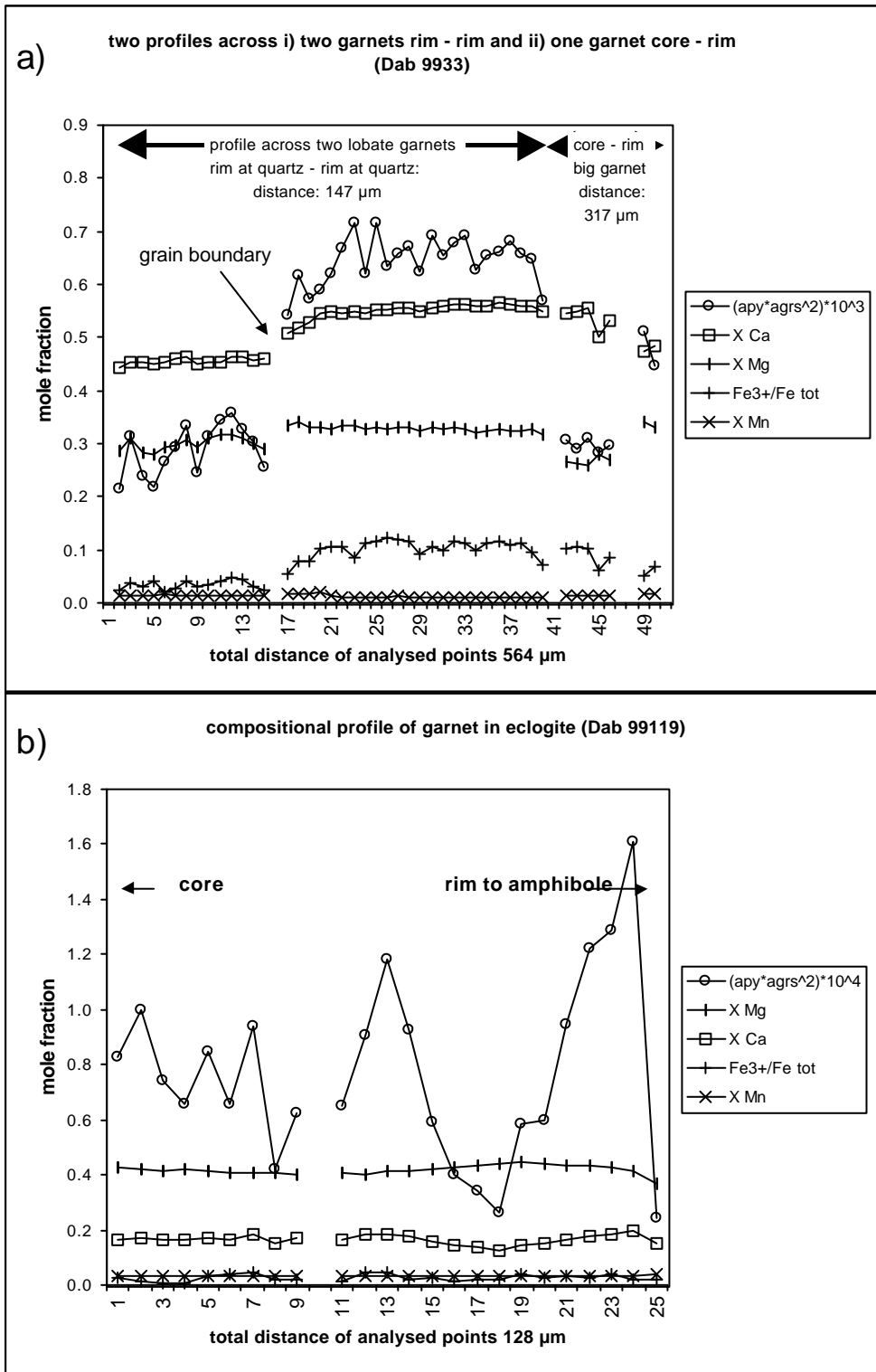
Figure 52 a, b: Chemical composition of garnet within eclogite samples of the Ganghe unit calculated from equally spaced microprobe profiles. See Figure 27 for explanation of abbrevations.
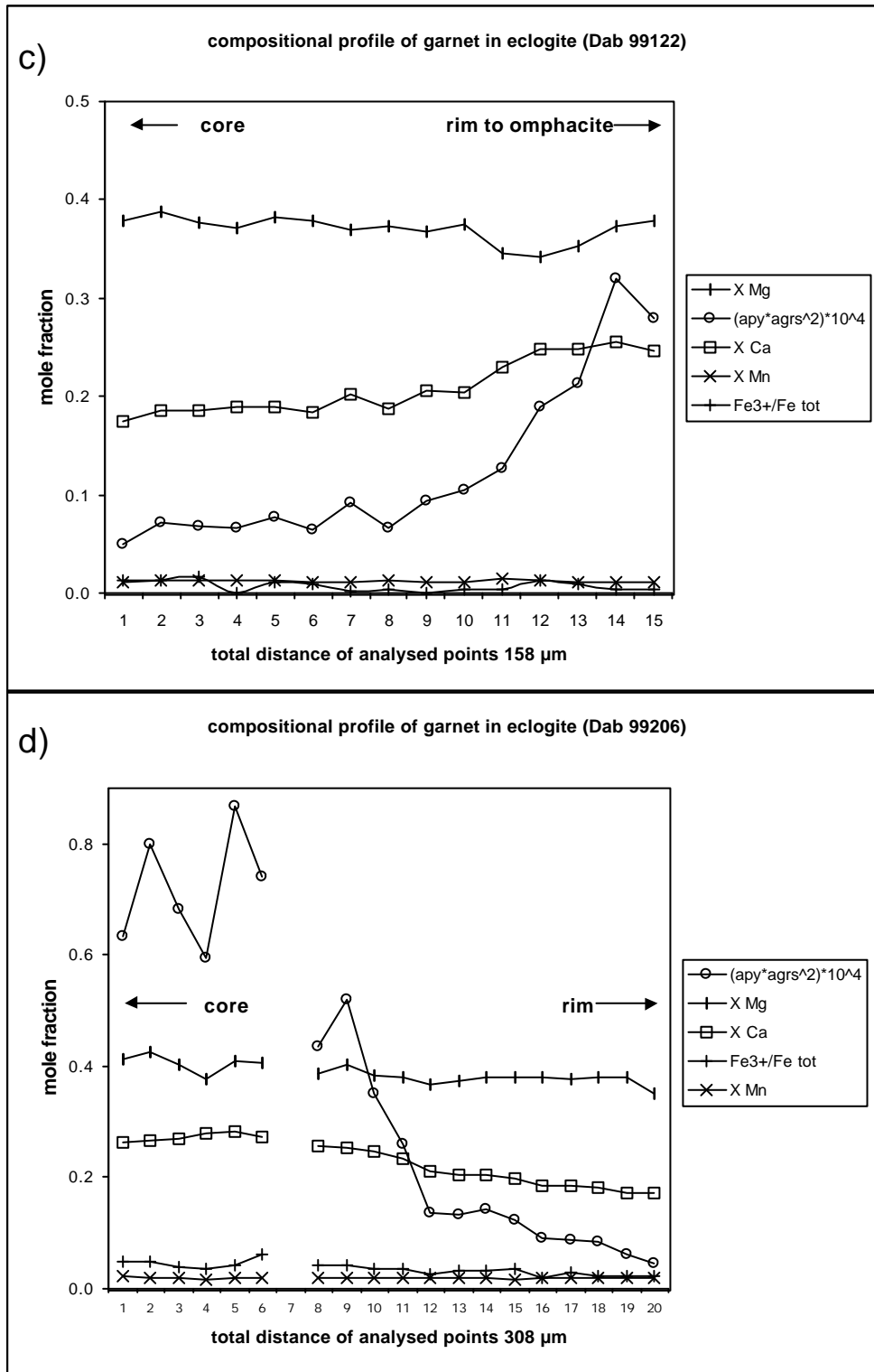
Figure 52 c, d: Chemical composition of garnet within eclogite samples of the Ganghe unit calculated from equally spaced microprobe profiles. See Fig. 27 for explanations of abbrevations.

Omphacite

All analysed grains revealed a consistent homogeneity from core to rim, and only at contacts to garnet are minor modifications observed. There, microprobe analyses did not meet robust criteria, compatible with a clinopyroxene analysis (i.e. wt.% and cation sum beyond the tolerance of 1.5 % and 1 %, respectively), probably due to amphibole and/or chlorite formation. From Figs. 53, 54 and 55 it can be seen that they scatter around Jd_{45} and have some minor variation in aegirine component.

Phengite

Phengite only exhibits a weak zoning with Si contents of up to 3.5 p.f.u. in the centre of individual grains (Dab 99119) moderately decreasing towards the rim. The same holds true for the X_{Mg}, which decreases as Fe_{tot} increases. There is no significant zoning in the paragonite component, however X_{Na} reaches up to 0.11 at rims of phengite in Dab 99119 (Fig 56). The inverse tschermaks-activity (cf. above) calculated from single analyses is additionally plotted (cf. Fig. 56) and follows the general trend from low values in the core regions to significantly higher ones at the rims. Thus it is clear that the portions high in Si p.f.u. and X_{Mg} represent equilibrium during UHP metamorphism.

Dab 99125 – acidic ash layers

For this sample only feldspar analyses are available due to its extremely fine grained texture. In a ternary diagram it can be seen that members of the potassium-feldspar family are present beside An-poor plagioclase (Fig. 57). It might be argued that K-feldspar was (meta-) stable during metamorphism and that the albite-rich grains stem from recrystallisation following a Jd-bearing clinopyroxene breakdown. Alternatively, the "original" feldspar composition might have been anorthoclase and trends towards albite and orthoclase may be a response to a late retrogression. Anyhow, this does neither explain the small grain size nor the preserved volcanogenic and syn-sedimentary texture with absence of reaction rims. Instead it is favoured here in a qualitative sense that this felsic lithology did not respond to elevation of P-T conditions for kinetic reasons due to a probable lack of a promoting fluid phase.
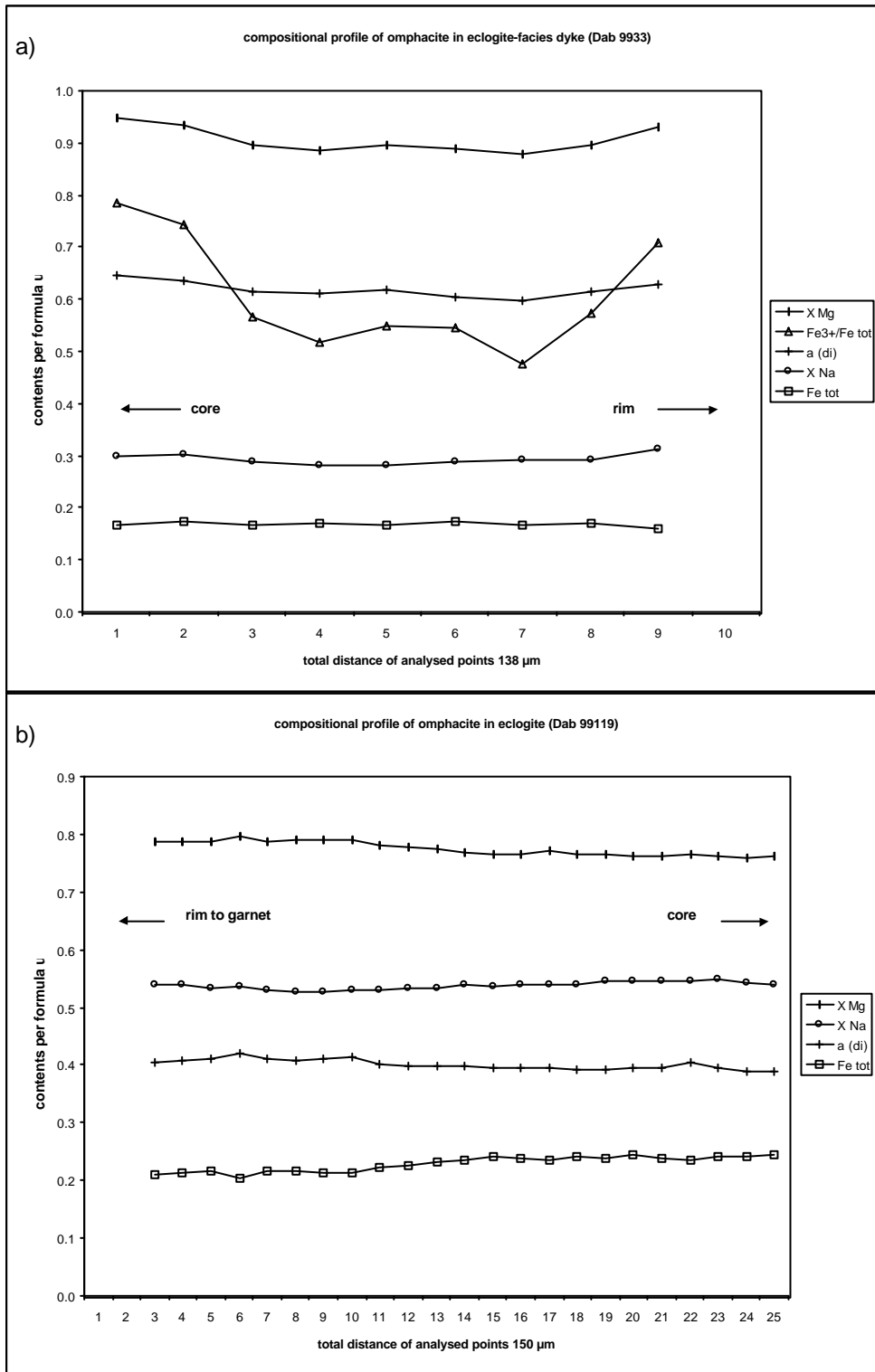
Figure 53: Chemical composition of omphacite within eclogite samples from the Ganghe unit calculated from equally spaced microprobe profiles. See Figure 42 for explanation of abbrevations. Note that due to higher Fe tot contents the ferric iron in a) has been determined by charge balance methods (Droop 1987).
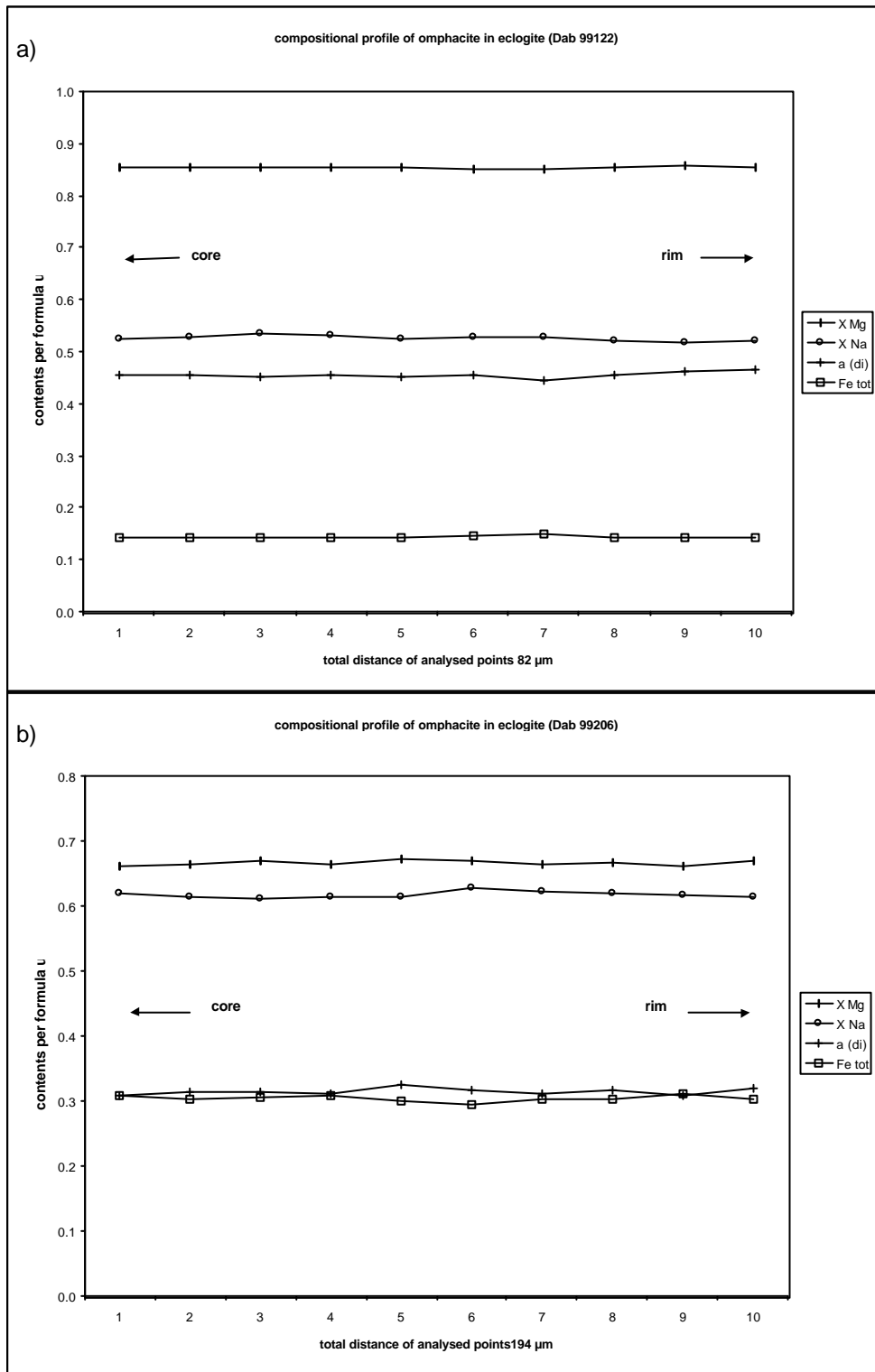
Figure 55: Chemical composition of omphacite within eclogite samples from the Ganghe unit calculated from equally spaced microprobe profiles. See Figure 42 for explanation of abbrevations.

a) compositional profile of phengite in eclogite (Dab 99119)

b) compositional profile of phengite in eclogite (Dab 99122)

c) compositional profile of phengite in eclogite (Dab 99206)
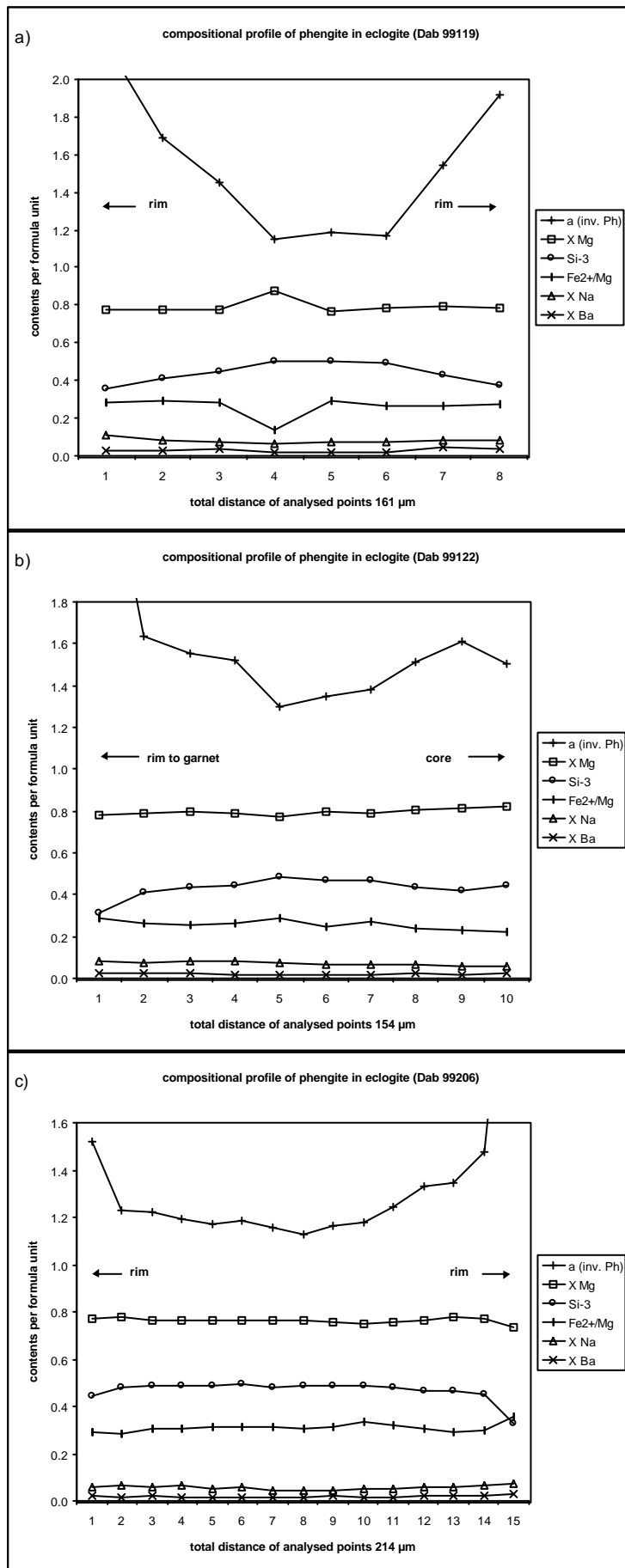
Figure 56: Chemical composition of phengite within eclogite samples from the Ganghe unit calculated from equally spaced microprobe profiles. Inverse Tsermaks activity is calculated as ideal (cf. Carswell et al. 1997); X Mg = Mg / Mg + Fe2+; Si-3 = Si p.f.u. - 3; X Na = Na A / sum A; X Ba = Ba A / sum A.

Or

**Fig. 57: Volcanoclastic samples
from the Ganghe Unit**

Ab

An

Or
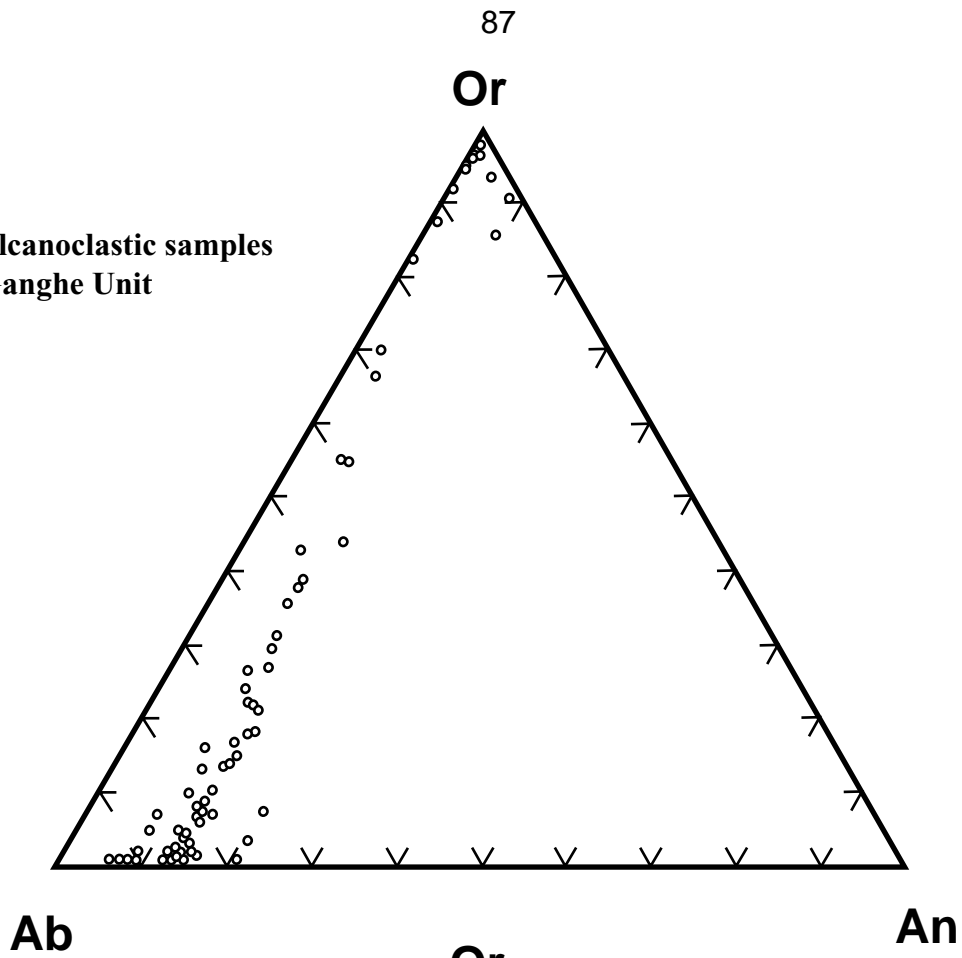
Fig. 58: Mylonite (Dab 99210)

Ab

An
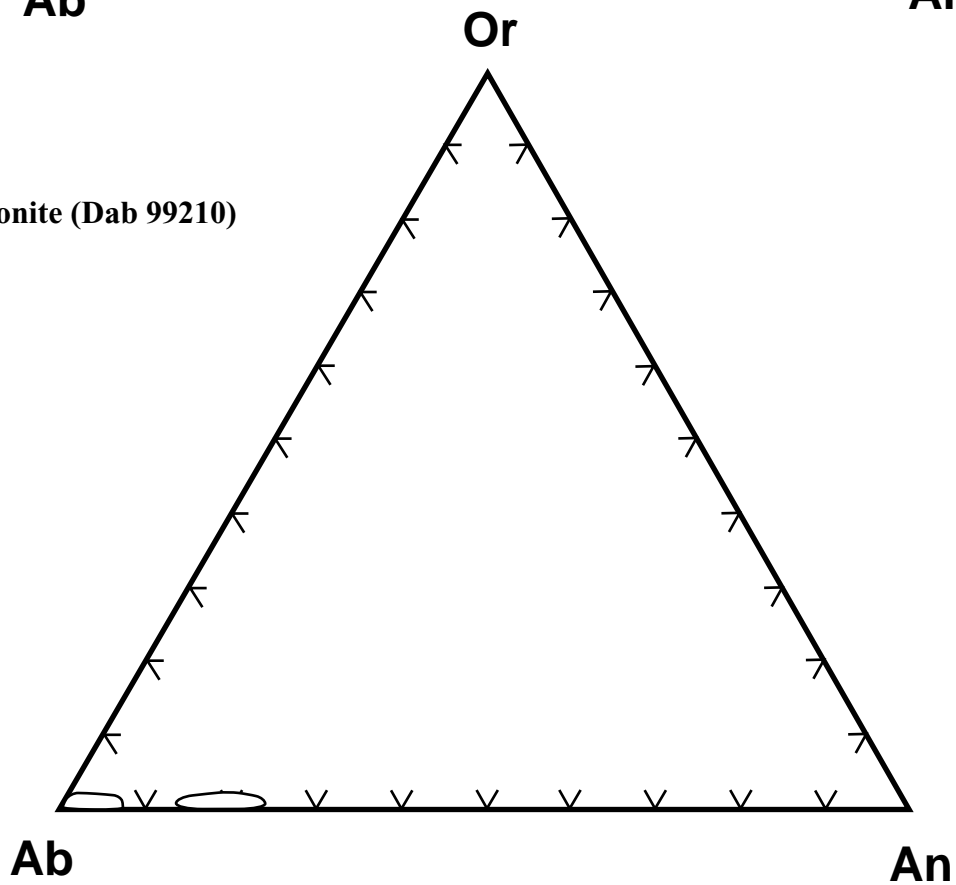
Figures 57 and 58: Ternary plots showing endmember compositions of feldspar from volcanoclastic
samples (Dab 99125, 99186) and from the blasto-mylonite (Dab 99210) bounding the Ganghe Unit to the
basement of the Changpu unit.
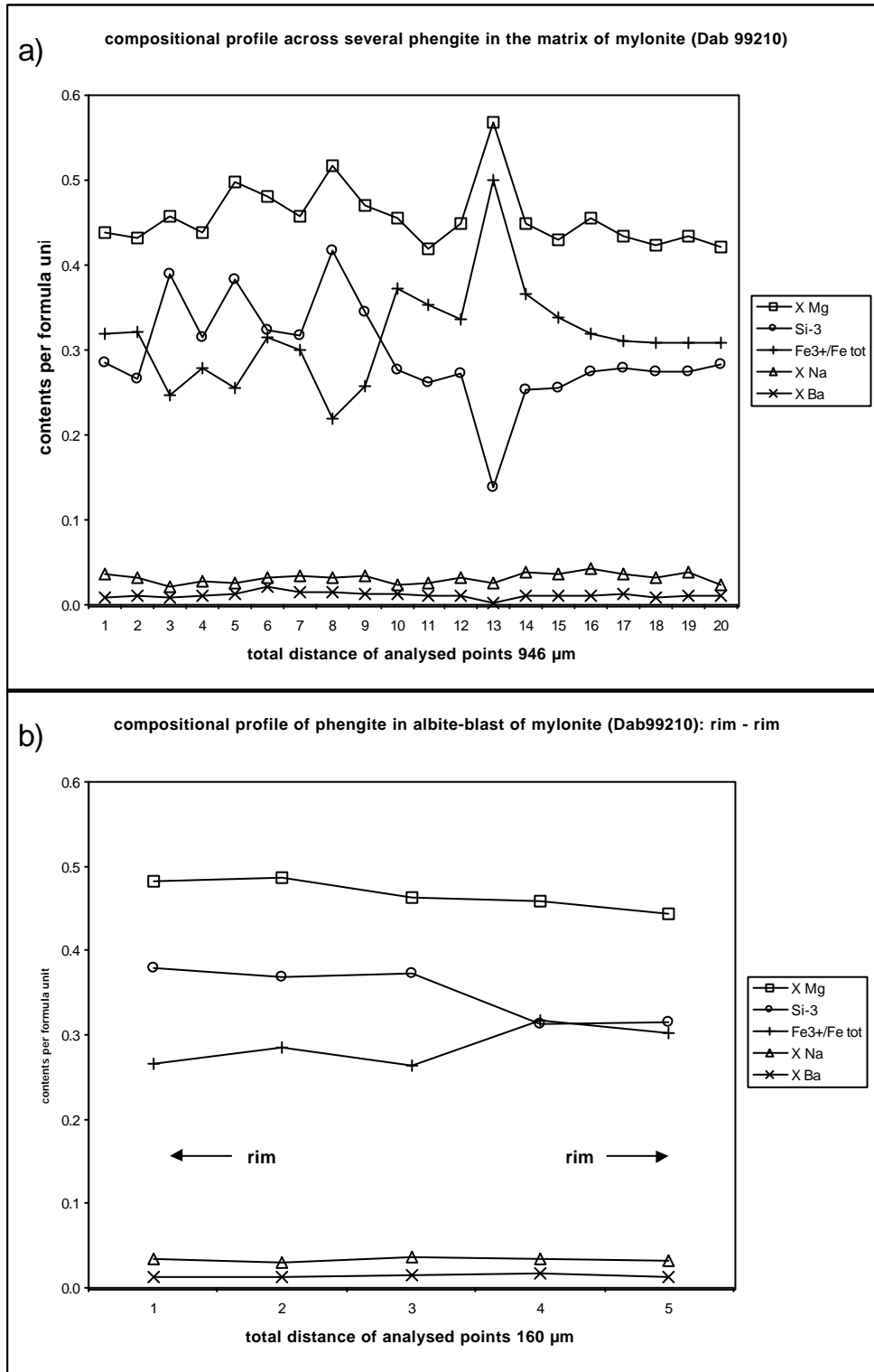
Figure 59: Chemical composition of phengite in the a) matrix and b) inclusion within albite-blasts of mylonite sample Dab 99210 calculated from equally spaced microprobe profiles. See Figure 56 for explanation of abbrevations.

Dab 99210 - Mylonite

While plagioclase in the matrix is richer in anorthite (ab $_{78-85}$) the porphyroblasts show near albite endmember composition (ab$_{>93}$, cf. Fig.58). Garnet included in the big albite grains has a core composition of Grs$_{50}$Alm$_{30}$Py$_3$Sps$_{15}$An$_2$ whereas the rims are distinct showing Grs$_{37}$Alm$_{38}$Py$_2$Sps$_{20}$An$_2$. White mica in the albite porphyroblasts is phengite with Si contents of 3.4 p.f.u. in the core and 3.3 p.f.u. at the rim. The X$_{Mg}$ is around 0.5 and shows minor variation from core to rim. Phengite in the matrix is not very distinct in composition but varies irregularly across several grains (cf. Fig. 59). Some epidote grains exhibit a skeleton-like shape, have a prominent Mn content (ca. 9 wt.%) and often occur within plagioclase grains in the matrix.

4.3.3 THERMOBAROMETRY

The results of the thermobarometric calculations are plotted for the single samples in Figs 60-62 and a representative set of mineral analyses is listed in Table A7. However, in conclusion it has to be said that they are somewhat ambiguous, because they do not uniformly reflect UHP conditions. In particular the barometer of Waters and Martin (1993) gives inconsistent results. It indicates pressures near the coesite-quartz transition for Dab 99206 (Fig. 60a), but distinctly lower pressures in the stability field of quartz are indicated for Dab 99119 (Fig. 60b). For Dab 99122 the pressures of the samples from the other units are reproduced (Fig. 61a). Temperature estimates are in better agreement, although for Dab 99206 they indicate T>800° C. However maximum P-T conditions for the kyanite stability in sample Dab 99119 are compatible with an alleged UHP metamorphism. The titanite- and zoisite- as well as the paragonite-forming reactions at least indicate a P-T regime close to coesite stability. For Dab 9933 only minimum conditions within the quartz field are calculated due to lack of critical minerals (Fig. 61b). The reasons for the inconsistency in P-T data may arise from retrograde modification of the phengite composition, or may be due to erroneous choice of the garnet analyses used for the calculations. However the temperatures of the garnet-clinopyroxene and garnet-phengite Fe-Mg exchange do not support this interpretation. In the light of the non-metamorphic felsic rocks one might not be surprised to detect some degree of disequilibrium in the more mafic rocks, too. Anyhow, at least one sample gives thermobarometric evidence for UHP metamorphism and possible quartz pseudomorphs after coesite point in the same direction.
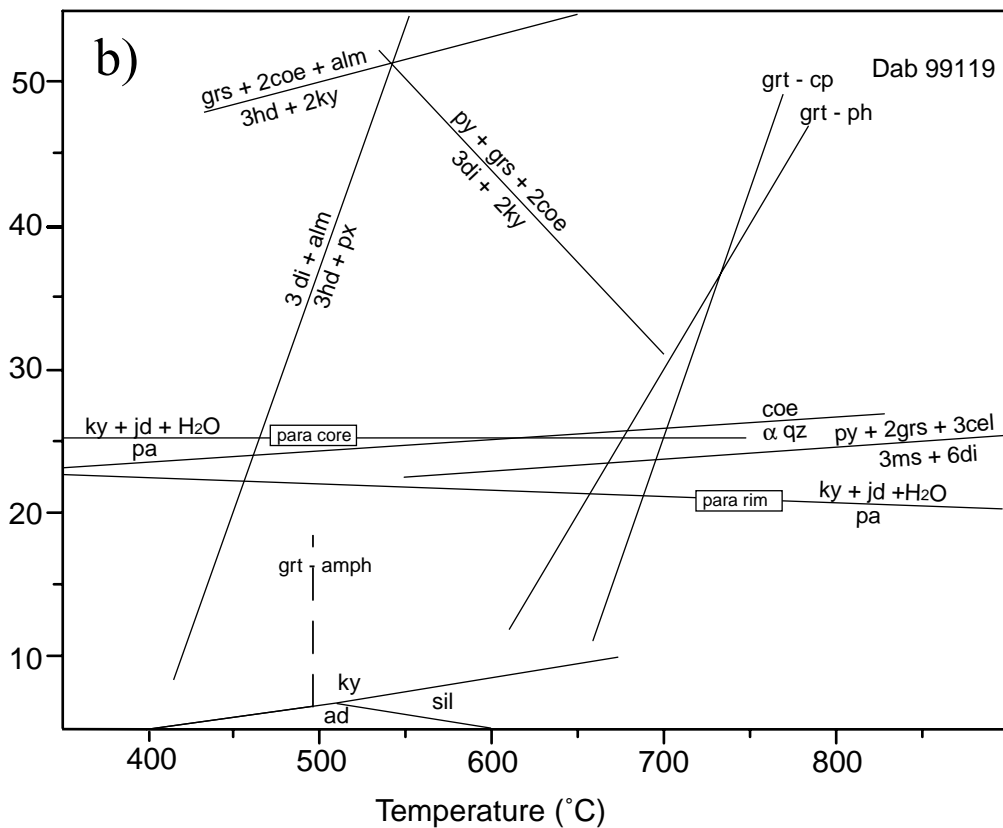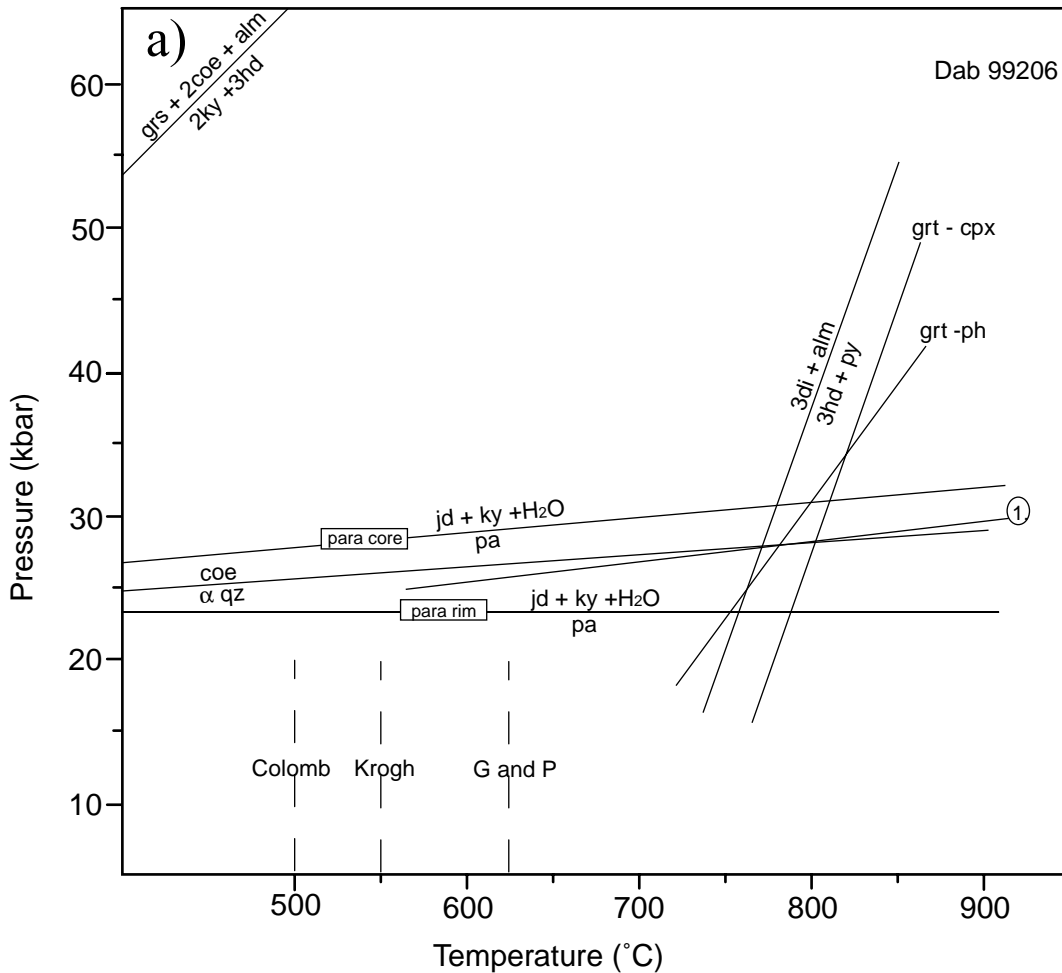
Figure 60: P-T diagram for eclogite samples from the Ganghe Unit, a) for sample Dab 99206 coesite stability is likely due to calculated equilibria (① stands for the reaction: 3ms+6di = py+2grs+3cel); b) eclogite sample Dab 99119 calculates a large spread in temperatures due to different methods used, however garnet-clinopyroxene and garnet-phengite temperatures show good agreement with other samples and stability of kyanite indicates UHP conditions, while other pressure sensitive reaction do not confirm coesite stability.
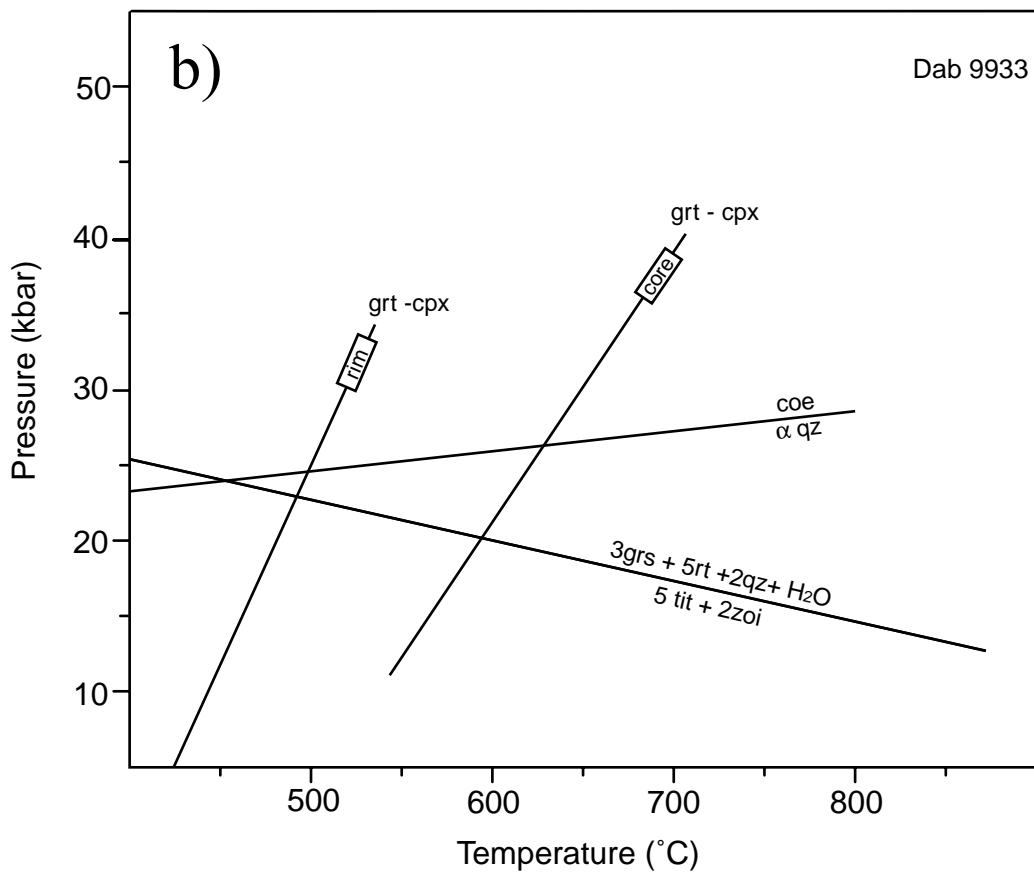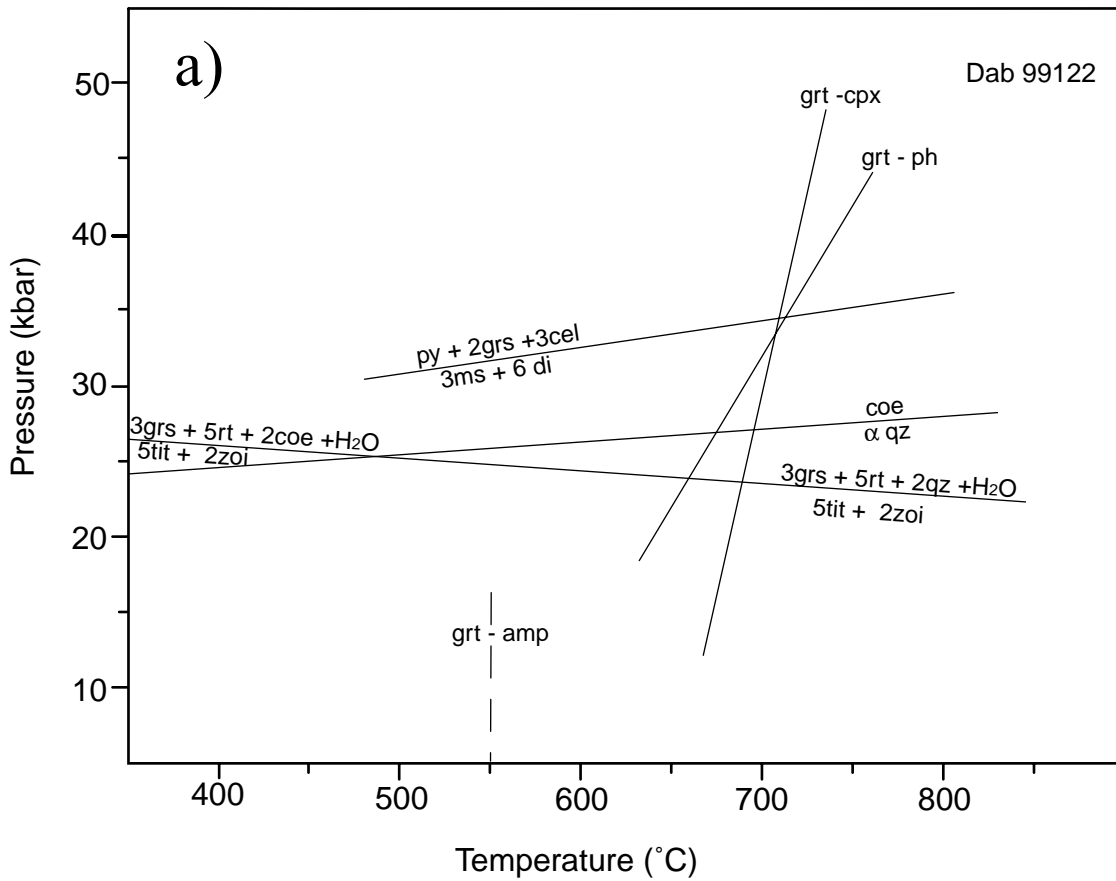
Figure 61: P-T diagram for a) eclogite sample Dab 99122, b) eclogite-facies basic dyke Dab 9933. While a) reveals clear record of the UHP event, for b) lack of critical mineral assemblages hampers detailed calculations. See also text for a discussion.
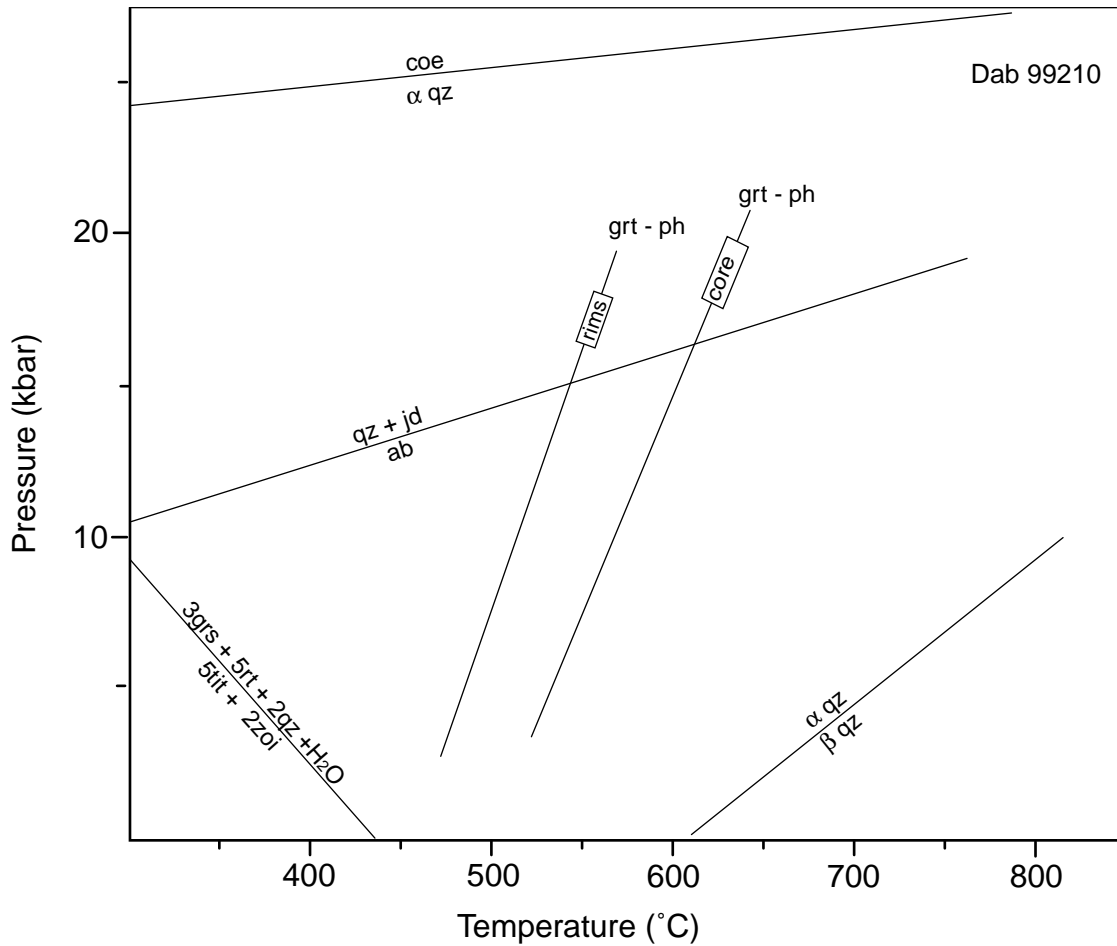
Figure 62: P-T diagram for minerals included in albite blasts of mylonite sample Dab 99210, bounding the Ganghe Unit. Temperatures calculated from core and rim analyses indicate retrogression and thus point to former presence of high-pressure minerals, however the absence of jadeite constraints the maximum pressure for the observed assemblage.

An estimate of potential UHP (or at least HP) conditions for the mylonite sample Dab 99210 is hampered by a lack of critical mineral assemblages. Garnet-phengite temperatures (cf. Fig. 62) indicate decreasing P-T conditions using core and rim analyses (core: 580°C at 10 kbar; rim: 500°C at 5 kbar). Due to the absence of K-feldspar the pressures have to be regarded as minimum estimates. The lack of jadeite in the presence of albite and quartz constrains the maximum pressure to 15 kbar at 600° C. The titanite- and zoisite- forming reaction in the absence of rutile also points to low grade conditions, recorded in the minerals.

Although only greenschist-facies conditions are documented for the mylonite, replacement of a HP-paragenesis is indicated by elevated (3.4) Si p.f.u. contents of phengite, and the presence of near-pure albite, garnet and titanite.

5. SUMMARY AND DISCUSSION

The UHP unit of the Dabie Shan is studied in this thesis by means of field-geology, reflection seismology, 2-D tomography, petrography, mineral chemistry as well as thermobarometry. Although some statements and conclusions are more qualitative rather than "founded in concrete" and supported by detailed data, there is a line of evidence which documents that the Dabie Shan is the metamorphic equivalent of the former passive margin of the Yangtze craton. This craton underwent rifting (probably in the Precambrian, e.g. Rowley et al. 1997; Romer unpubl. and pers. comm.), remained as a passive margin for some time and was then subducted as a (at least in part) coherent crustal segment to upper mantle depth, subsequently, likewise coherently, exhumed and finally overprinted by considerable Cretaceous to Cenozoic extensional tectonics (cf. Hacker et al. 2000; Ratschbacher et al. 2000). Thus classical field-geology combined with various techniques is a powerful method to study and decipher such deep-crustal processes.

An important argument for the coherent nature of the Dabie Shan arises from the geophysical data discussed here (cf. Schulze et al. 1998; Schmid et al. in review). A crustal segment of the eastern Dabie Shan was investigated by applying high-resolution reflection seismic and tomographic inversion techniques along a 20 km c. W-E traverse across UHP metamorphic and sedimentary rocks. Although such a short profile is potentially not fully representative for an orogen it provides a (so far) unique window to study UHP crust. This survey revealed that the crust exhibits three zones with different reflection patterns. The upper crustal zone (i) is c. 15 km thick and is more or less transparent with only few, largely subhorizontal reflectors. It is interpreted to trace a lithologically homogeneous crustal portion, consisting of UHP rocks thrusted on top of non-UHP crust. Both the hanging and footwall crustal segments lack larger portions of mafic rocks (i.e. oceanic crust). The relatively abrupt change in the reflection patterns from zone (i) to (ii) may correspond to the shear zone separating the UHP slab from the rocks below; a distinct "Master-thrust" contact was, however, not imaged. Future confirmation of such a "Master-thrust" would provide a reliable basis for recent exhumation models (cf. Hacker et al. 2000; Ratschbacher et al. 2000). In contrast to zone (i), the middle to lower crust (zone (ii) at 5-10 s TWT) is distinct both in number and geometry of reflectors. This zone is interpreted as cratonal basement, i.e. Yangtze crust, unaffected by the UHP metamorphism. The prominent and continuous subhorizontal

reflectors within zone (iii) at 10-12 s TWT (30-40 km) trace the Moho along the base of the crust. This evidences that a crustal root due to the UHP orogeny is not preserved and thus corroborates that the architecture of the Dabie Shan is dominated by Cretaceous to Cenozoic tectonics (Ratschbacher et al. 2000). This interpretation is in accord with results from differently located (low resolution) refraction profiles through Dabie, which also do not give an indication for a significantly elevated crustal thickness. Such a crustal root, likely present during the Triassic-Jurassic collision tectonics, was probably destroyed by Cretaceous, large-scale crustal extension and associated magmatism.

A shallow (< 700 m) tomographic velocity model elucidates the geology across the Tan Lu fault. The active fault dips steeply towards E; to the east of this major regional fault sediments and sedimentary rocks, dipping shallowly towards the fault, are imaged. The transition across the Tan Lu and towards the UHP gneisses is seen as a sharp increase in velocities and a changing geometry of isolines. Our tomographic model shows that the UHP unit is grossly homogeneous in velocities (variation below 10%), demonstrating that distinct and detectable (i.e. at the applied resolution) bodies of high-velocity rocks (eclogite or marble) do not occur along the profile line. This verifies field observations in the UHP unit, which indicate that gneisses represent the dominant lithology and eclogitic rocks are restricted to small scale enclosures. Observed velocity-variations in the western part of the line are interpreted to directly trace large scale ductile structures, i.e. folds, in the rocks. This test study shows that reflection seismics may help to explore the 3D geometry of the UHP slab, and that tomography has the potential to directly trace super-outcrop structures and distinct lithologies, due to its higher sensitivity compared to reflection or refraction seismic lines.

New insights into the field relations in the UHP unit are founded on Chinese mapping work (Tang et al. unpubl.), and indicate that the Dabie Shan is a former passive margin of the Yangtze craton. Two cover units are defined and documented: one of which formed during the initial rifting and is characterised by bi-modal volcanics and dominantly silici-clastic sediments, the other exhibits a stratigraphic contact to its basement and bears clastic-carbonatic and mafic volcanic rock, thus indicating a shallow basin as environment. Metabasites in both cover units as well as carbonatic and minor felsic (e.g. jadeite-"coesitites") rocks reveal P-T conditions compatible with UHP metamorphism, whereas the large majority of felsic rocks either re-equilibrated in the lower amphibolite- to greenschist-facies, or apparently did not respond to an elevation of P-T conditions.

The felsic basement contains mafic meta-plutons and dykes, both in (partly relict) UHP-facies, supporting the distinction of an older basement and overlying cover rocks. Whole rock geochemical data obtained from volcanic metabasites of the cover units (not presented here) point to alkaline to sub-alkaline within-plate-basalts with a mantle signature, thus likely rift-related. Furthermore, portions of gneissic eclogite are recognised to occur in the basement gneisses, giving further direct evidence that the basement experienced the UHP event as well (cf. Tabata et al. 1998; Carswell et al. 2000). A distinct record of the poly-phase deformation history and occurrence of a blasto-mylonite, bounding the Ganghe Unit to the basement of the Changpu Unit, suggests a different tectonic evolution for the two units during the UHP metamorphism. Recognisable basement-cover sequences, surviving UHP tectono-metamorphism, are a further argument for an exhumation model as proposed by Hacker et al. (2000).

Surprisingly, some of the discussed rocks, namely the felsic volcanics, apparently did not respond at all to changing P-T conditions. As pointed out above, the probable lack of a promoting fluid phase may be responsible for this "frozen" kinetics, thus meta-stability nearly an order of magnitude higher than documented from the Bergen Arcs, western Norway, (Austrheim 1987, 1998) seems possible for felsic lithologies, whereas mafic rocks obviously obey the rules of equilibrium thermodynamics (at least along the prograde segment(s) of metamorphic paths).

A major geodynamic consequence of coherent basement-cover sequences undergoing UHP metamorphism is that all quartz within the rocks which are subducted to corresponding depth is transformed into coesite. This high-pressure silica-polymorph has a molar volume ca. 11 vol.% less than quartz (cf. e.g. Matthes 1990). A reasonable assumption of ca. 30 modal % quartz present in the gneisses results in a volume decrease and thus density increase of ca. 3 % for the bulk of the subducted crust. This represents a minimum estimate since high-pressure rocks are in general denser than their protoliths. Thus formation of HP to UHP felsic gneisses contributes to the subduction forces, similar to "slab pull" of oceanic crust. Back-reaction to quartz reverse the volume loss and causes fracturing of the bulk of the crust during uplift, comparable to cracks observed around former coesite inclusions in refractory minerals.

This has a significant impact on the rheological behaviour and the buoyancy of the crust. Resulting grain size reduction enhances deformation and creates potential pathways for fluids, giving rise to penetrative recrystallisation of gneisses and thus to formation of retrograde hydrous minerals like amphibole or biotite. In contrast, mafic HP-UHP rocks are often well preserved or suffered only a small amount of retrogression. This might be

explained by i) less abundant quartz/coesite present (SiO_2 liberated during prograde metamorphism might dissolve in a fluid phase and be precipitated in metamorphic veins), ii) non-penetration by fluids due to their impermeability or iii) by unfavourable reaction kinetics after formation of a HP mineral assemblage. The latter is often evident from pristine eclogite with coesite inclusions, however one mineral which breaks down frequently in the presence of a fluid phase is Na-clinopyroxene (omphacite), whereas garnet, phengite, zoisite, zircon and rutile behave more as refractory minerals. From this and the above documented petrography a lithologically-controlled retrogression is obvious. Thus different lithologies record different segments of a tectono-metamorphic history. Consideration of such processes might solves the enigma of lower grade gneisses hosting UHP eclogites. Further such volume changes reduce the amount of overburden to be removed during uplift by erosion and/or normal faulting.

These observations and interpretations further argue strictly against a "foreign" origin of eclogite-facies rocks and strongly support an "in situ" generation (cf. Smith 1995, for a recent discussion).

Field-relationships and petrography already indicate a common UHP overprint in the three lithological units, however, a mineral chemistry study, combined with thermobarometry was undertaken in order to document the variations of considered phases and thus provide data-supported evidence for the UHP event in all lithologies. A total of twenty-four rock samples (mafic, felsic and carbonatic) were investigated for their petrography, mineral chemistry and preserved P-T information.

The detected chemical differences among the most widespread minerals in the studied rocks (garnet and omphacite) are likely to reflect chemically different protoliths and/or (especially for the metabasites of the Changpu Unit) different degrees of interaction with their carbonatic host-rocks, during their common tectono-metamorphic history.

Relics of UHP minerals in calc-silicate rocks, similar mineral chemistry in different eclogite-types, gneissic eclogite and carbonatic rocks as well as their field relations indicate that these rocks underwent the same metamorphic cycle, although texturally constrained P-T data are not yet available for marbles and calc-silicate rocks. According to microprobe data, Fe^{3+} contents in omphacite and phengite calculated by charge balance constraints are highly variable, which results in a great range of temperatures for the garnet-phengite and garnet-clinopyroxene thermometry. Wet chemical titration reveals elevated contents of about 40% Fe^{3+} of total iron for omphacite, which, however cannot take into account any zoning of Fe^{3+} in the minerals. Assuming a fixed Fe^{3+}/Fe_{tot} ratio for both, the omphacite and the phengite, P-

T calculations for single samples as well as for the whole suite of rocks produce meaningful P-T data. Thus, reliability of P-T data involving clinopyroxene with low Fe_{tot} contents should be examined critically.

Careful thermobarometric calculations using minerals in similar textural positions result in peak metamorphic P-T conditions in excess of 40 kbar and 700°C, whereas retrograde mineral assemblages point to continuously decreasing pressures and temperatures down to <20 kbar and <600°C. These new results imply that subduction of continental rocks in the Dabie Shan was deeper than previously assumed and that cooling already took place during the initial exhumation of the UHP rocks in upper mantle depth. In particular, the shape of the retrograde P-T path has to be taken into account for future geodynamic and thermal modelling of the rocks from Dabie Shan.

Peak metamorphic pressures presented here (i.e. 40-48 kbar/ <750°C) are considerably higher than previously reported for any of the Dabie Shan eclogite (e.g. Okay 1993, Tabata et al. 1998a, 1998b, Carswell et al. 1997, 2000). Although there is an inconsistency in the maximum pressures recorded in the different samples studied here, most importantly they are compatible with UHP metamorphism in the three defined lithological units. In this connection it is interesting that the sample with the most calcic garnet (Dab 9712) yielded pressures in general ca. 5-6 kbar higher than those with less grossular, thus it can not be excluded that a high grossular component (X_{Ca} >0.5) produces somewhat overestimated pressures. However, up until now this effect is not studied experimentally and therefore awaits clarification in the future. Furthermore, it can not be excluded that some of the samples (not only the felsic volcanics) failed to equilibrate at the P and/or T peak of metamorphism due to kinetic reasons or suffered some degree of modification of their peak-compositions in the course of uplift and retrogression. Further, although the mineral chemistry was studied as systematically as accessible, true peak compositions may have been overlooked or simply not measured in the "best" grains/samples (it took some time to recognise coesite in the Dora Maira rocks). Anyhow, involvement of more Fe- and Mg-rich garnet (e.g. Dab 9854 and 9872, respectively) and omphacite with distinct Jd-contents (~60 and ~25, respectively) results in pressures, corresponding at least to the occurrences and stability of coesite and even possible diamond (cf. Xu et al. 1992, Tabata et al. 1998a). Thus irregular compositional effects on the used barometer (Waters and Martin 1993) appear less serious than once thought.

Similar pressures for crustal UHP rocks have so far only been reported from the diamond-bearing rocks from the Kokchetav massif (e.g. Shatsky et al. 1995). Importantly, experimental results indicate that phengite is stable at such conditions (Domanik and

Holloway 1996) and melting would have been restricted to water-saturated MORB (Schmidt and Poli 1998). It has to be mentioned, however, that the determined pressures are outside the calibrated range of the barometer (40 kbar, 900°C, Si p.f.u. >3.5) but the possible error due to extrapolation is considered as small and the calibration itself has an error of ± 2.5 kbar (Waters and Martin 1993, and pers. comm.). Definitely, the chosen activity model for garnet and omphacite has a major influence, resulting in differences of up to 10 kbar (e.g. using ideal mixing in garnet), but the application of the activity models of Newton and Haselton (1981) for garnets and Holland (1990) for omphacites is at least conformable with the barometric expression. Use of fixed Fe^{3+} contents for omphacite and phengite resulted in similar P-T estimates for the garnet-clinopyroxene and garnet-phengite geothermometer within the error of the calibrations (grt-omph ±30°C; grt-phe ±50°C). Temperature calculations, which solely base on charge balance constraints, gave rather variable and in part unreasonable values of >1000°C. Thus a critical evaluation of the ferric iron, especially in Fe-poor minerals, is crucial to document reliability of P-T estimates for HP and UHP rocks.

Most garnet porphyroblasts reveal diffusion-controlled zonation patterns with distinct retrograde rims, which should be expected at such high temperatures. It is, however, quite remarkable that one garnet porphyroblast (Dab 9854) still preserved its compositional growth zoning, which may be caused by accelerated rates of subduction and exhumation or is an expression of locally unfavourable kinetics. One major problem concerning the P-T estimates of high grade metamorphic rocks bearing garnet with diffusion-controlled zoning is the uncertainty about the equilibrium compositions and the relative timing of the thermal equilibrium(-a) (recently discussed for UHP eclogites in Nowlan et al. 2000). The flat zonation pattern in the core of most of the garnets likely represents the temperature peak already below the "truly attained pressure peak" during the metamorphic evolution. However, the preservation of a compositional prograde growth zoning in one garnet porphyroblast and the P-T estimate for this sample (Dab 9854, cf. Table A5), which is quite close to the other results, seems to exclude large uncertainties. Furthermore, the distinctly different diffusion rates of the minerals used for thermobarometry may result in erroneous P-T conditions. Minerals may well (in part) equilibrate along the retrograde path or may be affected by fluid-enhanced decomposition. This is particularly critical for UHP phengite, which may be affected by exsolutions of talc and quartz as described by Ferraris et al. (2000). Such exsolution features may lead to analytical errors resulting in a considerable overestimation of Si and a deficiency of A-site cations, thus yielding erroneous pressures. Such patterns may be present in high-Si phengite (cf. Fig. 44), however, the described core-rim systematics of

phengite, lack of petrographic evidence, and the garnet-phengite temperatures compared to the garnet-omphacite ones, argues against the presence of such exsolutions in the studied samples.

With the application of the same barometer to samples from Dabie Shan, Carswell et al. (1997) could distinguish between HP and UHP-eclogites, although lower pressures were presented; in the Western Gneiss Region of Norway the used barometer also yields pressures consistent with coesite occurrence and thus reliable UHP conditions (Wain 1997).

Another constraint towards the exhumation path of the investigated UHP rocks is the fact that no granulite-facies assemblages were observed. In the Su Lu region, however, such an overprint is reported (cf. Wallis et al. 1999; Banno et al. 2000), whereas it is lacking in the Dora Maira (Chopin 1984, Schreyer 1995) This limits the temperatures to less than ca. 800 °C for the whole metamorphic path of the Dabie. Furthermore the occurrence and stability of prograde talc together with garnet in samples from the Bixiling body (not shown and discussed here; cf. Liou and Zhang 1995) point in the same direction. This and the P-T estimates presented here implies that the UHP slab cooled during its exhumation, as predicted by models of e.g. Peacock et al. (1995).

It is further worth considering the initial temperature of continental crust undergoing HP-UHP metamorphism. In general upper crust can be considered as cold, i.e. <100 °C/1kbar, whereas the lower crust of a stable craton (like the Yangtze) should be in the order of about 300-400 °C/10 kbar (comparable to the present Scandinavian shield, cf. e.g. Press and Siever 1985). Thus upper and lower portions of an "intact" crustal section (30-40 km thick) subjected to UHP conditions would likely behave differently, depending on the initial temperature. If such a "hypothetical" crust remains "intact" during subduction, the lower crust would be faster heated by the elevated temperature of the surrounding mantle, because isotherms are only deeply dragged down in the upper part of a subducted slab, thus the initial "temperature gap" is broadly conserved, whereas the initial "pressure gap" disappears as soon as the "subduction tip" becomes ± horizontal. Therefore, lower crust at UHP conditions during subduction is expected to reach temperatures of >1000 °C, while upper crust remains below ca. 800 °C (as seen in UHP rocks). In such a case lower crustal rocks would likely either melt or (probably earlier) jam the subduction zone due to buoyancy when the thicker continental lithosphere enters the subduction zone. This may account for the enigma that "true" (not tectonically transported to upper levels prior to UHP) lower crustal rocks with history of UHP metamorphism haven't been found yet (to the authors knowledge). Alternatively, the upper crust may detach and rise back to the surface, while the lower crust remains and may melt

later. In contrast, a thinned (rifted) continental margin is expected to be dragged down the subduction channel by the oceanic plate and probably refrigerated by underplating of other, cold, slabs (e.g. Platt 1986, 1993; Ernst and Peacock 1996). The latter case is postulated to hold true for the Dabie Shan. The above drafted scenario of a rift within the Yangtze craton, subsequent development as a passive margin followed by (obvious) attempted subduction to depths of ca. 120-150 km (40-48 kbar/<750 °C) can be explained by the above processes. However, this requires a very broad passive margin, since Hacker et al. (2000) estimated the down-dip length of the slab to be 125-200 km. Considerable thinning, thus elongation, due to deformation is so far only documented during exhumation. It is only speculated here that arrival of the "thicker", "true cratonal" portion of the Yangtze, represents the continental collision, what may have caused a subduction jam and thus reduced the "downward forces" allowing buoyancy forces to take over and trigger the exhumation of the UHP slab.

6. REFERENCES

Ames, L., Tilton, G.,R., Zhou, G. 1993. Timing of collision of the Sino-Korean and the Yangtze cratons: U-Pb zircon dating of coesite-bearing eclogites. *Geology,* **21**, 339-342

Anhui Institute of Regional Geological Survey (AIRGS). (unpublished). 1: 250,000, Geological Map of Dabie Mountains Area of Anhui Province.

Austrheim, H. 1987. Eclogitisation of lower crustal granulites by fluid migration through shear zones. *Earth Planet Sci Lett*, **81**, 221-232.

Austrheim, H. 1998. Influence of fluid and deformation on metamorphism of the deep crust and consequences for the geodynamics of collision zones. *In: Hacker BR, Liou JG (eds.) When continents collide: geodynamics and geochemistry of ultrahigh-pressure rocks*. Kluwer Academic Publishers. Dordrecht, Netherlands, 297-323.

Banno, S., Enami, M., Hirajima, T., Ishiwatari, A., Wang, Q.C. 2000. Decompression P-T path of coesite eclogite to granulite from Weihai, eastern China. *Lithos*, **52**, 97-108.

Berman, R.G. 1979. Thermal properties. *The properties of diamond*. London, Academic press, 4-22.

Berman, R.G. 1991. Thermobarometry using multiequilibrium calculations: a new technique with petrologic applications. *Can. Mineral.*, **29**, 833-855.

Bohlen, S.R., Boettcher, A.L. 1982. The quartz-coesite transformation: a pressure determination and the effects of other components. *J. Geophys. Res.*, **87**, 7073-7078.

Bundy, F.R. 1980. The P, T phase and reaction diagrams for elemental carbon. *J. Geophys. Res.*, **87**, 7073-7078.

Carswell DA 1990. Eclogites and the eclogite facies. *In: Carswell DA (ed.) Eclogite facies rocks*. Blackie, Glasgow, London, 1-13.

Carswell, D.A. 2000. Preface - Ultra-high-pressure metamorphic rocks. *Lithos*, **52**, ix-xii.

Carswell, D.A., O´Brien, P.J., Wilson, R.N., Zhai, M. 1997. Thermobarometry of phengite bearing eclogites in the Dabie Mountains of central China. *J. metamorphic Geol.*, **15**, 239-252.

Carswell, D.A., Wilson, R.N. and Zhai, M. 2000. Metamorphic evolution, mineral chemistry and thermobarometry of schists and orthogneisses hosting ultra-high pressure eclogites in the Dabieshan of Central China. *Lithos* **52**, 121-155.

Carswell, D.A., Zhang, R.Y. 1999. Petrographic and Metamorphic Evolution of Ultrahigh-Pressure Eclogites in Plate-Collision Belts. *Intern. Geol. Rev.*, **41**, 781-798.

Chatterjee, N., D. 1991. Applied mineralogical thermodynamics. Berlin, Springer.

Chavagnac, V., Jahn, B.-M. 1996. Coesite-bearing eclogites from the Bixiling Complex, Dabie Mountains, China: Sm-Nd ages, geological characteristics and tectonic implications. *Chemical Geology*, **133**, 29-51.

Chemenda, A.I., Mattauer, M., Malavieille, J, Bokun, A.N., 1995. A mechanism for syn- collisional rock exhumation and associated normal faulting: Results from physical modelling. *Earth Planet. Sci. Lett*., **132**, 225-232.

Chopin, C. 1984. Coesite and pure pyrope in high-grade blueschists of the western Alps: A first record and some consequences. Contrib. *Mineral. Petrol.*, **86**, 107-118.

Coleman, R.G. and Wang, X. 1995. Ultrahigh Pressure Metamorphism. Cambridge Univ. Press.

Domanik, K.J, Holloway, R. 1996. The stability and composition of phengitic muscovite and associated phases from 5.5 to 11 Gpa: Implications for deeply subducted sediments *Geochimica et Geochosmochimica Acta*, **60**,

No. 21, 4133-4150.

Dong, S., Wu, X., Gao, R., Lu, D., Li, Y., He, Y., Tang, J., Cao, F., Hou, M., Huang, D.,1996. Preliminary study on deep geology of Dabie orogenic belt. *Continental Dynamics*, **1**,103-108.

Dong, S., Wang, X., Huang, D. 1997. Discovery of low grade metamorphic volcanic rock sheets within UHP in Dabie Mts., and its implications. *Chinese Sci. Bull.*, **41**, 815-820. (in Chinese).

Droop, G.T.R. 1987. A general equation for estimating Fe^{3+} concentrations in ferromagnesian silicates and oxides from microprobe analyses, using stoichiometric criteria. *Mineral. Mag*. **51**, 431-435.

Eide, E.A., 1995. A Model for the Tectonic History of HP and UHPM Regions in East Central China. *In: Coleman, R.G., Wang, X. (Eds.) Ultrahigh Pressure Metamorphism*. Cambridge University Press. Cambridge. 391-426.

Enkin, R.J., Yang, Z., Chen, Y, Courtillot, V. 1992. Paleomagnetic constraints on the geodynamic history of major blocks of China from Permian to Present. *J. Geophys. Res.*, **97**, 13,953-13,989.

Ernst, W.G. 1973. Blueschist metamorphism and P-T regimes in active subduction zones. *Tectonophysics*, **17**, 255-272.

Ernst, W.G. 1976: Petrologic phase equilibria. W.H. Freeman, New York. 333pp.

Ernst, W.G., Peacock, S.M. 1996: A thermotectonic model for preservation of ultrahigh-pressure phases in metamorphosed continental crust. *In: Subduction: Top to Bottom*. Geophysical monograph of the AGU. 171-178.

Ferraris, C., Chopin, C. and Wessicken, R. 2000. Nano to microscale decompression products in ultrahigh-pressure phengite: HRTEM and AEM study, and some petrological implications. *American Mineralogist,* **85** (9), 1195-1201.

Franz, L., Romer, R., Klemd, R., Schmid, R., Oberhänsli, R., Wagner, T., Dong, S. 2001. Formation of High-Pressure quartz veins within eclogite of the Southern Dabie Shan (Central China): P-T-t-d-x conditions and fluid flow during exhumation of eclogite facies rocks. *Contr. Mineral. Petrol*. In press.

Gao, S., Jin, Z., Jin, S., Kern, H., Popp, T., 1998. Seismic velocity structure and composition of continental crust in the Dabie-Sulu Area. *Continental Dynamics,* **3**, 108-112.

Gilder, S., Courtillot, V., 1997. Timing of the North-South China collision from new middle to late Mesozoic paleomagnetic data from the North China Block. *J. Geophys. Res.*, **102**, 17713-17727.

Graham, C.M. and Powell, R., 1986. A garnet-hornblende geothermometer: calibration, testing, and application to the Pelona schists, southern California. *J. metamorphic Geol.*, **2**, 13-31.

Green, D. H. and Hellman, P. L., 1982. Fe-Mg partitioning between coexisting garnet and phengite at high pressures, and comments on a garnet-phengite geothermometer. *Lithos*, **15**, 253-266.

Hacker, B.R. and Liou, J.G. 1998. When Continents Collide: geodynamics and Geochemistry of Ultrahigh Pressure Rocks. Kluwer Academic Publishers, Dordrecht.

Hacker, B.R., Ratschbacher, L., Webb, L., Ireland, T., Walker, D. and Dong, S., 1998: U/Pb zircon ages constrain the architecture of the ultrahigh-pressure Qinling-Dabie Orogen, China. *Earth and Planetary Science Letters,* **161**, 215-230, 1998.

Hacker, B.R., Ratschbacher, L., Webb, L.E., McWilliams, M., Ireland, T., Dong, S., Calvert, A., Wenk, H.-R. 2000. Exhumation of the ultrahigh-pressure continental crust in east-central China: Late Triassic Early Jurassic extension. *Journal Geophysical Research* **105**: 13,339-13,364.

Hacker, B.R., Wang, X, Eide, E.A., Ratschbacher, L. 1996. Qinling-Dabie ultrahigh-pressure collisional orogen: A critical review of existing data and suggestions for future research. *In: Yin, A. and Harrison, T.M.*

(eds.) *The Tectonic Evolution of Asia.* Cambridge Univ. Press, 345-370.

Harley, S.L., Carswell, D.A., 1995. Ultradeep crustal metamorphism: A prospective view. J. Geophys. Res., B5, **100**, 8367-8380.

Hodges, K.V., Spear, F.S. 1982. Geothermometry, geobarometry and the Al2SiO5 triple point at Mt. Moosilauke, New Hampshire. *Am. Mineral.*, **67**, 1118-1134.

Holland, T..J.B. 1980. The reaction albite = jadeite + quartz determined experimentally in the range of 600 - 1200°C. *Amer. Mineral.*, **65**, 129-134.

Holland, T.J.B. 1990. Activities of components in omphacite solid solutions - An application of Landau theory to mixtures. *Contributions to Mineralogy and Petrology* **105**, 446-453.

Jahn, B., Wu, F., Lo, Ch-H., Tsai, Ch-H. Crust-mantle interaction induced by deep subduction of the continental crust: geochemical and Sr-Nd isotopic evidence from post-collisional mafic-ultramafic intrusions of the northern Dabie complex, central China. *Chemical Geology*, **157**, 119-146.

Kern, H., Gao, S., Jin, Z., Popp, T., Jin, S. 1998. Petrophysical studies on rocks from the Dabie ultrahigh-pressure (UHP) metamorphic belt, Central China: implications for the composition and delamination of the lower crust. *Tectonophysics*. **301**, 191-215.

Kern, H., Gao, S., Jin, Z., Popp, T., Jin, S., 1998a. Petrophysical studies on rocks from the Dabie ultrahigh pressure (UHP) metamorphic belt, Central China: implications for the composition and delamination of the lower crust. *Tectonophysics*, **301**, 191-215.

Kern, H., Popp, T., Gao, S., Jin, Z., 1998b. P- and S-wave velocities and densities of rocks from the Dabie ultrahigh-pressure (UHP) metamorphic belt to pressures of 600 MPa and to temperatures of 600 °C. *Continental Dynamics,* **3**, 96-102.

Krogh, E.J.. 2000. The garnet-clinopyroxene Fe^{2+} - Mg geothermometer: an updated calibration. *Journal of Metamorphic Geology,* **18**, 211-219.

Krogh, E.K. 2000b. Distribution of Fe2+ and Mg between coexisting garnet and hornblende in synthetic and natural systems: an empirical calibration of the garnet-hornblende Fe-Mg geothermometer. *Lithos*, **53**, 265-277.

Kröner, A., Zhang, G.W., Sun, Y. 1993. Granulites in the Tongbai area, Qinling belt, China: Geochemistry, petrology, single zircon geochronology, and implications for the tectonic evolution of eastern Asia. *Tectonics*, **12**, 245-255.

Lardeaux, J.-M. 1998. Discovery of ultra-high pressure metamorphism in the axial zone of the Variscan belt (French Massif Central): exhumation processes and geodynamic consequences. *Acta Universitatis Carolinae - Geologica*, **42**, 294-5.

Lardeaux, J.-M., Ledru, P., Daniel, I. 1999. Exhumation of the Palaeozoic coesite-bearing eclogites from the eastern Massif Central. EUG 10, Journal of Conference Abstracts, 86.

Leake, B.W., Wooley, A.R., Arps, C.E.S., Birch, W.D., Gilbert, M.C., Grice, J.D., Hawthorne, F.C., Kato, A., Kisch, H.J., Krivovichev, V.G., Linthout,K., Laird, J., Mandarino, J., Maresch, W.V., Nickel, E.H., Rock, N.M.S., Schumacher, J.C., Smith, D.C., Stephenson, N.C.N., Ungaretti, L., Whittaker,E.J.W., and Youzhi, G. 1997. Nomenclature of amphiboles. Report of the subcommittee on amphiboles of the International Mineralogical Association Commission on new minerals and mineral names. *European Journal of Mineralogy* **9**, 623-65.

Liou, J.G., Zhang, R.Y. 1995. Significance of ultrahigh-P talc-bearing eclogitic assemblages. *Am. Mineral*. **59**, 93-102.

Liou, J.G., Zhang, R.Y., Eide, E.A., Maruyama, S., Wang, X. and Ernst, W.G. 1996. Metamorphism and tectonics of high-P and ultrahigh-P belts in Dabie-Sulu Regions, eastern China. *In*: *Yin, A. and Harrison, T.M.* (eds.):*The Tectonic Evolution of Asia*, 300-343, Cambridge Univ. Press.

Mattauer, M., Matte, P., Malavieille, J., Tapponier, P., Maluski, H., Xu, Q., Lun, L. and Tang, Q. 1985. Tectonics of the Qinling belt: Build-up and evolution of eastern Asia. *Nature*, **317**, 496-500.

Matthes, S. 1990. Mineralogie. Springer. third ed.. 448pp.

Mirwald, P.W. and Massonne, H.-J. 1980. The low-high quartz and quartz-coesite transition to 4GP between 600 and 1600 °C and some reconnaissance data on the effect of NaAlO2 component on the low quartz coesite transition. J. Geophys. Res., **85**, 6983-6990.

Morimoto, M. 1988. Nomenclature of Pyroxenes. *Mineralogical Magazine,* **52**, 535-550.

Newton, R.C., Haselton, H.T. 1981. Thermodynamics of the garnet-plagioclase-Al_2SiO_5-quartz geobarometer. *In*: Newton, R.C. (ed.): *Thermodynamics of minerals and melts*. Springer Verlag, New York, 131-147.

Nowlan, E.U., Schertl, H.-P. and Schreyer, W. 2000. Garnet-omphacite-phengite thermobarometry of Eclogites from the coesite-bearing unit of the southern Dora-Maira Massif, Western Alps. *Lithos,* **52**, 197-214.

Oberhänsli, R., Franz, L., Schmid, R., Ryberg, T., Schulze, A., Ratschbacher, L., Hacker, B.R. (1998). Seismic highlights Structure of the Dabie Ultrahigh-Pressure Orogen of China. EOS Transactions, AGU Fall Meeting 1998, 79, No. 45, p. F795.

O´Brien, P.J., Zotov, N, Law, R., Ahmed Khan, M., Qasim Jan, M. (2001). Coesite in Himalayan eclogite and implications for models of India-Asia collision. *Geology* (in press).

Okay, A.I. 1993. Petrology of a diamond and coesite bearing metamorphic terrain: Dabie Shan, China. *European Journal of Mineralogy*, **5**, 659-67.

Okay, A.I., Shutong, X. and Sengör, A.M. 1989. Coesite from the Dabie Shan eclogites, central China. *European Journal of Mineralogy*, **1**, 595-598.

Omori, S., Liou, J.G., Zhang, R.Y., Ogasawara, Y. 1998. Petrogenesis of impure dolomitic marble from the Dabie Mountains, central China. *Island Arc*, **7**, 98-114.

Parkinson, C.D. 2000. Coesite inclusions and prograde compositional zonation of garnet in whiteschist of the HP-UHPM Kokchetav massif, Kazakhstan: a record of progressive UHP metamorphism. *Lithos,* **52**, 215-233.

Peacock, S.M., Rushmer, T., Thompson, A.B. 1995. Partial melting of subducting oceanic crust. *Earth Planet. Sci. Let.*, **121**, 227-244.

Peltzer, G., Tapponier, P., Zhang, Z.T., Xu, Z.Q. 1985. Neogene and Quaternary faulting in along the Qinling Shan. *Nature*, **317**, 500-505.

Platt, J.P. 1986. Dynamics of orogenic wedges and the uplift of high-pressure metamorphic rocks. *Geol. Soc. America Bull.*, **97**, 1037-1053.

Platt, J.P. 1993. Exhumation of high-pressure rocks: a review of concepts and processes. *Terra Nova*, **5**, 133-199.

Powell, R., 1985. Regression diagnostics and robust regression in geothermometer/geobarometer calibration: the garnet-clinopyroxene geothermometer revisited. *J. metamorphic Geol.,* **3**, 327-342.

Press, F., Siever, R. 1986. Earth. W.H. Freeman and Company, New York.

Ratschbacher, L., Hacker, B.R., Webb, L.E., McWilliams, M., Ireland, T., Dong, S., Calvert, A., Wenk, H.-R. 2000. Exhumation of the ultrahigh-pressure continental crust in east-central China: Cretaceous and Cenozoic unroofing and the Tan-Lu fault. *Journal Geophysical Research* **105**: 13,303 13,338.

Reischmann, T., Kröner, A., Sun, Y., Yu, Z., Zhang, G. 1990. Opening and closure of an early Paleozoic ocean in the Qinling belt, China. *Terra Abstracts*, **2**, 55-56

Rowley, D. B., Xue, F., Tucker, R. D., Peng, Z. X., Baker, J. and Davis, A. 1997. Ages of ultrahigh pressure metamorphism and protolith orthogneisses from the eastern Dabie Shan: U/Pb zircon geochronology. *Earth Planet. Science* Letters, **151**, 191-203.

Schertl H.P. and Okay, A.I. 1994. A coesite inclusion in dolomite in Dabie Shan, China: Petrological and rheological significance. *European Journal of Mineralogy* **6**, 995-1000.

Schliestedt, M. 1980. Phasengleichgewichte in Hochdruckgesteinen von Sifnos, Griechenland. PhD thesis, TU Braunschweig, 142 pp.

Schmid, J.C., Ratschbacher, L., Hacker, B.R., Gaitzsch, I., Dong, S., 1999. How did the foreland react? Yangtze foreland fold-and-thrust belt deformation related to exhumation of the Dabie Shan ultrahigh-pressure continental crust (eastern China). *Terra Nova*, **11**, 266-272.

Schmid, R., Franz, L., Oberhänsli, R., Dong, S., 2000b. High Si-phengite, Mineral Chemistry and P-T Evolution of Ultra-High-Pressure Eclogites and Calc-Silicates from the Dabie Shan, eastern PR China. *Geological Journal*, **35** (3-4), 185-207.

Schmid, R., Oberhänsli, R., Franz, L., Klemd, R., Ratschbacher, L. (1999). Metamorphic Evolution of the UHPM Marble-Eclogite Association in the Dabie Shan, E-China, Abstract-Volume Metam. Studies Group Meeting 1999. Exhumation of Metamorphic Terrans; Rennes (France). p. 68.

Schmid, R., Oberhänsli, R., Martinotti, G., Franz, L., Liu, X. and Dong, S. (2000a). Basement-Cover Sequences within the UHP unit of the Dabie Shan, E-China. *Eur. J. Mineral. 12, Beihefte 1*, 2000, 183.

Schmid, R., Ryberg, T., Ratschbacher, L., Schulze, A., Franz, L., Oberhänsli, R., Dong. S. (2001). Crustal structure of the eastern Dabie Shan interpreted from deep reflection and shallow tomographic data. *Tectonophysics* (in press).

Schmidt, M.W, Poli S. 1998. Experimentally based water budgets for dehydrating slabs and consequences for arc magma generation. *Earth and Planetary Science Letters* **163**, 361-379.

Schreyer, W., 1995. Ultrahigh-pressure metamorphism- the retrospective view. *J. Geophys. Res.* **100**, B5, 8353-8366.

Schulze, A., Jiang, M., Ryberg, T., Gao, R., 1998. Survey yields data on unique metamorphic rock complex in China. *EOS, Transactions, Am. Geophys. Union* **79**, 36, 429-433.

Shatsky, V.S., Sobolev, V.S., Vavilov, M.A. 1995. Diamond-bearing metamorphic rocks of the Kokchetav massif (Northern Kazakhstan), *In: Coleman RG, Wang X. (eds.). Ultrahigh Pressure Metamorphism. Cambridge University Press: Cambridge.*

Smith, D.C., 1984. Coesite in clinopyroxene in the Caledonides and its implications for geodynamics. *Nature* **310**, 641-644.

Smith, D.C. 1995. Microcoesite and microdiamonds in Norway: An overview. *In: R. Coleman and X. Wang (eds.) Ultrahigh Pressure Metamorphism*. Cambridge University Press. Cambridge. 299-355.

Sobolev, N.V. and Shatsky, V.S. 1990. Diamond inclusions in garnets from metamorphic rocks: A new environment for diamond formation. *Nature*, **343**, 742-746.

Tabata, H., Maruyama, S. and Shi, Z. 1998b. Metamorphic zoning and thermal structure of the Dabie ultrahigh/high-pressure terrain, central China. *Island Arc*, **7**, 142-158.

Tabata, H., Yamauchi, K., Maruyama, S. and Liou, J.G. 1998a. Tracing the extend of a UHP metamorphic

terrane: mineral-inclusion study of zircons in gneisses from the Dabie Shan. *In: Hacker, B.R. and Liou, J.G. (eds.) When Continents Collide: geodynamics and Geochemistry of Ultrahigh-Pressure Rocks.* 261-273, Kluwer Academic Publishers, Dordrecht.

Tang, J., Qian, C., Gao, T. 1995. Discovery of low-grade metamorphic volcanic-detrital rock association in eclogite belt in the Dabie Mountains and its geological significance. *Geology of Anhui*, **5**, 29-35. (in Chinese with English abstract).

Tang, J., Qian, C., Jia, S., Gao, T., Lu, X., Lu, S., Yang, S. (unpublished). 1:10,000 Geological map of Changpu Area, Yuexi County, Anhui Province.

Tsai, C.-H-, Liou, J.G. 2000. Eclogite-facies relics and inferred ultrahigh-pressure metamorphism in the North Dabie Complex, central-eastern China. *Am. Mineral.*, **85**, 1-8.

Wain, A. 1997. 1997. New evidence for coesite in eclogite and gneisses: defining an ultrahigh-pressure province in the Western Gneiss Region of Norway. *Geology*, **25**, 927-930.

Wallis, S., Enami, M. and Banno, S., 1999. The Sulu UHP Terrane: A review of the petrology and structural geology. *International Geology Review*, **41**, 906-920.

Wang, C-Y., Zeng, R-S., Mooney, W.D., Hacker, B.R., 2000. A crustal model of the ultrahigh-pressure Dabie Shan orogenic belt, China, derived from deep seismic refraction profiling. *J. Geophys. Res.*, **105**, 10,857-10,869.

Wang, X. and Liou, J. G. 1991. Regional Ultrahigh-Pressure coesite-bearing eclogitic terrane in central China: evidence from country rocks, gneiss, marble and metapelite. *Geology* **19**, 933-936.

Wang, X. and Liou, J.G. 1993. Ultra-high-pressure metamorphism of carbonate rocks in the Dabie Mountains, central China. *Journal of Metamorphic Geology* **11**, 575-588.

Wang, X., Liou, J.G., 1991. Regional ultrahigh-pressure coesite-bearing eclogitic terrane in central China: Evidence from country rocks, gneiss, marble and metapelite. *Geology*, **19**, 933-936.

Wang, X., Liou, J.G., Mao, H.K. 1989. Discovery of Coesite in the Dabie Mountains, central China-indication of ultra-high pressure metamorphism. *GSA Abstracts with programs*, No. 32345.

Waters, D.J. and Martin, H.N. 1993. Geobarometry of phengite-bearing eclogites. *Terra Abstracts* **5**, 410-411. (updated calibration of 1996 at: http://www.earth.ox.ac.uk/~davewa/ecbar.html).

Webb, L.E., Hacker, B.R., Ratschbacher, L., Mc Williams, M.O., Dong, S. 1999. Thermochronologic constraints on deformation and cooling history of high- and ultrahigh-pressure rocks in the Qinling Dabie orogen, eastern China. *Tectonics*, **18**, 621-638.

Xiao YL, Hoefs J, van den Kerkhof AM, Fiebig J, Zheng Y. 2000. Fluid history of UHP metamorphism in Dabie Shan, China: a fluid inclusion and oxygen isotope study on the coesite-bearing eclogite from Bixiling. *Contrib. Mineral Petrol* **139**: 1-16

Xu, S., Okay, A.I., Sengör, A.M.C., Su, W., Liu, Y. and Jiang, L. 1992. Diamond from Dabie Shan metamorphic rocks and its implication for tectonic setting. *Science* **256**, 80-82.

Xue, F., Rowley, D.B., Baker, J. 1996. Refolded syn-ultrahigh-pressure thrust sheets in the south Dabie complex, China: Field evidence and tectonic implications. *Geology*, **34**, 455-458.

Yang, W., Chen, Z., 1998. Crustal structure and development of the Dabie UHPM terrane in eastern central China. *Continental Dynamics,* **3**, 86-95.

Yin, A. and Nie, S., 1993. An indentation model for the North and South China collision and the development of the Tan Lu and Honam fault systems, eastern Asia. *Tectonics*, **12**, 801-813.

You Z, Han Y, Yang W, Zhang Z, Wie B, Liu R. 1996. The high-pressure and ultra-high-pressure

metamorphic belt in the East Qinling and Dabie Mountains, China. China University of Geoscience Press, Wuhan, 150 pp

Zhang, Y.Q., Vergely, P., Mercier, J.L., 1995. Active faulting in and along the Qinling Range (China) inferred from SPOT imagery analysis and extrusion tectonics of southern China. *Tectonophysics,* **243**, 69-95.

Zhao, X., and Coe, R.S., 1987. Palaeomagnetic constraints on the collision and rotation of North and South China. *Nature*, **327**, 141-144.

III. APPENDIX

Table A1: Observed mineral assemblages of samples from the basement.

sample # rock type	mineral garnet	omph	rutile	phe	coesite	kyanite	zircon	apatite	K-fsp.	plag	omph symp.	phen symp.	amph	epidote group	biotite	carb.	titanite	chlorite	quartz	parag.
9837 gneisic eclogite	+	+	+	+	(-)	-	+	+	+	-	+	+	+	+	+	-	-	(+)	+	-
99101 gneissic eclogite	+	+	+	+	(-)	-	+	+	(-)	+	+	+	+	+	+	-	+	-	+	-
99102 eclogite lens	+	+	+	+	+	-	+	-	-	-	+	+	-	-	-	-	+	-	(+)	-
99178 gabbroic eclogite	+	+	+	-	+	+	+	-	-	-	+	-	+	+	+	-	-	-	+	+
99103 gneiss	+	-	+	+	-	-	+	-	(-)	+	+	+	+	+	+	+	+	-	+	-
99104 gneiss	-	-	+	-	-	-	+	+	(-)	+	+	+	+	+	+	+	+	-	+	-

Table A2a: Representative EMP analyses of garnet from basement samples

Sample	9837	99101	99102	99103	99178
mineral	garnet	garnet	garnet	garnet	garnet
comment	2-10	1-1-8	2-5-2	3-1-5	S1
		s-4	s-4	s-4	1-4
	1	1	2	15	4
SiO2	38.99	39.42	39.24	39.70	40.28
TiO2	0.09	0.03	0.05	0.06	0.07
Al2O3	22.18	22.20	22.00	22.04	22.74
FeO	21.53	22.75	21.71	21.00	14.10
MnO	0.40	0.45	0.44	0.41	0.26
MgO	5.20	5.84	6.65	5.48	8.92
CaO	12.10	11.85	10.55	12.74	14.43
Ia2O (n.m.)	0.00	0.00	0.00	0.00	0.00
K2O (n.m.)	0.00	0.00	0.00	0.00	0.00
Cr2O3	0.00	0.04	0.03	0.03	0.14
Fe2O3	1.45	0.00	0.00	0.00	0.00
sum	**101.94**	**102.58**	**102.63**	**101.47**	**100.94**
cations					
Si	2.96	2.97	2.99	3.01	2.99
Ti	0.01	0.00	0.00	0.00	0.00
Al	1.98	1.97	1.98	1.97	1.99
Fe2+	1.41	1.37	1.36	1.31	0.86
Mn	0.03	0.03	0.03	0.03	0.02
Mg	0.59	0.66	0.76	0.62	0.99
Ca	0.98	0.96	0.86	1.03	1.15
Na	0.00	0.00	0.00	0.00	0.00
K	0.00	0.00	0.00	0.00	0.00
Cr	0.00	0.00	0.00	0.00	0.01
Fe3+	0.06	0.06	0.03	0.02	0.02
Sum	**8.02**	**8.01**	**8.00**	**7.99**	**8.00**
formula					
Mg	0.59	0.66	0.76	0.62	0.99
Mn	0.03	0.03	0.03	0.03	0.02
Ca	0.98	0.96	0.86	1.03	1.15
FeII	1.41	1.37	1.36	1.31	0.86
sum X	**3.01**	**3.01**	**3.00**	**2.99**	**3.00**
exc. Fe	*0.01*	*0.01*	*0.00*	*-0.01*	*0.00*
Si	2.96	2.97	2.99	3.01	2.99
Aliv	0.04	0.03	0.01	0.00	0.01
sum Z	**3.00**	**3.00**	**3.00**	**3.01**	**3.00**
Alvi	1.94	1.94	1.97	1.97	1.97
Cr	0.00	0.00	0.00	0.00	0.01
Ti	0.01	0.00	0.00	0.00	0.00
FeIII	0.06	0.06	0.03	0.02	0.02
sum Y	**2.00**	**2.00**	**2.00**	**1.99**	**2.00**
dmembers					
pyrope	19.54	21.80	25.18	20.70	32.81
almandine	46.92	45.50	45.16	43.83	28.53
grossular	29.88	28.47	27.23	33.53	36.87
spessartine	0.85	0.95	0.95	0.89	0.53
andradite	2.80	3.17	1.39	0.97	0.85

Table A2b: Representative EMP analyses of omphacite from basement samples

Sample	9837	99102	99178
mineral	omphacite	omphacite	omphacite
comment	2-8	2-5-5	1-3-14
		s-4	prof c-r
		40	S-1
SiO2	57.63	56.29	57.38
TiO2	0.04	0.06	0.06
Al2O3	17.43	15.14	12.35
FeO	2.84	3.51	1.69
MnO	0.00	0.01	0.00
MgO	4.67	5.98	8.61
CaO	7.35	9.99	13.20
Na2O	10.43	9.30	7.26
K2O	0.00	0.00	0.00
Cr2O3	0.00	0.00	0.17
Fe2O3	0.44	0.00	0.00
sum	**100.83**	**100.27**	**100.71**
cations			
Si	1.98	1.97	1.99
Ti	0.00	0.00	0.00
Al	0.71	0.62	0.51
Cr	0.00	0.00	0.00
Fe3+	0.05	0.05	0.02
Mg	0.24	0.31	0.45
Ca	0.27	0.37	0.49
Mn	0.00	0.00	0.00
Fe2+	0.05	0.05	0.02
Na	0.70	0.63	0.49
K	0.00	0.00	0.00
sum	**3.99**	**4.01**	**3.98**
formula			
Si	1.98	1.97	1.99
Al	0.02	0.03	0.01
Fe3+	0.00	0.00	0.00
sum	**2.00**	**2.00**	**2.00**
Al	0.69	0.59	0.50
Fe3+	0.05	0.05	0.02
Cr	0.00	0.00	0.00
Ti	0.00	0.00	0.00
Mg	0.22	0.31	0.45
Fe2+	0.05	0.05	0.02
Mn	0.00	0.00	0.00
sum	**1.00**	**1.00**	**1.00**
Mg	0.02	0.00	0.00
Fe2+	0.00	0.00	0.00
Mn	0.00	0.00	0.00
Ca	0.27	0.37	0.49
Na	0.70	0.63	0.49
K	0.00	0.00	0.00
sum	**0.98**	**1.01**	**0.98**
dmembers			
WEF	28.03	37.25	50.11
jadeite	67.29	57.74	47.56
aegerine	4.69	5.01	2.33

Table A2c: Representative EMP analyses of white mica from basement samples

sample	9837	99101	99102	99178
mineral	phengite	phengite	phengite	paragonite
comment	22-6	1-1-7	2-5-1	S3
		s-4	s-4	3-2-2
		8	8	3
SiO2	53.46	53.20	52.99	48.24
TiO2	0.23	0.24	0.36	0.08
Al2O3	24.21	24.32	23.98	39.87
Cr2O3	0.00	0.03	0.03	0.17
FeO	1.78	2.83	1.59	0.31
MnO	0.02	0.05	0.01	0.00
MgO	4.72	4.43	4.91	0.14
CaO	0.00	0.04	0.01	0.53
BaO	0.00	0.22	0.63	0.03
Na2O	0.10	0.19	0.08	7.22
K2O	10.70	10.56	10.87	0.48
Fe2O3	0.00	0.00	0.00	0.00
sum	**95.22**	**96.10**	**95.46**	**97.07**
cations				
Si	3.54	3.52	3.53	3.02
Ti	0.01	0.01	0.02	0.00
Al	1.89	1.89	1.88	2.94
Cr	0.00	0.00	0.00	0.01
Fe 2+	0.05	0.08	0.04	0.01
Mn	0.00	0.00	0.00	0.00
Mg	0.47	0.44	0.49	0.01
Ca	0.00	0.00	0.00	0.04
Ba	0.00	0.01	0.02	0.00
Na	0.01	0.02	0.01	0.88
K	0.90	0.89	0.92	0.04
Fe 3+	0.05	0.08	0.04	0.01
sum	**6.93**	**6.94**	**6.96**	**6.95**
Si	3.54	3.52	3.53	3.02
Al	0.46	0.48	0.47	0.98
sum	**4.00**	**4.00**	**4.00**	**4.00**
Octaeder				
Al	1.44	1.41	1.41	1.96
Cr	0.00	0.00	0.00	0.01
Ti	0.01	0.01	0.02	0.00
Mg	0.47	0.44	0.49	0.01
Fe2+	0.05	0.08	0.04	0.01
Fe3+	0.05	0.08	0.04	0.01
Mn	0.00	0.00	0.00	0.00
sum	**2.01**	**2.02**	**2.01**	**2.00**
Interlayer				
Ca	0.00	0.00	0.00	0.04
Ba	0.00	0.01	0.02	0.00
Na	0.01	0.02	0.01	0.88
K	0.90	0.89	0.92	0.04
sum	**0.92**	**0.92**	**0.95**	**0.95**
dmembers (Schliestedt 1980)				
muscovite	44.13	45.40	45.99	2.05
celadonite	54.47	51.62	52.83	2.01
paragonite	1.40	2.64	1.13	92.24
margarite	0.00	0.34	0.05	3.71

Table A3: Observed mineral assemblages in eclogite and calc-silicate samples from the Changpu Unit. Numbers in brackets refer to sample localities (cf. Fig. 8).

	eclogite-facies assemblages										retrogressive assemblages												
	grt	omp	phe	rt	carb	ky	coe/qz	zr	apa	clz/zoi	amph	omp symp	phen symp	epi-gr	clz/zoi	sph	plag	bio	para	op	qz	carb	chl
phen-eclogites																							
9712 (1)	+	+	+	+	-	-	-	+	-	-	+	+	+	+	+	-	-	-	-	+	-	+	-
9872 (6)	+	+	+	+	-	-	+	+	-	-	+	+	-	-	-	-	-	-	-	+	+	-	-
9857 (5)	+	+	+	+	-	+	+	+	-	-	+	+	+	-	+	-	-	-	-	+	+	-	-
9854 (5)	+	+	+	+	-	-	+	+	+	-	+	+	+	-	-	+	-	-	-	+	+	-	-
9718 (8)	+	+	+	+	-	-	-	-	-	-	+	+	+	+	+	-	-	+	-	-	+	-	-
9719 (8)	+	+	+	+	-	-	-	+	-	+	+	+	+	+	+	-	-	+	-	+	+	-	+
carb-eclogites																							
98335 (4)	+	(+)	+	+	+	-	-	+	-	-	+	+	+	-	+	+	+	+	-	+	+	+	+
98382 (2)	+	(+)	+	+	-	-	+	+	+	-	+	+	-	+	-	+	+	+	-	+	+	+	+
98411 (1)	+	(+)	+	+	+	-	-	+	-	-	+	+	+	+	-	+	+	-	-	+	+	+	-
98133 (7)	+	+	+	+	+	-	-	+	-	-	+	+	+	-	-	-	-	-	-	+	+	+	-
9867 (1)	+	(+)	+	+	+	-	-	+	-	-	+	+	-	+	-	-	-	-	-	+	+	+	-
98409 (1)	+	(+)	+	+	+	-	+	+	-	-	+	+	+	+	+	-	+	+	-	+	+	+	-
9869 (1)	+	(-)	+	+	+	-	-	+	-	-	+	-	+	+	+	+	+	+	-	+	+	+	-
calc-silicates																							
9712 (1)	-	+	+	+	+	-	+	+	-	-	+	+	+	+	+	+	-	-	-	+	+	+	-
98408 (1)	-	+	+	+	+	-	+	+	-	-	+	+	+	+	+	+	+	+	-	+	+	+	-

Table A4a: EMP analyses of garnet from samples Dab 9712, 9857, 98335 as used in P-T plots (cf. Figs. 45, 46). Analysis numbers refer to Table A5.

sample	9712	9712	9712	9712	9712	9712	9712	9857	9857	9857	9857	98335	98335	98335	98335	98335	98335
analy. #	1	2	3	4	5	6	7	8	9	10	11	12	13	14	15	16	17
SiO2	39.21	39.36	38.47	38.67	39.69	39.13	39.02	38.97	39.10	38.83	38.05	37.79	38.20	38.03	38.01	38.13	37.90
TiO2	0.10	0.13	0.14	0.08	0.09	0.14	0.06	0.07	0.03	0.11	0.03	0.26	0.16	0.19	0.13	0.20	0.14
Al2O3	22.59	22.83	22.53	22.62	22.44	21.70	22.55	21.89	21.82	21.74	20.87	21.24	21.34	21.27	21.37	21.16	21.15
Cr2O3	0.02	0.00	0.00	0.04	0.00	0.00	0.01	0.01	0.01	0.04	0.00	0.10	0.11	0.08	0.09	0.07	0.04
FeO	12.80	16.89	12.80	16.28	14.48	16.42	15.49	17.45	19.35	18.31	19.48	17.75	18.81	18.43	19.39	18.61	19.67
MnO	0.46	0.52	0.37	0.55	0.38	0.59	0.48	0.38	0.39	0.35	0.33	0.41	0.42	0.39	0.45	0.45	0.52
MgO	6.04	5.77	5.47	5.10	5.75	4.26	5.61	4.56	4.33	4.26	4.51	3.64	4.27	3.86	3.94	3.84	3.33
CaO	18.67	16.16	18.29	16.79	17.94	17.65	16.65	15.56	14.81	15.29	14.29	16.56	14.80	16.00	14.82	15.86	14.93
Na2O	0.05	0.06	0.01	0.03	0.02	0.02	0.02	-	-	-	-	-	-	-	-	-	-
K2O	0.03	0.02	0.00	0.00	0.00	0.00	0.00	-	-	-	-	-	-	-	-	-	-
Sum	99.96	#####	98.07	#####	#####	99.90	99.88	98.90	99.84	98.93	97.56	97.74	98.09	98.26	98.19	98.31	97.68
cations																	
Si	2.96	2.95	2.96	2.95	2.98	3.00	2.97	3.01	3.01	3.01	3.00	2.98	3.00	2.99	2.99	2.99	3.01
Ti	0.01	0.01	0.01	0.00	0.01	0.01	0.00	0.00	0.00	0.01	0.00	0.02	0.01	0.01	0.01	0.01	0.01
Al	2.01	2.02	2.05	2.03	1.99	1.96	2.02	2.00	1.98	1.99	1.94	1.98	1.97	1.97	1.98	1.96	1.98
Cr	0.00	0.00	0.00	0.00	0.00	0.00	0.00	0.00	0.00	0.00	0.00	0.01	0.01	0.00	0.01	0.00	0.00
Fe3+	0.02	0.03	0.00	0.01	0.02	0.03	0.01	0.00	0.01	0.00	0.05	0.02	0.01	0.03	0.01	0.03	0.01
Fe2+	0.79	1.03	0.82	1.02	0.89	1.03	0.98	1.13	1.24	1.19	1.23	1.15	1.23	1.18	1.26	1.19	1.30
Mn	0.03	0.03	0.02	0.04	0.02	0.04	0.03	0.02	0.03	0.02	0.02	0.03	0.03	0.03	0.03	0.03	0.03
Mg	0.68	0.64	0.63	0.58	0.65	0.49	0.64	0.53	0.50	0.49	0.53	0.43	0.50	0.45	0.46	0.45	0.39
Ca	1.51	1.30	1.51	1.37	1.45	1.45	1.36	1.29	1.22	1.27	1.21	1.40	1.24	1.35	1.25	1.33	1.27
Na	0.01	0.01	0.00	0.00	0.00	0.00	0.00	0.00	0.00	0.00	0.00	0.00	0.00	0.00	0.00	0.00	0.00
K	0.00	0.00	0.00	0.00	0.00	0.00	0.00	0.00	0.00	0.00	0.00	0.00	0.00	0.00	0.00	0.00	0.00
Sum	8.02	8.02	8.01	8.02	8.01	8.00	8.01	7.98	7.99	7.98	8.00	8.00	8.00	8.00	8.00	8.00	7.99
Mg	0.68	0.64	0.63	0.58	0.65	0.49	0.64	0.53	0.50	0.49	0.53	0.43	0.50	0.45	0.46	0.45	0.39
Mn	0.03	0.03	0.02	0.04	0.02	0.04	0.03	0.02	0.03	0.02	0.02	0.03	0.03	0.03	0.03	0.03	0.03
Ca	1.51	1.30	1.51	1.37	1.45	1.45	1.36	1.29	1.22	1.27	1.21	1.40	1.24	1.35	1.25	1.33	1.27
Fe 2+	0.79	1.03	0.82	1.02	0.89	1.03	0.98	1.13	1.24	1.19	1.23	1.15	1.23	1.18	1.26	1.19	1.30
Sum	3.01	3.01	2.99	3.01	3.00	3.00	3.01	2.97	2.99	2.97	3.00	3.00	3.00	3.00	3.00	3.00	2.99
Al	1.97	1.97	2.01	1.98	1.97	1.96	1.99	2.00	1.98	1.99	1.94	1.96	1.97	1.95	1.97	1.95	1.98
Cr	0.00	0.00	0.00	0.00	0.00	0.00	0.00	0.00	0.00	0.00	0.00	0.01	0.01	0.00	0.01	0.00	0.00
Ti	0.01	0.01	0.01	0.00	0.01	0.01	0.00	0.00	0.00	0.01	0.00	0.02	0.01	0.01	0.01	0.01	0.01
Fe 3+	0.02	0.03	0.00	0.01	0.02	0.03	0.01	0.00	0.01	0.00	0.05	0.02	0.01	0.03	0.01	0.03	0.01
Sum	2.00	2.00	2.02	2.01	2.00	2.00	2.00	2.00	1.99	2.00	2.00	2.00	2.00	2.00	2.00	2.00	1.99
Si	2.96	2.95	2.96	2.95	2.98	3.00	2.97	3.01	3.01	3.01	3.00	2.98	3.00	2.99	2.99	2.99	3.01
Al	0.04	0.05	0.04	0.05	0.02	0.00	0.03	0.00	0.00	0.00	0.00	0.02	0.00	0.01	0.01	0.01	0.00
Sum	3.00	3.00	3.00	3.00	3.00	3.00	3.00	3.01	3.01	3.01	3.00	3.00	3.00	3.00	3.00	3.00	3.01

Table A4b: EMP analyses of omphacite from samples Dab 9712, 9857, 98335 as used in P-T plots (cf. Figs. 45, 46). Analyses # refer to Table A5.

sample	9712	9712	9712	9712	9712	9712	9712	9712	9857	9857	98335
analy. #	1	2	3	4	5	6	7	8	9	10	11
SiO2	55.52	55.03	55.05	55.24	55.18	54.45	56.10	56.05	56.84	58.27	55.87
TiO2	0.03	0.04	0.05	0.00	0.02	0.06	0.00	0.00	0.05	0.03	0.08
Al2O3	7.37	6.43	7.10	6.52	7.10	5.73	7.69	7.32	15.93	12.86	10.25
Cr2O3	0.00	0	0.00	0.06	0.06	0.00	0.00	0.00	0.00	0.01	0.02
FeO	3.12	3.49	2.80	2.77	3.22	5.00	3.50	3.52	2.66	2.99	4.83
MnO	0.00	0.01	0.03	0.00	0.04	0.05	0.04	0.04	0.04	0.04	0.00
MgO	11.67	11.88	11.97	12.30	12.06	11.91	11.49	11.68	4.92	8.43	8.04
CaO	17.56	18.73	17.90	18.70	17.60	19.52	17.32	18.33	8.29	12.75	13.50
Na2O	4.30	3.52	4.01	3.69	4.21	3.31	4.67	4.41	9.75	6.36	6.98
K2O	0.04	0.03	0.00	0.03	0.01	0.04	0.01	0.00	0.00	0.00	0.04
Sum	99.62	99.16	98.91	99.31	99.50	100.07	100.81	101.34	98.48	101.73	99.61
cations											
Si	1.99	1.98	1.98	1.99	1.98	1.96	1.98	1.98	2.00	2.00	1.99
Ti	0.00	0.00	0.00	0.00	0.00	0.00	0.00	0.00	0.00	0.00	0.00
Al	0.31	0.27	0.30	0.28	0.30	0.24	0.32	0.30	0.66	0.52	0.43
Cr	0.00	0.00	0.00	0.00	0.00	0.00	0.00	0.00	0.00	0.00	0.00
Fe3+	0.05	0.05	0.04	0.04	0.05	0.08	0.05	0.05	0.04	0.04	0.07
Mg	0.62	0.64	0.64	0.66	0.64	0.64	0.61	0.61	0.26	0.43	0.43
Ca	0.67	0.72	0.69	0.72	0.68	0.75	0.66	0.69	0.31	0.47	0.52
Mn	0.00	0.00	0.00	0.00	0.00	0.00	0.00	0.00	0.00	0.00	0.00
Fe2+	0.05	0.05	0.04	0.04	0.05	0.08	0.05	0.05	0.04	0.04	0.07
Na	0.30	0.25	0.28	0.26	0.29	0.23	0.32	0.30	0.67	0.42	0.48
K	0.00	0.00	0.00	0.00	0.00	0.00	0.00	0.00	0.00	0.00	0.00
Sum	3.98	3.97	3.98	3.98	3.99	3.99	3.99	4.00	3.98	3.93	4.00
Mg	0.01	0.00	0.01	0.01	0.02	0.00	0.01	0.00	0.00	0.03	0.00
Ca	0.67	0.72	0.69	0.72	0.68	0.75	0.66	0.69	0.31	0.47	0.52
Na	0.30	0.25	0.28	0.26	0.29	0.23	0.32	0.30	0.67	0.42	0.48
K	0.00	0.00	0.00	0.00	0.00	0.00	0.00	0.00	0.00	0.00	0.00
Sum	0.98	0.97	0.98	0.98	0.99	0.99	0.99	1.00	0.98	0.93	1.00
Al	0.30	0.26	0.28	0.26	0.28	0.21	0.30	0.28	0.66	0.52	0.42
Fe3+	0.05	0.05	0.04	0.04	0.05	0.08	0.05	0.05	0.04	0.04	0.07
Cr	0.00	0.00	0.00	0.00	0.00	0.00	0.00	0.00	0.00	0.00	0.00
Ti	0.00	0.00	0.00	0.00	0.00	0.00	0.00	0.00	0.00	0.00	0.00
Mg	0.61	0.64	0.63	0.65	0.62	0.64	0.59	0.61	0.26	0.40	0.43
Fe2+	0.05	0.05	0.04	0.04	0.05	0.08	0.05	0.05	0.04	0.04	0.07
Mn	0.00	0.00	0.00	0.00	0.00	0.00	0.00	0.00	0.00	0.00	0.00
Sum	1.00	1.00	1.00	1.00	1.00	1.00	1.00	1.00	1.00	1.00	1.00
Si	1.99	1.98	1.98	1.99	1.98	1.96	1.98	1.98	2.00	2.00	1.99
Al	0.01	0.02	0.02	0.01	0.02	0.04	0.02	0.02	0.00	0.00	0.01
Sum	2.00	2.00	2.00	2.00	2.00	2.00	2.00	2.00	2.00	2.00	2.00

Table A4c: EMP analyses of phengite for samples Dab 9712, 9857, 98335, as used in P-T plots (cf. Figs. 45, 46). Analyses # refer to Table A5.

sample	9712	9712	9712	9712	9712	9712	9712	9712	9712	9712	9857	9857	9857	9857	9857	98335	98335	98335	98335	98335	98335
analy. #	1	2	3	4	5	6	7	8	9	10	11	12	13	14	15	16	17	18	19	20	21
SiO2	53.11	48.28	53.01	46.68	53.61	48.05	56.92	54.15	55.42	53.33	52.36	51.83	52.21	55.70	54.22	53.98	51.54	55.46	53.75	55.03	53.90
TiO2	0.30	0.72	0.32	0.75	0.30	0.37	0.32	0.32	0.33	0.38	0.30	0.27	0.29	0.29	0.29	0.34	0.44	0.30	0.39	0.30	0.29
Al2O3	23.19	28.26	23.12	28.31	22.16	28.52	24.01	24.91	24.12	26.88	24.85	25.05	25.10	26.66	28.88	22.44	24.69	20.46	23.18	21.11	22.17
FeO	1.62	2.07	2.16	3.28	1.76	2.60	0.78	1.51	1.59	1.51	1.72	1.94	1.39	1.67	1.71	2.14	2.50	2.36	2.49	2.56	2.66
MnO	0.00	0.01	0.01	0.02	0.00	0.00	0.00	0.02	0.00	0.00	0.01	0.01	0.03	0.00	0.02	0.00	0.01	0.00	0.05	0.02	0.00
MgO	4.96	3.42	4.86	3.14	5.39	3.19	4.87	5.12	5.50	4.52	4.21	4.21	4.29	4.53	3.89	4.80	4.17	5.29	4.28	4.94	4.49
CaO	0.01	0.02	0.00	0.10	0.00	0.00	0.81	0.00	0.03	0.04	0.00	0.00	0.00	0.00	0.00	0.02	0.08	0.00	0.02	0.00	0.01
Na2O	0.23	0.33	0.17	0.33	0.11	0.33	1.38	0.21	0.21	0.26	0.47	0.44	0.30	0.22	0.43	0.18	0.17	0.11	0.13	0.15	0.19
K2O	10.26	11.26	10.81	10.98	11.44	11.50	8.61	10.35	9.72	9.86	10.42	10.36	10.93	9.89	9.75	10.55	10.86	10.40	10.51	10.31	10.38
Sum	93.66	94.37	94.45	93.58	94.77	94.57	97.70	96.58	96.92	96.79	94.34	94.11	94.52	98.94	99.18	94.44	94.45	94.38	94.79	94.42	94.10
cations																					
Si	3.57	3.27	3.56	3.21	3.59	3.26	3.63	3.53	3.58	3.46	3.51	3.48	3.49	3.52	3.42	3.61	3.47	3.71	3.58	3.68	3.62
Ti	0.02	0.04	0.02	0.04	0.02	0.02	0.02	0.02	0.02	0.02	0.02	0.01	0.01	0.01	0.01	0.02	0.02	0.01	0.02	0.02	0.01
Al	1.84	2.26	1.83	2.29	1.75	2.28	1.80	1.91	1.84	2.05	1.96	1.98	1.98	1.99	2.15	1.77	1.96	1.61	1.82	1.66	1.76
Fe 3+	0.05	0.06	0.06	0.09	0.05	0.07	0.02	0.04	0.04	0.04	0.05	0.05	0.04	0.04	0.05	0.06	0.07	0.07	0.07	0.07	0.07
Fe 2+	0.05	0.06	0.06	0.09	0.05	0.07	0.02	0.04	0.04	0.04	0.05	0.05	0.04	0.04	0.05	0.06	0.07	0.07	0.07	0.07	0.07
Mn	0.00	0.00	0.00	0.00	0.00	0.00	0.00	0.00	0.00	0.00	0.00	0.00	0.00	0.00	0.00	0.00	0.00	0.00	0.00	0.00	0.00
Mg	0.50	0.35	0.49	0.32	0.54	0.32	0.46	0.50	0.53	0.44	0.42	0.42	0.43	0.43	0.37	0.48	0.42	0.53	0.43	0.49	0.45
Ca	0.00	0.00	0.00	0.01	0.00	0.00	0.06	0.00	0.00	0.00	0.00	0.00	0.00	0.00	0.00	0.00	0.01	0.00	0.00	0.00	0.00
Na	0.03	0.04	0.02	0.04	0.01	0.04	0.17	0.03	0.03	0.03	0.06	0.06	0.04	0.03	0.05	0.02	0.02	0.01	0.02	0.02	0.02
K	0.88	0.97	0.92	0.96	0.98	0.99	0.70	0.86	0.80	0.82	0.89	0.89	0.93	0.80	0.79	0.90	0.93	0.89	0.89	0.88	0.89
Sum	6.92	7.04	6.96	7.06	6.99	7.07	6.88	6.92	6.88	6.90	6.95	6.96	6.97	6.86	6.88	6.92	6.97	6.89	6.91	6.89	6.91
Si	3.57	3.27	3.56	3.21	3.59	3.26	3.63	3.53	3.58	3.46	3.51	3.48	3.49	3.52	3.42	3.61	3.47	3.71	3.58	3.68	3.62
Al	0.43	0.73	0.44	0.79	0.41	0.74	0.37	0.47	0.42	0.54	0.49	0.52	0.51	0.48	0.58	0.39	0.53	0.29	0.42	0.32	0.38
Sum	4.00	4.00	4.00	4.00	4.00	4.00	4.00	4.00	4.00	4.00	4.00	4.00	4.00	4.00	4.00	4.00	4.00	4.00	4.00	4.00	4.00
Al	1.41	1.53	1.39	1.50	1.34	1.54	1.43	1.44	1.42	1.51	1.47	1.47	1.47	1.51	1.57	1.38	1.43	1.32	1.41	1.34	1.38
Ti	0.02	0.04	0.02	0.04	0.02	0.02	0.02	0.02	0.02	0.02	0.02	0.01	0.01	0.01	0.01	0.02	0.02	0.01	0.02	0.02	0.01
Mg	0.50	0.35	0.49	0.32	0.54	0.32	0.46	0.50	0.53	0.44	0.42	0.42	0.43	0.43	0.37	0.48	0.42	0.53	0.43	0.49	0.45
Fe2+	0.05	0.06	0.06	0.09	0.05	0.07	0.02	0.04	0.04	0.04	0.05	0.05	0.04	0.04	0.05	0.06	0.07	0.07	0.07	0.07	0.07
Fe3+	0.05	0.06	0.06	0.09	0.05	0.07	0.02	0.04	0.04	0.04	0.05	0.05	0.04	0.04	0.05	0.06	0.07	0.07	0.07	0.07	0.07
Mn	0.00	0.00	0.00	0.00	0.00	0.00	0.00	0.00	0.00	0.00	0.00	0.00	0.00	0.00	0.00	0.00	0.00	0.00	0.00	0.00	0.00
Sum	2.01	2.03	2.01	2.05	2.00	2.03	1.95	2.04	2.05	2.05	2.00	2.01	2.00	2.04	2.05	1.99	2.01	1.99	1.99	1.99	1.99
Ca	0.00	0.00	0.00	0.01	0.00	0.00	0.06	0.00	0.00	0.00	0.00	0.00	0.00	0.00	0.00	0.00	0.01	0.00	0.00	0.00	0.00
Na	0.03	0.04	0.02	0.04	0.01	0.04	0.17	0.03	0.03	0.03	0.06	0.06	0.04	0.03	0.05	0.02	0.02	0.01	0.02	0.02	0.02
K	0.88	0.97	0.92	0.96	0.98	0.99	0.70	0.86	0.80	0.82	0.89	0.89	0.93	0.80	0.79	0.90	0.93	0.89	0.89	0.88	0.89
Sum	0.91	1.02	0.95	1.01	0.99	1.04	0.93	0.89	0.83	0.85	0.95	0.95	0.97	0.82	0.84	0.92	0.96	0.90	0.91	0.90	0.91

Table A5: Summary of P-T data for all investigated samples from the Changpu Unit with their key textural and chemical features. Data for Dab 9712, 9857 and 98335 are plotted in Fig. 45 and 46. See also chapter 4.

	garnet	omphacite	phengite	others	P-T
sample #/*comment*	X ca				T (°C)-P (kbar) K
rock type/*texture*	X mg	X mg	Si p.f.u.		T (°C)-P (kbar) P
phe texture	a grs	X jd	X mg		T (°C)-P (kbar) G&H
min. texture	a py	a di	a inv. phe		P (kbar)-T (°C) W&M
9712 (1,1,1) II	0.5024	0.9301	3.64		711/40
def. Phe-eclogite lens	0.4638	0.3026	0.91		793/40
matirx, centre	0.1781	0.5801	0.7588		727/40
cores	0.0358				41.5-700
(2,2,2) II-	0.4314	0.9238	3.27		557-20
def. Phe-eclogite lens	0.3844	0.2523	0.86		650-20
matirx, centre	0.1169	0.6045	2.5384		645-20
rims	0.0267				22.7-600
(3,3,3) III	0.4812	0.9303	3.59		665-40
def. Phe-eclogite lens	0.4204	0.2955	0.92		738-40
matrix, rim	0.1519	0.5791	0.6373		688-40
cores	0.0289				38.7-700
(4,4,4)	0.4833	0.8945	3.26		609-20
def. Phe-eclogite lens	0.3217	0.2337	0.81		702-20
matrix, rim	0.1378	0.60249	2.8118		625-20
rims	0.0130				19.6-600
(5,5,5) III-	0.5054	0.1310	3.56		655-40
eclogite/calc-silicate	0.4324	0.2846	0.89		736-40
at contact	0.1793	0.5948	0.8113		740-40
cores	0.0299				36.9-700
(6,6,6)	0.4556	0.9405	3.21		505-20
eclogite/calc-silicate	0.3617	0.2614	0.77		599-20
at contact	0.1334	0.6155	3.0605		715-20
rims	0.0214				20.2-600
(1,7,7) I	0.5024	0.9213	3.68		744-40
eclogite/calc-silicate	0.4638	0.3232	0.95		825-40
inc. Omph	0.1781	0.5679	0.3875		635-40
cores	0.0358				46-700
(-,7,7)	ideal	0.9213	3.68		
eclogite/calc-silicate	ideal	0.3232	0.95		
inc. Omph	0.125	0.5679	0.3875		
cores	0.125				39.9-700
(7,8,8) III	0.5024	0.9213	3.58		744-40
calc-silicate	0.4638	0.3232	0.92		825-40
matrix	0.1781	0.5679	0.7100		695-40
cores	0.0358				39.8-700
(8,7,9) III-	0.4344	0.912	3.46		700-30
calc-silicate	0.3179	0.3234	0.91		802-30
matrix	0.1052	0.5679	1.2864		624-30
rims	0.0147				29.6-600
(7,8,10) VI	0.4517	0.9221	3.53		619-30
calc-silicate	0.3935	0.3029	0.92		698-30
incl. Titanite	0.1323	0.5920	0.8953		608-30
cores	0.0270				32.9-600
Titanite reaction (7,-,-)	0.4517			a, x H20 1	
eclogite/calc-silic.	0.3935			a rt, SiO2 1	
	0.1323			a tit 0.863	35.5-600
rims	0.0270			a zoi 0.8141	
9872	0.3255	0.9187	3.57		594-30
Phe-eclogite	0.4399	0.4145	0.91		661-30
at Grt rim	0.0601	0.5262	0.9390		659-30
cores	0.0481				32-700
	0.3185	0.9197	3.51		569-30
Phe-eclogite	0.4131	0.4152	0.90		630-30
at Grt rim	0.0519	0.5313	1.2521		660-30
rims	0.0386				27.2-600
	0.3255	0.9187	3.59		594-30
Phe-eclogite	0.4399	0.4145	0.92		661-30
incl. Grt	0.0601	0.5262	0.8185		646-30
cores	0.0481				33.5-700
	0.3094	0.9197	3.25		527-20
Phe-eclogite	0.4240	0.4152	0.89		608-20
incl. grt	0.0497	0.5313	2.2300		607-20
rims	0.0428				21.2-700
	0.3255	0.9187	3.57		594-30
Phe-eclogite	0.4399	0.4145	0.90		661-30
matrix	0.0601	0.5262	0.92286		671-30
cores	0.0481				32.2-700
	0.3185	0.9197	3.15		527-20
Phe-eclogite	0.4131	0.4152	0.82		608-20
matrix	0.0519	0.5313	1.9951		700-20
rims	0.0386				22.9-600

Table A5: Summary of P-T data for all investigated samples from the Changpu Unit with their key textural and chemical features.Data for Dab 9712, 9857 and 98335 are plotted in Fig. 45 and 46. See also chapter 4.

9857 (8,9,11) II	0.4344	0.8680	3.51		723-40
Phe-eclogite	0.3179	0.6802	0.90		766-40
at Grt rims	0.1052	0.3701	1.1451		658-40
cores	0.0147				37.3-700
(9,10,12) II-	0.4093	0.9095	3.48		548-30
Phe-eclogite	0.2863	0.4564	0.89		609-30
at Grt rims	0.0880	0.4309	1.2136		603-30
rims	0.0118				30.9-600
(8,9,13) II	0.4344	0.8680	3.49		723-40
Phe-eclogite	0.3179	0.6802	0.92		766-40
incl. Ky	0.1052	0.3701	1.1658		628-40
cores	0.0147				37.1-700
(9,10,12) II-	0.4093	0.9095	3.50		548-30
Phe-eclogite	0.2863	0.4564	0.92		609-30
incl. Ky	0.0880	0.4309	1.2077		565-30
rims	0.0118				31-600
(10,9,14) I	0.4274	0.8680	3.52		692-40
Phe-eclogite	0.2929	0.6802	0.91		734-40
matrix	0.0985	0.3701	1.1104		649-40
cores	0.0120				37.6-700
(11,10,15) I-	0.4035	0.9095	3.42		556-30
Phe-eclogite	0.3010	0.4564	0.89		618-30
matrix	0.0833	0.4309	1.7355		606-30
min. rims	0.0134				27.6-600
	0.4093	0.9095			
Kyanite reaction(9,10,-)	0.2863	0.4564			
Phe-eclogite	0.1296	0.4309			intersection
	0.0420	a hd 0.04			40.5-648
cores a alm 0.046	a jd 0.42				
9854	0.3276	0.8499	3.45		682-30
Phe-eclogite	0.3448	0.6446	0.78		723-30
matrix	0.0519	0.3691	1.1269		751-30
cores	0.0235				34-700
	0.3217	0.8414	3.23		581-20
Phe-eclogite	0.2949	0.6439	0.69		645-20
matrix	0.04634	0.3795	3.2554		772-20
rims	0.0153				20.2-700
	0.3231	0.8499	3.50		697-40
Phe-eclogite	0.3165	0.6446	0.80		718-40
at Grt rim	0.0468	0.3691	0.8709		771-40
cores	0.0191				35.2-700
	0.3072	0.8414	3.28		594-20
Phe-eclogite	0.3173	0.6439	0.72		658-20
at Grt rim	0.0424	0.3795	2.5106		728-20
rims	0.0194				23.1-700
	0.3364	0.8499	3.48		700-40
Phe-eclogite	0.3126	0.6446	0.79		724-40
incl. Grt	0.0552	0.3691	0.9718		775-40
cores	0.0181				35-700
	0.3293	0.8414	3.37		580-20
Phe-eclogite	0.2877	0.6439	0.76		644-20
incl. Grt	0.0499	0.3795	1.6311		730-30
rims	0.0143				27.6-700
98335 (12,11,16)	0.4657	0.8557	3.61		713-40
Carbonate-eclogite	0.2710	0.4826	0.89		759-40
incl. Grt	0.1229	0.4780	0.6970		640-40
cores	0.0088				36.2-700
(13,11,17)	0.4149	0.8557	3.47		665-30
Carbonate-eclogite	0.2889	0.4826	0.86		721-30
incl. Grt	0.0919	0.4780	1.2326		639-30
rims	0.0120				29.2-600
(14,11,18)	0.4479	0.8557	3.71		711-40
Carbonate-eclogite	0.2769	0.4826	0.89		754-40
matrix	0.1107	0.4780	0.4308		644-40
cores	0.0098				40.8-700
(15,11,19)	0.4160	0.8557	3.58		664-30
Carbonate-eclogite	0.2680	0.4826	0.86		699-30
matrix	0.0915	0.4780	0.8669		622-30
rims	0.0097				31.8-600
(16,11,20)	0.4443	0.8557	3.68		707-40
Carbonate-eclogite	0.2743	0.4826	0.87		748-40
at Grt rims	0.1066	0.4780	0.5644		661-40
cores	0.0094				37.6-700
(17,11,21)	0.4236	0.8557	3.62		609-30
Carbonate-eclogite	0.2323	0.4826	0.86		665-30
at Grt rims	0.0916	0.4780	0.7143		600-30
rims	0.0062				32.2-600

Table A5: Summary of P-T data for all investigated samples from the Changpu Unit with their key textural and chemical features.Data for Dab 9712, 9857 and 98335 are plotted in Fig. 45 and 46. See also chapter 4.

98411	0.4795	0.9320	3.44		618-30
Carbonate-eclogite	0.4210	0.3094	0.81		710-30
matrix	0.1371	0.5989	1.5674		670-30
cores	0.0264				27.7-700
	0.4348	0.9320	3.22		551-20
Carbonate-eclogite	0.4133	0.3094	0.661		652-20
matrix	0.1089	0.5989	5.0195		728-20
rims	0.0289				14.4-700
	0.4371	0.9320	3.61		570-30
Carbonate-eclogite	0.3797	0.3094	0.79		648-30
incl. Grt	0.1075	0.5989	0.7758		661-30
cores	0.0229				32.8-700
	0.4393	0.9320	3.42		528-20
Carbonate-eclogite	0.3649	0.3094	0.72		621-20
incl. Grt	0.1051	0.5989	1.9933		648-20
rims	0.0198				22.9-600
98382	0.3682	0.7707	3.36		712-30
Carbonate-eclogite	0.2326	0.2981	0.81		752-30
matrix	0.0639	0.3654	2.0334		699-40
cores	0.0074	*symplectite*			25.6-700
	0.3397	0.8531	3.28		482-10
Carbonate-eclogite	0.2271	0.1477	0.76		565-10
matrix	0.0480	0.6159	3.8251		575-10
rims	0.0068	*symplectite*			10.5-500
		0.7707			18.9-700 **H 80**
		0.2981			14.4-700 **H 80**
symplectite		0.3654			13.3-700 **H 90**
		0.8531			18.9-700 **H 80**
		0.1477			11.1-700 **H 80**
symplectite		0.6159			9.8-700 **H 90**
98133	0.2992	0.8872	3.44		558-30
Carbonate-eclogite	0.2328	0.6154	0.84		602-30
incl. Grt	0.0394	0.3941	1.6203		672-30
cores	0.0181				26.1-700
	0.2501	0.8901	3.28		483-20
Carbonate-eclogite	0.3082	0.6400	0.78		541-20
incl. Grt	0.0254	0.4161	2.6782		669-20
rims	0.0203				18.3-600
9867	0.4586		3.24		
Carbonate-eclogite	0.2988		0.71		
matrix	0.0118		3.8017		753-40
cores	0.01146				
	0.4741		3.20		
Carbonate-eclogite	0.3393		0.68		
matrix	0.1316		2.9752		611-20
rims	0.0156				
98409	0.4039		3.44		
Carbonate-eclogite	0.3037		0.77		
matrix	0.0868		1.2040		791-40
cores	0.0142				
	0.4289		3.20		
Carbonate-eclogite	0.3106		0.67		
matrix	0.1020		4.0563		765-20
rims	0.0143				
9869	0.3626		3.46		
Carbonate-eclogite	0.2773		0.79		
incl. Grt	0.0636		1.0119		704-40
cores	0.0111				
	0.3665		3.25		
Carbonate-eclogite	0.2552		0.73		
incl. Grt	0.0650		1.9479		587-20
rims	0.0088				
9719	0.2638	0.8243	3.37		685-20
foliated Phe-eclogite	0.4000	0.4747	0.82		741-20
matrix	0.0336	0.4516	2.0639		628-20
cores	0.0418				22.6-700
	0.2327	0.8609	3.30		578-20
foliated Phe-eclogite	0.3765	0.4776	0.81		642-20
matrix	0.0240	0.4640	2.9048		694-20
rims	0.0381				17.1-600
9718	0.2333	0.8513	3.58		723-30
Phe-eclogite	0.4540	0.4283	0.81		770-30
matrix	0.0274	0.4839	0.8504		685-30
cores	0.0642				30.3-700
	0.1913	0.8846	3.38		531-20
Phe-eclogite	0.4165	0.4033	0.88		600-20
matrix	0.0147	0.4947	1.7236		628-20
rims	0.0519				18.7-600
	0.2256			amph	
Phe-eclogite	0.4362			X fe 0.0763	~ 460 °C **G&P**
	0.0212			X mg 0.9236	
rims	0.0653				

Table A5: Summary of P-T data for all investigated samples from the Changpu Unit with their key textural and chemical features.Data for Dab 9712, 9857 and 98335 are plotted in Fig. 45 and 46. See also chapter 4.

99178	0.3820	0.9479			629-40
gabbroic eclogite	0.5366	0.4984			704-40
	0.0983	0.5088			
cores	0.0730				
	0.3645	0.9385			520-20
gabbroic eclogite	0.4544	0.3772			617-20
	0.0805	0.5494			
rims	0.0485				
Paragonite reaction		0.9479		Paragonite	
gabbroic eclogite		0.4984		a ms 0.174	600-22.5 (B 91)
		0.5088		a pa 0.88	
rims		a hd 0.049		a marg 0.036	
		a jd 0.49			
Kyanite reaction	0.3645	0.9385			
gabbroic eclogite	0.4544	0.3772			T limit for Kyanite
	0.1567	0.55			45 kbar-600°C (B 91)
rims	0.1256	a hd 0.03			40 kbar-700°C (B 91)
	a alm 0.02	a jd 0.37			

Table A6: Observed mineral assemblages of samples from the Ganghe Unit.

sample # / rock type	mineral / garnet	omph	rutile	phe	coesite	kyanite	zircon	apatite	K-fsp.	plag	omph symp.	phen symp.	amph	epidote group	biotite	carb.	titanite	chlorite	quartz
9933 — mafic dyke	+	+	+	-	(+)	-	+	-	-	-	-	-	(-)	+	-	-	+	-	+
99119 — streched eclogite	+	+	+	+	-	+	+	-	-	-	+	+	+	+	-	-	-	(-)	+
99122 — eclogite	+	+	+	+	-	-	+	+	-	-	+	+	+	+	-	-	-	-	+
99206 — layered eclogite	+	+	+	+	(-)	+	+	-	-	-	+	+	+	+	-	-	-	-	+

Table A 7a: Representative EMP analyses of garnet of samples from the Ganghe Unit

sample	9933	99119	99122	99206
mineral	garnet	garnet	garnet	garnet
comment	S8	S6	S3	S6
	e18	9-6-9	1-2-2	6-4-1
	2	24	12	19
SiO2	38.48	39.47	38.62	39.57
TiO2	0.11	0.02	0.00	0.00
Al2O3	20.85	22.20	22.00	22.18
FeO	16.68	21.77	24.92	24.30
MnO	0.66	1.53	0.61	0.91
MgO	2.97	8.51	7.02	8.17
CaO	19.96	7.18	6.78	6.36
Na2O (n.m.)	0.00	0.00	0.00	0.00
K2O (n.m.)	0.00	0.00	0.00	0.00
Cr2O3	0.01	0.01	0.02	0.01
Fe2O3	0.00	0.00	0.00	0.00
sum	**99.73**	**100.69**	**99.96**	**101.49**
cations				
Si	2.98	2.99	2.98	2.99
Ti	0.01	0.00	0.00	0.00
Al	1.90	1.98	2.00	1.98
Fe2+	0.96	1.36	1.59	1.51
Mn	0.04	0.10	0.04	0.06
Mg	0.34	0.96	0.81	0.92
Ca	1.65	0.58	0.56	0.52
Na	0.00	0.00	0.00	0.00
K	0.00	0.00	0.00	0.00
Cr	0.00	0.00	0.00	0.00
Fe3+	0.11	0.02	0.01	0.03
Sum	**8.01**	**8.00**	**8.01**	**8.00**
formula				
Mg	0.34	0.96	0.81	0.92
Mn	0.04	0.10	0.04	0.06
Ca	1.65	0.58	0.56	0.52
FeII	0.96	1.36	1.59	1.51
Summe X	**3.01**	**3.00**	**3.00**	**3.00**
exc. Fe	*0.01*	*0.00*	*0.00*	*0.00*
Si	2.98	2.99	2.98	2.99
Aliv	0.02	0.01	0.02	0.01
sum Z	**3.00**	**3.00**	**3.00**	**3.00**
Alvi	1.88	1.98	1.99	1.97
Cr	0.00	0.00	0.00	0.00
Ti	0.01	0.00	0.00	0.00
FeIII	0.11	0.02	0.01	0.03
sum Y	**2.00**	**2.00**	**2.00**	**2.00**
dmembers				
pyrope	11.41	32.05	26.92	30.67
almandine	32.10	45.24	53.09	50.20
grossular	49.28	18.29	17.87	15.66
spessartine	1.45	3.28	1.32	1.95
andradite	5.73	1.12	0.73	1.51

Table A7b: Representative EMP analyses of omphacite from samples of the Ganghe Unit

sample	9933	99119	99122	99206
mineral	omphacite	omphacite	omphacite	omphacite
comment	a11	9-6-10	1-3-5	6-1.1-5
	5	23	1	3
SiO2	54.61	55.45	56.02	55.91
TiO2	0.02	0.02	0.03	0.05
Al2O3	5.58	9.48	10.58	10.15
FeO	5.57	7.98	4.77	10.17
MnO	0.02	0.05	0.05	0.06
MgO	11.52	7.15	7.93	5.76
CaO	17.79	11.22	12.03	9.34
Na2O	4.16	7.94	7.51	8.82
K2O	0.05	0.00	0.00	0.00
Cr2O3	0.00	0.02	0.06	0.00
Fe2O3	0.00	0.00	0.00	0.00
sum	**99.31**	**99.28**	**98.97**	**100.25**
cations				
Si	1.99	2.01	2.01	2.01
Ti	0.00	0.00	0.00	0.00
Al	0.24	0.40	0.45	0.43
Cr	0.00	0.00	0.00	0.00
Fe3+	0.05	0.07	0.04	0.09
Mg	0.63	0.39	0.42	0.31
Ca	0.69	0.43	0.46	0.36
Mn	0.00	0.00	0.00	0.00
Fe2+	0.12	0.17	0.10	0.21
Na	0.29	0.56	0.52	0.61
K	0.00	0.00	0.00	0.00
sum	**4.01**	**4.03**	**4.01**	**4.03**
formula				
Si	1.99	2.01	2.01	2.01
Al	0.01	0.00	0.00	0.00
Fe3+	0.00	0.00	0.00	0.00
sum	**2.00**	**2.01**	**2.01**	**2.01**
M1				
Al	0.23	0.40	0.45	0.43
Fe3+	0.05	0.07	0.04	0.09
Cr	0.00	0.00	0.00	0.00
Ti	0.00	0.00	0.00	0.00
Mg	0.61	0.36	0.41	0.28
Fe2+	0.12	0.17	0.10	0.21
Mn	0.00	0.00	0.00	0.00
sum	**1.00**	**1.01**	**1.00**	**1.02**
M2				
Mg	0.02	0.02	0.01	0.03
Fe2+	0.00	0.00	0.00	0.00
Mn	0.00	0.00	0.00	0.00
Ca	0.69	0.43	0.46	0.36
Na	0.29	0.56	0.52	0.61
K	0.00	0.00	0.00	0.00
sum	**1.01**	**1.02**	**1.00**	**1.00**
dmembers				
WEF	70.10	43.85	46.95	36.94
jadeite	24.45	47.62	48.41	51.97
aegerine	5.46	8.53	4.65	11.09

Table A7c: Representative EMP analyses of phengite from samples of the Ganghe Unit

sample	99119	99122	99206
mineral	phengite	phengite	S6
comment	S6	S3	6-1.1-1
	9-7-1	1-2-3	prof r-r
	4	1	2
SiO2	53.34	55.37	53.08
TiO2	0.24	0.26	0.26
Al2O3	25.02	23.42	24.84
Cr2O3	0.01	0.07	0.00
FeO	2.61	1.81	3.34
MnO	0.00	0.00	0.00
MgO	4.24	5.17	4.25
CaO	0.00	0.00	0.00
BaO	0.71	0.11	0.56
Na2O	0.49	0.33	0.33
K2O	10.11	10.28	10.34
Fe2O3	0.00	0.00	0.00
sum	**96.79**	**96.80**	**97.00**
cations			
Si	3.50	3.60	3.49
Ti	0.01	0.01	0.01
Al	1.94	1.79	1.92
Cr	0.00	0.00	0.00
Fe 2+	0.07	0.05	0.09
Mn	0.00	0.00	0.00
Mg	0.42	0.50	0.42
Ca	0.00	0.00	0.00
Ba	0.02	0.00	0.01
Na	0.06	0.04	0.04
K	0.85	0.85	0.87
Fe 3+	0.07	0.05	0.09
Sum	**6.94**	**6.91**	**6.95**
formula			
Si	3.50	3.60	3.49
Al	0.50	0.40	0.51
sum	**4.00**	**4.00**	**4.00**
Al	1.44	1.40	1.41
Cr	0.00	0.00	0.00
Ti	0.01	0.01	0.01
Mg	0.42	0.50	0.42
Fe2+	0.07	0.05	0.09
Fe3+	0.07	0.05	0.09
Mn	0.00	0.00	0.00
sum	**2.01**	**2.01**	**2.02**
Ca	0.00	0.00	0.00
Ba	0.02	0.00	0.01
Na	0.06	0.04	0.04
K	0.85	0.85	0.87
sum	**0.93**	**0.90**	**0.92**
dmembers hliestedt 1980)			
muscovite	42.92	35.25	46.57
celadonite	50.18	60.15	48.77
paragonite	6.90	4.60	4.66
margarite	0.00	0.00	0.00